



This is to certify that the

dissertation entitled

# DESIGN AND DEVELOPMENT OF LOW-FLOW COEFFICIENT CENTRIFUGAL COMPRESSORS FOR INDUSTRIAL APPLICATION

presented by

Jean-Luc Di Liberti

has been accepted towards fulfillment of the requirements for

Ph.D. degree in Mechanical Engineering

Date May 13, 1998

MSU is an Affirmative Action/Equal Opportunity Institution

0-12771



PLACE IN RETURN BOX to remove this checkout from your record.

TO AVOID FINES return on or before date due.

MAY BE RECALLED with earlier due date if requested.

DATE DUE	DATE DUE	DATE DUE
MAY 2 5 2002		

1/98 c/CIRC/DateDue.p85-p.14

# DESIGN AND DEVELOPMENT OF LOW-FLOW COEFFICIENT CENTRIFUGAL COMPRESSORS FOR INDUSTRIAL APPLICATION

By

Jean-Luc Di Liberti

#### A DISSERTATION

Submitted to
Michigan State University
in partial fulfillment of the requirements
for the degree of

**DOCTOR OF PHILOSOPHY** 

Department of Mechanical Engineering

1998

#### **ABSTRACT**

# DESIGN AND DEVELOPMENT OF LOW-FLOW COEFFICIENT CENTRIFUGAL COMPRESSORS FOR INDUSTRIAL APPLICATION

#### Ву

#### Jean-Luc Di Liberti

In centrifugal compressors, as in any type of turbomachinery, there exists an optimum efficiency over a certain range of flow. The flow coefficient of a centrifugal stage can be correlated to the efficiency, and the optimum range is between 0.06 and 0.09. In a multistage machine, the volume-flow rate decreases as the pressure of the flow is increased through the stages. As the last stages are reached, the flow coefficient  $\Phi$  is, therefore, smaller than at the inlet of the machine. The impeller and diffuser channel are narrower to handle the smaller volume flow rate, leading to higher friction losses. Hence, low-flow coefficient compressors are inherently inclined to have lower efficiency than the previous stage.

A one-dimensional and a quasi-three-dimensional code were successfully developed to design a centrifugal impeller. Ten low-flow coefficient compressors were designed and analyzed numerically to analyze the effect of the design flow coefficient, of the outlet width-outlet blade angle combination, and of the blade leading edge position on the stage performance.

The numerical analysis provided vital information regarding the internal aerodynamic of each impeller. All the impellers exhibited a jet/wake flow pattern. The

high backsweep angle of the blade was responsible for the rather small wake area at the design point.

The change in blade angle-blade outlet width showed that the wake was the largest for the impeller with the largest backswept. Hence, the development of the wake appeared more controlled by the curvature in the meridional plane and the diffusion achieved, than by the exit blade angle. Even if the wake was larger in the high-backswept impeller, higher performances were obtained because of the larger impeller exit area; the lower velocity levels and the wider diffuser led to reduce the total pressure loss. No advantage was found by using an impeller with a blade whose leading edge is located in the radial part of the impeller.

The performances of each impeller were estimated by CFD on a stage basis for hydraulically smooth and for rough walls. The necessary aero-thermodynamic quantities required to calculate the performance were mass-averaged at both the impeller exit and the diffuser exit. The numerical results were used to update the one-dimensional model and generate the predicted performance map of each impeller. It was found that the one-dimensional prediction with no external losses was in very good agreement with the CFD analysis with rough walls. As expected, the performances of the stages were found to decrease as the flow coefficient was reduced. The impellers with 60 and 65 degrees backsweep were found to be a good compromise between efficiency level, pressure ratio, and stability.

To Lisa

#### **ACKNOWLEDGMENTS**

The author is very grateful to his advisor, Professor Abraham Engeda, for his guidance, support, and encouragement throughout the course of his research work. Sincere thanks go to Professors Craig Somerton, Chang Wang and Indrek Wichman for their advice, suggestions and interest in this work. A particular thanks goes to Mr. Mike Flathers and Mr. Mike Cave from Solar Turbines Inc. for initiating this work, and for their help and support.

The author is also grateful to Professor Rene Van den Braembussche without whom he would not have been studying centrifugal compressors.

A special thanks goes to Mr. Frank Shih, Mr. Tim David, and Mr. Ed Fowler at Solar Turbines Inc.; Mr. Georges Bache and Mr. John Crapuchettes at AEA Technology for their helpful discussions; and to Mr. Craig Gunn at MSU for his help in preparing this thesis. The author also appreciates the numerous criticism, assistance, and great friendship of Naresh Amineni but also of Won Kim and all the German students that came to study at the turbomachinery lab at Michigan State University: Joachim Fischer, Bernd Wilmsen, and Alexander Kuppe.

The support of Solar Turbines Inc. and of the Division of Engineering Research is greatly appreciated.

Last, but certainly not least, my family and Lisa Nicholas, for their love and support.

## TABLE OF CONTENTS

ACKNOWLEDGMENTS	V
LIST OF TABLES	IX
LIST OF FIGURES	X
NOMENCLATURE	XIII
GreekSubscripts	
1. INTRODUCTION	1
DEMANDS ON AND CHALLENGES FOR CENTRIFUGAL COMPRESSORS      THE NEED FOR LOW-FLOW COEFFICIENT COMPRESSORS      STRUCTURE AND OBJECTIVES OF THE WORK	3
2. GENERAL DISCUSSION OF TURBOMACHINES	7
2.1. ELEMENTS OF A CENTRIFUGAL COMPRESSOR STAGE  2.2. VELOCITY TRIANGLES  2.3. THE EULER EQUATION  2.4. HEAD RISE  2.5. EFFICIENCY  2.6. WORK REDUCTION FACTOR AND SLIP FACTOR  2.7. OPERATING MAP AND COMPRESSOR RANGE  2.8. DIMENSIONLESS PARAMETERS  2.8.1. Flow and head coefficient  2.8.2. Specific diameter and specific speed	9 10 14 16 20 20
3. FLOW IN THE IMPELLER AND DESIGN PARAMETERS	
3.1.1. Qualitative Description of the Flow in the Impeller 3.1.2. Inviscid Flow Analysis 3.1.3. Secondary Flows 3.1.4. Effect of Rotation and Streamline Curvature on Boundary Layer Stabilit 3.1.5. Experimental Observation 3.2. Losses in a Centrifugal Compressor 3.2.1. Internal Losses 3.2.2. External Losses 3.3. One-Dimensional Design Parameters 3.3.1. Overall View of the 1-D Design Parameter 3.3.2. Inducer Hub and Tip Radius 3.3.3. Exit Width 3.3.4. Velocity Ratio	25 29 ty . 31 40 40 46 46 47 49
3.3.5. Slip Factor	

4.1. DES	CRIPTION OF THE 1-D METHOD	52
4.1.1.	Two-zone Model	<i>53</i>
4.1.2.	Impeller Diffusion Level	54
<i>4.1.3</i> .	Off-Design Performance	56
4.2. ONE	E-DIMENSIONAL ANALYSIS	58
<i>4.2.1.</i>	Design Constraints	58
	Modeling Assumptions	
	Influence of the Modeling Assumptions on the Choice of the Geometry	
	1-D Impeller Design	
	EAMLINE CURVATURE THROUGHFLOW METHOD	
4.3.1.	Description of the Quasi-3D Method	<i>73</i>
	Definition of the Blade Geometry	
	Impeller Blade Shape for the Five Impellers	
	Velocity Distribution and Blade Loading for the Five Impellers	
	AND ANALYSIS OF FOUR LOW-FLOW COEFFICIENT	
	SSORS	78
	IGN REQUIREMENTS	
	Inlet Design Conditions	
	Impeller Sizing	
	EAMLINE CURVATURE THROUGHFLOW ANALYSIS	
	Geometry	
	Streamline Curvature Analysis	
	O Analysis	
	Presentation of the Commercial Software TASCflow	
	Equations Solved	
	Boundary Conditions	
	Grid Specifications	
	Convergence Criteria	
	ALITATIVE ANALYSIS OF THE FLOW FIELD	
	Flow at Design Point in the AA Impeller	
	Flow at Off-design Conditions (AA Impeller)	
5.4.3.		
	•	
	ARISON OF THE VARIOUS DESIGNS	
	T-Processing Technique	
	ANTITATIVE ANALYSIS OF THE AA, AB, AC, AND AD IMPELLERS	
	Performance at Design Point	
	Consequence for the 1-D analysis	
	Determination of the TEIS Models	
	Off-design Performance (AA impeller)	
6.2.5.	Off design performance of the AA, AB, AC and AD stages	118
	LIDATION OF THE LOADING ESTIMATION	
6.4. AN	ALYSIS OF THE EFFECT OF EXIT BLADE ANGLE AND WIDTH	121
<i>6.4.1</i> .	Qualitative analysis	121
	Quantitative analysis	
6.5. INF	LUENCE OF THE BLADE LEADING EDGE	131

7. CONCLUSIONS AND RECOMMENDATIONS	133
BIBLIOGRAPHY	136
APPENDIX A	141
APPENDIX B	143
APPENDIX C	152
APPENDIX D	166

## LIST OF TABLES

Table 3.1 Summary of the limitation on some main 1D parameters	47
TABLE 4.1 GEOMETRY OF THE FIVE SELECTED IMPELLERS	72
Table 5.1 Impeller main dimensions	81
Table 5.2 Design velocity triangles	81
TABLE 6.1 AA, AB, AC, AD STAGE PERFORMANCE PREDICTION	110
Table 6.2 Impellers exit conditions	112
TABLE 6.3 TEIS MODELS FOR THE AA, AB, AC, AND AD IMPELLERS	116
Table 6.4 Impeller exit conditions	127
Table 6.5 TEIS models	129
TABLE 6.6 TASCFLOW ANALYSIS (SMOOTH WALLS) – EFFECT OF THE LEADING EDGE	
POSITION	131

## **LIST OF FIGURES**

FIGURE 2.1 CENTRIFUGAL COMPRESSOR STAGE	8
FIGURE 2.2 SHROUDED IMPELLER	8
FIGURE 2.3 INLET AND EXIT VELOCITY TRIANGLES	. 10
FIGURE 2.4 EFFECT OF EXIT BLADE ANGLE ON THE ENTHALPY RISE	. 12
FIGURE 2.5 REPRESENTATION OF A COMPRESSION PROCESS IN A T-S DIAGRAM	. 15
FIGURE 2.6 IMPELLER EXIT VELOCITY TRIANGLE WITH AND WITHOUT SLIP	. 17
FIGURE 2.7 INFLUENCE OF THE BLADE NUMBER AND THE EXIT BLADE ANGLE ON THE SLIP	•
FACTOR	. 18
FIGURE 2.8 TYPICAL CENTRIFUGAL COMPRESSOR HEAD-FLOW CURVE	. 19
FIGURE 2.9 MAXIMUM COMPRESSOR AND PUMP EFFICIENCIES AS FUNCTION OF SPECIFIC	
SPEED (BALJE 1981)	.23
FIGURE 2.10 TEST IMPELLER EFFICIENCIES VERSUS AVERAGE SPECIFIC SPEED (ROGERS	
1980)	. 23
FIGURE 3.1 SCHEMATIC OF COMPRESSOR STAGE FLOW REGION	. 25
FIGURE 3.2 FORCES ACTING ON A FLUID ELEMENT INSIDE AN IMPELLER PASSAGE	. 26
FIGURE 3.3 VELOCITY DISTRIBUTION IN IMPELLER PASSAGE – INVISCID ANALYSIS	. 27
FIGURE 3.4 FLOW IN THE MERIDIONAL PLANE NEAR IMPELLER EXIT – INVISCID ANALYSIS	;
(AFTER KRAIN 1984)	. 28
FIGURE 3.5 MOVEMENT OF LOW P* FLUID IN THE BOUNDARY LAYER IN AN IMPELLER	
PASSAGE (AFTER JOHNSON 1978)	.31
FIGURE 3.6 SIMPLIFIED REPRESENTATION OF THE FLOW BETWEEN TWO RADIAL BLADES	.32
FIGURE 3.7 DEFINITION OF STABLE AND UNSTABLE CASES (AFTER JOHNSTON AND EIDE	
1976)	.33
FIGURE 3.8 OPTICAL MEASUREMENT PLANES (ECKARDT 1976)	. 34
FIGURE 3.9 NON-DIMENSIONAL VELOCITY DISTRIBUTION AT FIVE STATIONS ALONG THE	
IMPELLER (ECKARDT 1976)	.36
FIGURE 3.10 NORMALIZED MERIDIONAL VELOCITY IN BACKSWEPT IMPELLER (ECKARDT	
1980)	. 37
FIGURE 3.11 ROTARY STAGNATION PRESSURE AT IMPELLER EXIT, BELOW DESIGN POINT	
(JOHNSON AND MOORE 1983)	. 38
FIGURE 3.12 ROTARY STAGNATION PRESSURE AT IMPELLER EXIT, AT DESIGN POINT	
(JOHNSON AND MOORE 1983)	.38
FIGURE 3.13 ROTARY STAGNATION PRESSURE AT IMPELLER EXIT, ABOVE THE DESIGN PO	INT
(JOHNSON AND MOORE 1983)	
FIGURE 3.14 EFFECT OF INLET MACH NUMBER ON LOSS COEFFICIENT (DOUBLE CIRCULAI	R
ARC BLADE CASCADE) LIEBLEIN 1965	
FIGURE 3.15 IMPELLER MAIN GEOMETRICAL PARAMETERS	
FIGURE 3.16 IMPELLER MAIN DIMENSION (AFTER PAROUBEK ET AL. 1994)	.48

FIGURE 3.17 IMPELLERS EFFICIENCY (PAROUBEK ET AL. 1994)	49
FIGURE 3.18 SLIP FACTORS (PAROUBEK ET AL. 1994)	
FIGURE 4.1 COMPARISON OF ACHIEVABLE PRIMARY FLOW DIFFUSION IN INDUSTRIAL 2D	)
IMPELLERS AND IN STRAIGHT INLET, 3D IMPELLERS (BENVENUTTI 1978)	55
FIGURE 4.2 TEIS MODEL – DIFFUSING PASSAGES (AFTER JAPIKSE 1984)	56
Figure 4.3 Effect of $\chi$ and MR2 on the wake width	60
Figure 4.4 Effect of $\chi$ and MR2 on $v=W_{2s}/W_{2p}$	
FIGURE 4.5 EFFECT OF $\chi$ AND MR2 ON C= $W_{2m}/W_{2p}$ AND ON $\delta_{2p}$	
Figure 4.6 Effect of $\chi$ and MR2 on the impeller efficiency	
Figure 4.7 Effect of $\chi$ and MR2 on the impeller pressure ratio	
FIGURE 4.8 INFLUENCE OF THE HUB-TO-SHROUD INLET RADIUS RATIO ON THE SHROUD	
INLET RELATIVE MACH NUMBER	66
FIGURE 4.9 STAGE TOTAL-TO-TOTAL PRESSURE RATIO AS A FUNCTION OF IMPELLER EXT	
WIDTH AND IMPELLER EXIT BLADE ANGLE	67
FIGURE 4.10 IMPELLER EXIT TANGENTIAL VELOCITY VERSUS IMPELLER WIDTH	
FIGURE 4.11 RELATIVE VELOCITY RATIO AS A FUNCTION OF IMPELLER EXIT WIDTH AND	
IMPELLER EXIT BLADE ANGLE	68
FIGURE 4.12 IMPELLER EXIT ABSOLUTE FLOW ANGLE VS. IMPELLER EXIT WIDTH AND	
IMPELLER EXIT BLADE ANGLE	69
FIGURE 4.13 DIFFUSER PRESSURE RECOVERY AS A FUNCTION OF IMPELLER EXIT WIDTH A	AND
EXIT BLADE ANGLE	70
FIGURE 4.14 DIFFUSER TOTAL PRESSURE LOSS COEFFICIENT AS A FUNCTION OF IMPELLE	R
EXIT WIDTH AND EXIT BLADE ANGLE	71
FIGURE 4.15 DEFINITION OF THE LEAN ANGLE	
FIGURE 4.16 VIEW OF THE IMPELLER TIP AND DEFINITION OF THE RAKE ANGLE	
FIGURE 4.17 IMPELLERS MERIDIONAL CONTOUR	
FIGURE 4.18 BLADE ANGLE DISTRIBUTION FOR THE AA50, AA55, AA65, AND AA70	
FIGURE 4.19 BLADE-TO-BLADE LOADING FOR THE IMPELLERS	
FIGURE 5.1 MERIDIONAL CONTOURS OF IMPELLERS	
FIGURE 5.2 BLADE ANGLE DISTRIBUTIONS	
FIGURE 5.3 RELATIVE VELOCITY DISTRIBUTION AT HUB (LEFT) AND SHROUD (RIGHT) FO	
THE AA IMPELLER AT DESIGN POINT	
FIGURE 5.4. BLADE-TO-BLADE LOADING	
FIGURE 5.5 MERIDIONAL VIEW OF CALCULATION GRID (IMPELLER ONLY)	
FIGURE 5.6 BLADE-TO-BLADE VIEW OF THE CALCULATION GRID (IMPELLER ONLY)	
FIGURE 5.7 VELOCITY VECTOR AT MID PITCH (AA IMPELLER, DESIGN POINT)	
FIGURE 5.8 VELOCITY VECTOR NEAR THE SUCTION SIDE (AA IMPELLER, DESIGN POINT)	
FIGURE 5.9 CALCULATING STATIONS ALONG THE IMPELLER CHANNEL	
FIGURE 5.10 NORMALIZED MERIDIONAL VELOCITY AT STATION I (AA IMPELLER, DESIG	
POINT)	
FIGURE 5.11 NORMALIZED MERIDIONAL VELOCITY AT STATION II (AA IMPELLER, DESIG	
POINT)	
FIGURE 5.12 NORMALIZED MERIDIONAL VELOCITY AT STATION III (AA IMPELLER, DESI	
POINT)	
FIGURE 5.13 NORMALIZED MERIDIONAL VELOCITY AT STATION IV (AA IMPELLER, DESI	
POINT)	ヺ1

FIGURE 5.14 NORMALIZED MERIDIONAL VELOCITY AT STATION V (AA IMPELLER, DESIGNOT)	GN 98
FIGURE 5.15 FLOW ANGLE DISTRIBUTION AT STATION V (AA IMPELLER, DESIGN POINT)	98
FIGURE 5.16 REDUCED RELATIVE TOTAL PRESSURE (NORMALIZED BY PO AT INLET) (AA IMPELLER, DESIGN POINT)	A
FIGURE 5.17 TKE DISTRIBUTION AT STATION V (AA IMPELLER, DESIGN POINT)	
FIGURE 5.18 NORMALIZED MERIDIONAL VELOCITY AT STATION V (AA IMPELLER, 70%	. 101
FLOW)FIGURE 5.19 VELOCITY VECTORS AT MID-PITCH (AA IMPELLER, 60% MASS-FLOW)	
FIGURE 5.20 REDUCED RELATIVE TOTAL PRESSURE (AA IMPELLER, 60% MASS-FLOW)	
FIGURE 5.21 NORMALIZED VELOCITY DISTRIBUTION (STATION V, A IMPELLER, 60% MA	ASS
FLOW)	. 104
FIGURE 5.22 REDUCED RELATIVE TOTAL PRESSURE DISTRIBUTION (AA, 140% MASS FLO	
FIGURE 5.23 NORMALIZED VELOCITY DISTRIBUTION AT STATION V (AA, 140%	
MASSFLOW)	. 105
FIGURE 5.24 TKE AT STATION V (AB IMPELLER, DESIGN POINT)	
FIGURE 5.25 TKE AT STATION V (AC IMPELLER, DESIGN POINT)	
FIGURE 5.26 TKE AT STATION V (AD IMPELLER, DESIGN POINT)	
FIGURE 6.1 PERFORMANCE PREDICTION FOR THE AA, AB, AC, AND AD STAGES	
FIGURE 6.2 DIFFUSER LOSS COEFFICIENT AND PRESSURE RECOVERY	. 115
FIGURE 6.3 CALCULATED PERFORMANCE MAP FOR THE AA IMPELLER	. 117
FIGURE 6.4 PERFORMANCE MAP PREDICTION OF THE AA, AB, AC AND AD STAGES	. 119
FIGURE 6.5 ISENTROPIC BLADE-TO-BLADE LOADING (AB IMPELLER, DESIGN POINT)	. 121
FIGURE 6.6 NORMALIZED MERIDIONAL VELOCITY (AA50, DESIGN POINT)	. 123
FIGURE 6.7 NORMALIZED MERIDIONAL VELOCITY (AA55, DESIGN POINT)	. 123
FIGURE 6.8 NORMALIZED MERIDIONAL VELOCITY (AA65, DESIGN POINT)	. 124
FIGURE 6.9 NORMALIZED MERIDIONAL VELOCITY (AA70, DESIGN POINT)	. 124
FIGURE 6.10 TKE CONTOUR AT STATION V (AA50, DESIGN POINT)	. 125
FIGURE 6.11 TKE CONTOUR AT STATION V (AA70, DESIGN POINT)	. 125
FIGURE 6.12 RELATIVE FLOW ANGLE AT STATION V (AA55, DESIGN POINT)	. 126
FIGURE 6.13 RELATIVE FLOW ANGLE AT STATION V (AA65, DESIGN POINT)	. 126
FIGURE 6.14 PERFORMANCE AT DESIGN POINT	. 128
FIGURE 6.15 DIFFUSER PERFORMANCE AT DESIGN POINT	. 129
FIGURE 6.16 PERFORMANCE PREDICTION COMPARISON	. 130
FIGURE C.1 COORDINATE SYSTEM FOR THE GENERAL EQUATIONS	. 153
FIGURE C.2 DEFINITION OF THE GEOMETRY AND NOTATIONS	. 154
FIGURE C.3 EXAMPLE OF BEZIER CURVE	. 159
FIGURE C.4 EXAMPLE OF CALCULATION GRID	. 160
FIGURE C.5 LOCAL COORDINATE SYSTEM	
FIGURE C.6 TYPICAL BLADE ANGLE VARIATION	. 163
FIGURE D.1 MERIDIONAL VELOCITY PROFILE AT IMPELLER INLET	. 166

#### **NOMENCLATURE**

b width or distance along a quasi-orthogonal C absolute velocity Cd dissipation coefficient Cf friction coefficient  $C_p$ specific heat at constant pressure pressure recovery Cp D diameter hydraulic diameter Dh DR diffusion ratio Fb distributed blade force Fd dissipative blade force g gravitational constant Н head h enthalpy I rothalpy or node number in the streamwise direction incidence (blade angle minus flow angle) i node number in the pitchwise direction J K node number in the spanwise direction M Mach number MR2 Mach number ratio Relative mach number Mw distance along the meridional direction m m mass-flow rate N rotational speed specific speed (US definition) NS P pressure Q volume flow rate Ò heat exchanged R radius or gas constant r radius radius of curvature rk entropy S T temperature U peripheral speed W relative velocity Ŵ work exchanged Z blade number

#### Greek

Α

area

α blade or flow angle (relative to meridional) or slope angle of calculating station

- β blade or flow angle (relative to meridional)
- γ isentropic exponent or lean angle
- δ deviation or thickness
- ε area ratio between secondary zone and outlet area or slope angle of meridional direction
- η effectiveness or efficiency
- θ circumferential coordinate
- μ work reduction factor
- ρ density
- $\sigma$  slip factor
- τ torque or exit rake angle
- Φ flow coefficient
- χ ratio of the mass in the secondary zone to mass flow
- Ψ head coefficient
- ω rotational speed
- $\Omega_{\rm s}$  streamwise vorticity

#### **Subscripts**

- bl blade
- F front stage
- i ideal or inlet
- is isentropic
- LE leading edge
- M middle stage
- m meridional
- o outlet
- p on previous calculating station
- ps pressure side
- R rear stage
- r on current calculating station or radial
- ss suction side
- t tip
- th throat
- u tangential
- z axial direction
- 0 stage entrance or total conditions
- 2 impeller exit
- 4 diffuser pinch
- 5 diffuser exit
- 6 exit bend
- 7 exit return vane
- 8 exit stage

#### 1. INTRODUCTION

#### 1.1. Demands on and Challenges for Centrifugal Compressors

A centrifugal compressor is a high speed rotating device that adds energy to a fluid passing through it. The flow enters the impeller axially through the impeller "eye" and leaves the impeller radially at higher pressure and absolute velocity. The range of applications for centrifugal compressors is large. They can be found in various industries: from the process industry to petrochemical industry, from gas turbines to turbochargers for internal combustion engine, and from aeronautical applications to air conditioning units.

For the early gas turbine application, a single-stage centrifugal compressor was sufficient. After World War II, as the need for larger power grew, axial flow compressors appeared more suitable for large engines. At the time, multistaging of centrifugal compressors, especially for aircraft application, seemed inappropriate because of the necessity to turn the flow from the radial back to the axial direction to enter the next stage. The additional ducting required contributed to the increase in size and weight of the machine, which does not occur in axial machines. Consequently, most development funding went towards the axial machine, leaving the centrifugal compressor on the side.

By the late fifties, it became clear that smaller gas turbines would have to use centrifugal compressors. Centrifugal compressors appeared to be more suitable for small volume flows. On a single stage application (and for the same duty), they have a shorter axial length than their axial counter part and a better resistance to foreign objects. They are also able to operate over a wider flow range for a constant rotational speed.

For turbochargers, the centrifugal compressor is the ideal candidate with its wide margin between surge and choke, which allows it to match the continuous range of automotive engines, from idle to full power.

In the process industry, because size and weight are of secondary importance, the centrifugal compressor can be used in multistage applications. The return systems between each impeller have seen their aerodynamics improved, and higher efficiency can now be achieved.

The design of the impeller depends mainly on the type of application. For centrifugal compressors used in gas turbines or turbocharger applications, the impeller is unshrouded: the tip of the moving blade passes near the casing where a small clearance is maintained. Generally, the impeller is predominantly axial at the inlet. This axial portion is called the inducer. The aerodynamic performance will be improved by using a well-designed inducer.

For industrial applications, multistage centrifugal compressors are used. To limit the overall length of the machine, the impellers have a smaller axial inlet. They are generally shrouded, that is, a cover is fixed on the blades and rotates with them. This removes the need for clearance, but the additional weight generates stresses that limit the maximum rotational speed that can be used.

In this thesis, centrifugal impellers for an industrial multistage machine will be at the center of attention.

#### 1.2. The Need for Low-Flow Coefficient Compressors

In centrifugal compressors, as in any type of turbomachinery, there exist an optimum efficiency over a certain range of flow. The flow coefficient  $\Phi$  of a centrifugal stage can be correlated to the efficiency, and is defined by

$$\Phi = \frac{Q}{\frac{\pi}{4} D_{tip}^2 U_{tip}} \tag{1.1}$$

where Q is the inlet volume flow rate,  $D_{tip}$  is the impeller tip diameter, and  $U_{tip}$  is the peripheral speed at impeller tip. The optimum range is for a flow coefficient between 0.06 and 0.09. In a multistage machine, the volume-flow rate decreases as the pressure of the flow is increased through the stages. As the last stages are reached, the flow coefficient  $\Phi$  is, therefore, smaller than at the inlet of the machine. The impeller and diffuser channel are narrower to handle the smaller volume flow rate. The friction losses are thereby increased, and a smaller efficiency is to be expected. Also, the disk friction losses and the leakage losses (see Chapter 4) have been shown to be inversely proportional to the volume flow rate. Hence, low-flow coefficient compressors are inherently inclined to have lower efficiency than the earlier stage.

If efficiency is directly related to flow coefficient, one would think that the only way to improve the performance of such compressors is to increase their flow coefficient. Looking back at equation (1.1), this would imply decreasing  $D_{tip}$  or reducing  $U_{tip}$ . In both cases, this would lead to a decrease in the work input of the machine (see Section 2.3), which is not desirable.

The literature covering the subject of low-flow coefficient compressor is limited.

Four main sources have been found. The first one is the solution proposed by Rusak

(1974) in his patent. He proposed to reduce the friction losses by enlarging the impeller exit area while continuously increasing the thickness of the blade from inlet to exit in order to maintain the same diffusion. This leads to a larger hydraulic diameter. The invention was claimed for very low-flow coefficient impellers only. Very little performance data were provided. Efficiencies around 55% at a flow coefficient of 0.008 were quoted.

The second reference is by Paroubek et al. (1994). They investigated the effect of the hub-to-outlet diameter ratio and the exit width to exit diameter ratio. They found that higher performances were obtained with the smallest hub diameter and with the wider impellers. Unfortunately, the hub diameter in a multi-stage machine has already been optimized, and is more or less set by rotordynamics considerations. The limited geometrical input and the non-dimensionalized experimental results reduced greatly the interest in this paper.

The third reference is by Koizumi (1983). He mainly showed the large impact of the Reynolds number on the performance of the impeller and the need to maintain the surface roughness of all the passages as low as possible.

The last reference is by Casey (1990). He showed experimentally that impellers with higher backward-swept blades and a larger impeller exit width could lead to better performance even with their smaller work input. The optimum configuration was difficult to evaluate with the conventional prediction methods and required an experimental evaluation to determine the best design. The large flow angle (from radial) at the diffuser entrance led to instabilities in the vaneless diffuser at low flow rates, and the use of a vaned diffuser was recommended by the author.

#### 1.3. Structure and Objectives of the Work

In this thesis, centrifugal compressor stages with flow coefficient below 0.022 will be considered. No attempt has been made to minimize the seal losses or the disc friction losses. Only a better seal design could reduce the seal friction losses, which is beyond the scope of this thesis. For the disc friction losses, the only recommendation will be to manufacture the impeller with the best surface finish on the back disk.

The purpose of the work will be to optimize the geometry of the impeller in order to keep the friction losses as low as possible. For this, different combinations of blade outlet angles and exit impeller widths have been studied to fulfill the design requirement of an industrial application.

The return channels between each stage have been designed and analyzed, but the results will not be presented here.

This dissertation starts with a general chapter on centrifugal compressors to define the notations and the specific vocabulary used through this thesis.

Chapter 3 presents the general flow characteristics in a centrifugal impeller. An inviscid analysis explains the forces applied to a fluid element travelling through a blade passage. The results of secondary flow theory are described, and experimental results are shown to help visualize the flow field. The different types of losses and the one-dimensional parameters are then reviewed.

The first step in the work was to develop two codes to design a centrifugal compressor: a one-dimensional code and a streamline curvature through-flow code.

These codes are presented in Chapter 4. They have been applied to design five impellers

satisfying the same design requirements but having a different outlet blade angle and outlet width. The detailed CFD analysis of these impellers is presented in Chapter 6.

Chapter 5 presents the design of four low-flow coefficient compressors as an extension of an existing family of impeller. The one-dimensional code and streamline curvature code have been used to select the geometry. A commercial CFD code, TASCflow, has then been used to qualitatively describe the flow field inside the impellers. The effect of the mass flow rate on the flow field of the first impeller is shown. The flow field between the four impellers is then compared.

Chapter 6 attempts to obtain quantitative results from the CFD in order to compare all the designs developed in Chapter 4 and 5. The analysis of two more impellers (one with a long inducer and one with no inducer) is presented.

The objective of this work is to use CFD as a way of artificially testing various designs, as CFD can provide information on many details unreachable through experiments. The quantitative results should provide the necessary information to select the best suitable design.

#### 2. GENERAL DISCUSSION OF TURBOMACHINES

The purpose of this chapter is to define some general parameters and basic concepts that are commonly used in the area of turbomachinery and to introduce the notation that will be used throughout this thesis.

#### 2.1. Elements of a Centrifugal Compressor Stage

A centrifugal compressor stage consists of an impeller (the rotating part) and a diffuser (non-rotating). Inlet guide vanes are sometimes used in front of the rotor to direct the flow to the impeller eye (or inducer, i.e. the axial part of the impeller). The impeller is used to impart energy to the flow by increasing the velocity and pressure of the fluid. The diffuser is used to convert the kinetic energy available at the impeller exit into static pressure by decelerating the fluid. The diffuser is followed by a collector, a scroll (volute), or a return channel depending on the type of application.

For a multistage machine, as the flow leaves the impeller radially, a return channel is used at the diffuser exit to turn the flow back in the axial direction. Return vanes are used to remove any residual swirl before entering the next stage. In the last stage, the diffuser discharges into a volute that leads the fluid to the exit piping system. Figure 2.1 shows a typical centrifugal compressor stage.

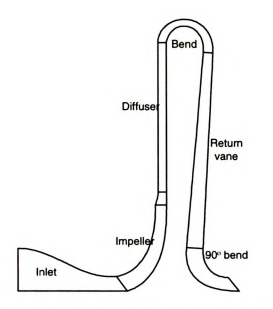


Figure 2.1 Centrifugal compressor stage

The impeller is the essential element of the centrifugal compressor stage. There are two types of impellers: unshrouded, which does not have a front cover, and shrouded, which has a cover. Figure 2.2 shows a meridional view of a shrouded impeller.

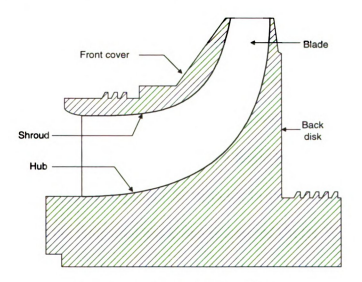


Figure 2.2 Shrouded impeller

By using a shrouded wheel, the secondary flow arising from tip clearance can be avoided. A trade-off must be made between the tip clearance losses of the unshrouded wheel, and the cover friction losses of the shrouded wheel. The high stress generated by the front cover limits the use of this type of impeller to relatively low rotational speed machines.

#### 2.2. Velocity Triangles

Velocity triangles are used to represent the velocity components (absolute or relative) at any station of a turbomachine. The velocity measured in a fixed frame is called absolute velocity and is denoted by C. The velocity measured with respect to a rotating frame is denoted by W. The blade speed relates both velocities, and the following vector relation holds:

$$\vec{C} = \vec{W} + \vec{U}$$

where U is the blade speed, also called the peripheral speed.

Figure 2.3 shows a typical velocity triangle with the notation that will be used throughout the thesis. The velocity vectors shown are those for the mean flow at a specified radius at inlet and at exit. The flow direction within the rotor passage or on the blade is not shown in the diagram.  $\alpha$  represents the flow angle between the absolute velocity and the meridional plane, and  $\beta$  is the flow angle between the relative velocity and the meridional plane. The component of velocity in the tangential direction is the projection of C (or W) in the tangential plane and is denoted Cu (or Wu).

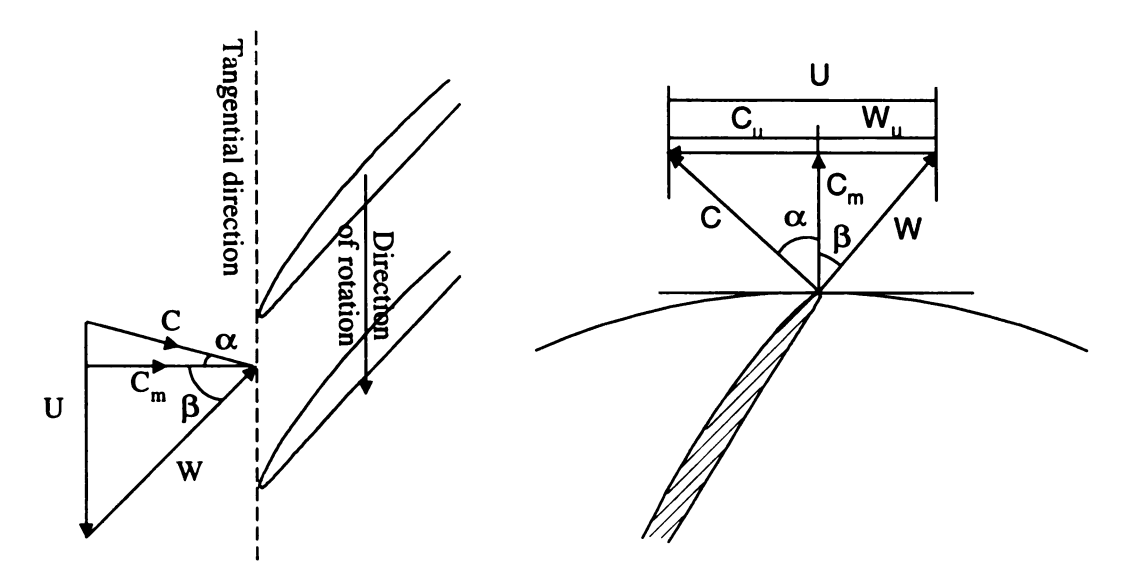


Figure 2.3 Inlet and exit velocity triangles

#### 2.3. The Euler Equation

The Euler equation relates the head change in a turbomachine to the velocities at the impeller inlet and exit. The Euler equation is derived from the conservation of linear momentum: the rate of change in linear momentum of a volume moving with the fluid is equal to the surface forces and body forces acting on the fluid.

By the conservation of momentum principle, the change of angular momentum (obtained by the change in tangential velocities) is equal to the summation of all forces acting on the rotor, i.e. the net torque of the rotor.

Mathematically, between inlet (1) and exit (2), this can be written as

$$\tau = \dot{m} \big( r_1 C_{u1} - r_2 C_{u2} \big)$$

where  $C_{u1}$  and  $C_{u2}$  are the tangential velocity at inlet and exit.

The rate of change of energy transfer is the product of the torque and the angular velocity, and therefore the total energy transferred is

$$E = \tau \omega = \dot{m} (r_1 \omega C_{u1} - r_2 \omega C_{u2}) = \dot{m} (U_1 C_{u1} - U_2 C_{u2})$$

where  $U_1$  and  $U_2$  are the peripheral velocity at  $r_1$  and  $r_2$ .

The energy transferred per unit of mass flow is equal to the change in total enthalpy  $h_0$  and hence

$$\Delta h_0 = U_2 C_{u2} - U_1 C_{u1} = h_{02} - h_{01} = \overline{C}_p (T_{02} - T_{01})$$

where  $\overline{c}_p$  is the average specific heat between inlet and outlet.

It is useful to relate the enthalpy change to the exit blade angle. Using the velocity triangle at the impeller exit and assuming no prewhirl, the enthalpy rise is given by

$$C_{u2} = U_2 + C_{m2} \tan \beta_2$$

with the convention that  $\beta_2$ <0 for a backward swept impeller (the word backswept is used to describe impellers with vanes inclined backward at the outlet).

Introducing the theoretical head rise  $\psi = \frac{\Delta H}{U_2^2}$  and the flow parameter  $\phi = \frac{C_{\pi_2}}{U_2}$  to make a non dimensional representation of the enthalpy rise versus mass flow rate, the following relation is obtained:

$$\psi = 1 + \varphi \tan \beta_2$$

which is plotted in Figure 2.4.

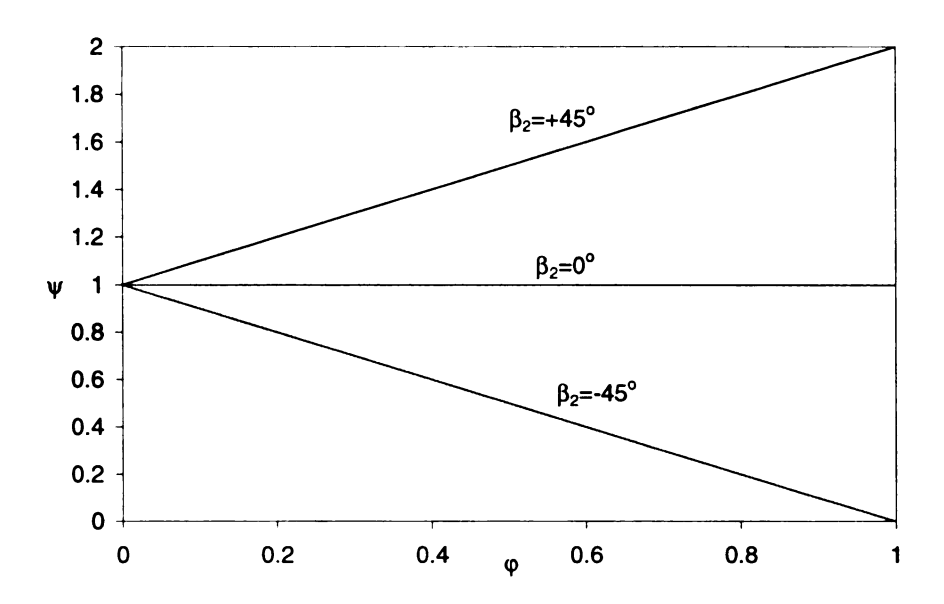


Figure 2.4 Effect of exit blade angle on the enthalpy rise

The theoretical head rise is seen to decrease with increasing mass flow rate for a backward-swept impeller, independent of the mass flow for a radially-ending impeller, and to increase with mass flow for a forward-leaned blade impeller. The increasing head with decreasing mass flow for backward-swept impellers gives a more stable operating stage characteristic and consequently a greater range.

It is worth noting that the enthalpy change in the machine can also be expressed in the following way:

$$\Delta h_0 = \frac{1}{2} \left\{ U_2^2 - U_1^2 \right\} + \left[ W_1^2 - W_2^2 \right] + \left[ C_2^2 - C_1^2 \right] \right\}$$
 (2.1)

after having introduced the relations inside the inlet and exit velocity triangles

$$W^2 = C^2 + U^2 - 2UC_u$$

Hence, it is seen that the enthalpy rise in a centrifugal machine is due to three different contributions. The first term in Equation (2.1) represents the change of energy of a particle as it moves from one radius to another. This contribution by the centrifugal

forces represents about one-half of the work input, and is accomplished without loss (Casey and Marty 1986). The second term represents the rise in enthalpy due to the diffusion of the relative flow. This term represents approximately one-fifth of the total work input (depending on the impeller shape). Assuming that the velocity at the exit stage is equal to the velocity at the inlet of the stage ( $C_1=C_4$ ), the last term represents the diffusion of the absolute velocity in the diffuser and accounts for about one-third of the work input.

#### 2.4. Head Rise

The adiabatic head  $H_{ad}$  represents the energy transferred through a turbomachine per unit mass of fluid. If a compressor produces 1 m of head, it means that 1 kg-force will be required to elevate 1 kg of gas mass to a height of 1 meter. For an incompressible flow, the head is expressed by

$$\Delta H_{ad} = \frac{\Delta P}{\rho}$$

where  $\Delta P$  is the pressure rise, and  $\rho$  the density.

For compressible flow, the average density between inlet and exit must be used in the equations. An exact relation for a compressible flow, considering an ideal gas and an isentropic process, is given by

$$\Delta H_{ad} = \frac{\gamma R}{\gamma - 1} \Delta T_{ad}$$

where, for a compression process

$$\Delta T_{ad} = T_1 \left[ \left( \frac{p_2}{p_1} \right)^{\frac{\gamma - 1}{\gamma}} - 1 \right]$$

The head, the enthalpy rise, or the pressure ratio are quantities used to express the energy exchange into the impeller. They can all be used interchangeably.

#### 2.5. Efficiency

The first principle of thermodynamics in its complete form relates the work input  $\dot{W}$  and heat exchanged  $\dot{Q}$  to the change in total enthalpy and altitude z as follows:

$$\frac{\dot{Q} - \dot{W}}{\dot{m}} = \left[ h + \frac{C^2}{2} + gz \right]^2 = \left[ c_p T_0 + gz \right]^2$$

Neglecting the change in altitude, the heat loss, and considering a perfect gas, the change in energy is directly related to the change in total temperature. It is then natural to represent the compression process in a T-S diagram.

It is easy to show (e.g. Wilson 1984) that the slope of each line increases with increasing temperature. A typical compression process is shown in Figure 2.5.

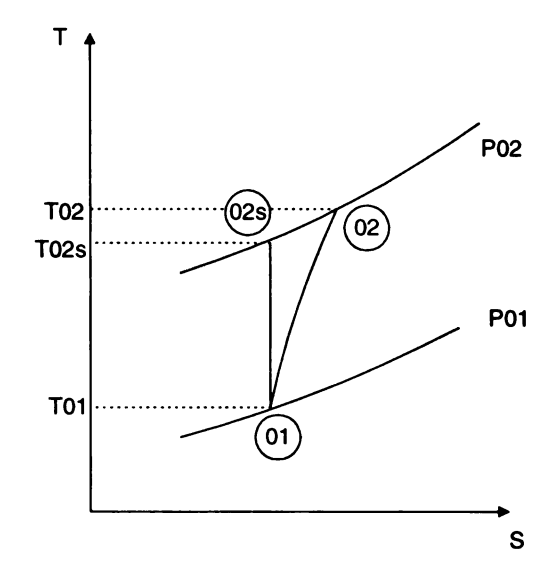


Figure 2.5 Representation of a compression process in a T-S diagram

The isentropic efficiency compares the actual enthalpy change during the compression process to the one that would have taken place for an isentropic process. It is defined by

$$\eta_{is} = \frac{h_2 - h_1}{h_{2s} - h_1}$$

State 1 generally refers to the total conditions at the inlet. State 2 corresponds to the exit conditions. If total conditions are used at state 2, the total-to-total isentropic efficiency is obtained. If static conditions are used, it is the total-to-static isentropic efficiency. The difference between these two efficiencies will be large for stages having a large exit velocity. Depending on the type of application, one efficiency or the other will be used. Generally, if the exit velocity is used for a purpose (as in a jet-engine for example) the total-to-total efficiency is used; if the exit velocity is not used, the total-to-static efficiency is used. For a perfect gas with constant specific heat, the expression for the efficiency becomes

$$\eta_{is} = \frac{C_p (T_{02is} - T_{01})}{C_p (T_{02} - T_{01})} = \frac{\left(\frac{P_{02}}{P_{01}}\right)^{\frac{y-1}{y}} - 1}{\frac{T_{02}}{T_{01}} - 1}$$

Note that the isentropic efficiency depends on the inlet conditions and the pressure ratio.

A representation of the isentropic efficiency is shown in a T-S diagram in Figure 2.5.

#### 2.6. Work Reduction Factor and Slip Factor

The flow at the exit of the impeller does not follow the blade. A parameter is introduced to compare the actual absolute tangential velocity to the one obtained in the case of an infinite number of blades where the flow would follow the blade. This parameter is called the work reduction factor  $\mu$ 

$$\mu = \frac{C_{u2}}{C_{u2}^{\infty}}$$

This quantity directly influences the estimation of the enthalpy rise in the compressor.

The Euler equation is now rewritten as follows:

$$\Delta H = \mu U_2 C_{u2}^{\infty}$$

assuming no inlet prewhirl. The corresponding velocity triangles are shown in Figure 2.6.

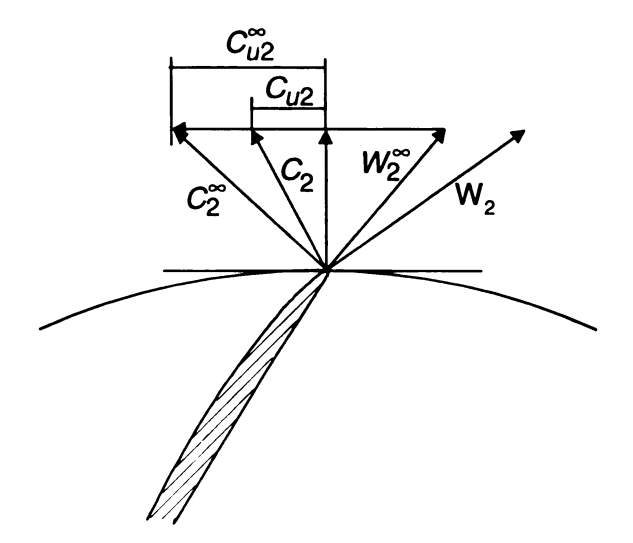


Figure 2.6 Impeller exit velocity triangle with and without slip

The other parameter commonly used in the literature is the slip factor  $\sigma$  defined

by

$$\sigma = 1 - \frac{C_{slip}}{U_2}$$

where  $C_{slip} = C_{u2}^{\infty} - C_{u2}$ 

The work coefficient and the slip factor are related through the following relation:

$$\sigma = 1 - \left(1 - \frac{C_{m2}}{U_2 \tan \beta_2}\right) (1 - \mu)$$

Many correlations are available in the literature to predict the value of the slip factor. One of the most commonly used is the one by Wiesner (1967)

$$\sigma = 1 - \frac{\sqrt{\cos \beta_{2b}}}{Z^{0.7}}$$

where  $\beta_{2b}$  is the exit blade angle and Z the blade number.

This equation is a data fit of the theoretical curves obtained by Buseman (1928) for inviscid flow in an impeller with logarithmic-spiral shaped blades. The validity of this

expression was checked by Wiesner with over 60 compressors and pumps with various blade angles and blade numbers, and compared to other correlations. The agreement was found to be fairly good, but this relation may be off by a few percents for some machines.

The effect of the blade angle and blade number on the slip factor is shown in Figure 2.7. The slip factor is seen to be smaller for a radial impeller that for a backward-swept impeller. It increases with increasing blade number.

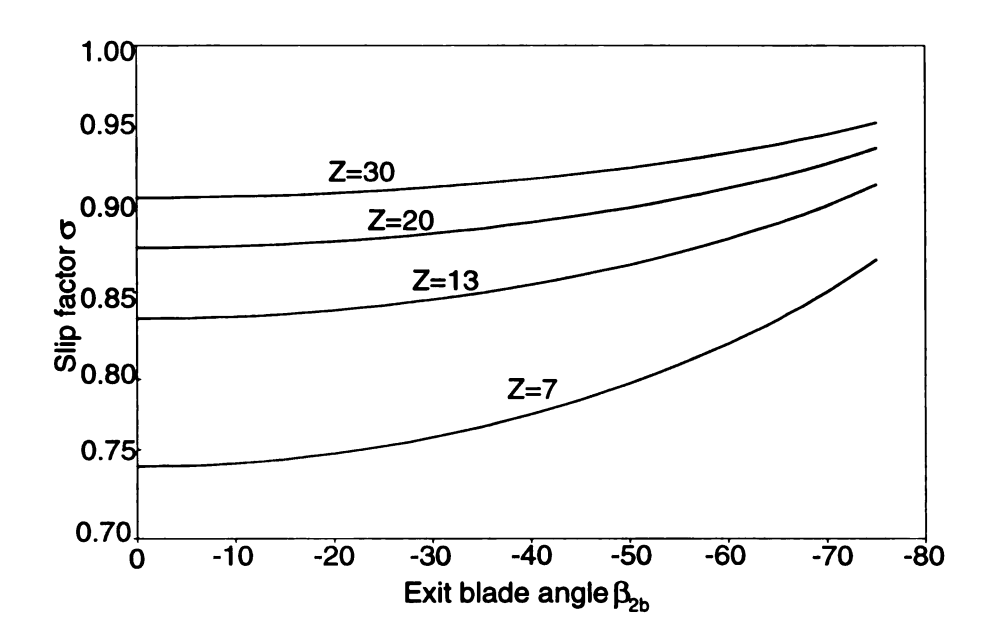


Figure 2.7 Influence of the blade number and the exit blade angle on the slip factor

#### 2.7. Operating Map and Compressor Range

The compressor performance consists of a plot showing the efficiency and pressure ratio versus. the mass-flow rate for different rotational speeds, or the head versus the volume-flow rate, or in a dimensionless form, the head coefficient versus the flow coefficient. A typical curve for a centrifugal compressor stage is shown in Figure 2.8.

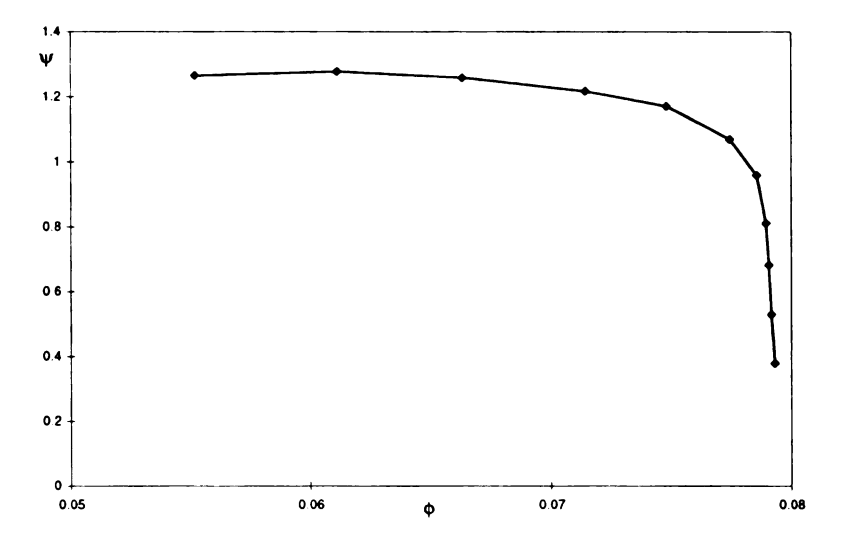


Figure 2.8 Typical centrifugal compressor head-flow curve

Three different regions may be distinguished. On the right is the choke limit obtained when sonic conditions are reached in the minimum section of the machine (impeller throat or diffuser throat). The choke limit appears as a vertical line in the compressor map because the efficiency and the pressure ratio drop drastically.

On the left is the stall region and surge line, which corresponds to a region of instability. Rotating stall is an unstable phenomenon often preceding surge. It can take place in the impeller or in the diffuser. Rotating stall is a local instability in which zones of separated flow, called cells, rotate in one component of the machine. When operating at a high pressure level, the pressure fluctuations corresponding to rotating stall generate mechanical vibrations that can severely damage the machine. Operation in this area should therefore be avoided. In the case of vaneless diffusers, the onset of this phenomenon has been correlated to the diffuser inlet flow angle (Senoo 1978).

During surge operation, oscillations of mass flow rate between the compressor exit and inlet occur that may damage the machine especially for high-density gas. Van den Braembussche (1984) showed that for a negative value of dΨ/dφ (i.e. increasing

pressure for decreasing mass flow) any perturbation will be damped out, resulting in a stable operating point. As soon as  $d\Psi/d\varphi$  is positive, the flow may become unstable depending on the characteristic of the global system (i.e. the compressor, but also the inlet and exit piping). The compressor should not be operated in this region.

At medium flow coefficient is a region of high efficiency, generally close to the design point, where the compressor should be operated.

#### 2.8. Dimensionless Parameters

As in any physical process, dimensional analysis and similarity considerations can be applied to turbomachinery. They state that for machines that are geometrically similar, similar velocity triangles will be obtained. Among the dimensionless groups that appear, the head coefficient, the flow coefficient, the efficiency, the specific speed, and the specific diameter are used.

Dimensional analysis can be used to compare data from different machines to predict the performance of an actual machine when the testing has been performed on a scale model, and to predict the performance at different speed line or operating flow point.

#### 2.8.1. Flow and head coefficient

The flow coefficient is defined by

$$\Phi = \frac{Q}{ND^3}$$

and the head coefficient by

w) in

d

a

a

1

2

ma

for

the

$$\psi = \frac{H}{N^2 D^2}$$

where Q is the volume flow rate, H is the head, N is the rotational speed, and D is the impeller diameter.

These two parameters are generally used to predict the off-design characteristic of a machine. The similarity does not hold close to the choke line and close to the surge line due to compressibility and viscous effect.

There are various definitions of  $\Phi$  and  $\Psi$ . The following definitions are used

$$\Phi_{in} = \frac{Q_{in}}{\frac{\pi}{4}D_{tip}^2U_2}$$

and

$$\Psi = \frac{H_{is}}{\frac{U_2^2}{2g}}$$

where  $Q_{in}$  is the inlet volume flow rate,  $H_{is}$  is the isentropic head produced by the machine,  $U_2$  is the peripheral speed at rotor tip, and g is the gravitational constant.

### 2.8.2. Specific diameter and specific speed

The specific diameter and the specific speed are another group of dimensionless parameters. They are a combination of the head and flow coefficient. They are used mainly for stage selection applications. Numerous correlations are available and allow for the selection of the type of machine (positive displacement, centrifugal, axial) required for an application.

The specific diameter is defined by

$$N_s = \frac{NV_1^{0.5}}{H_{ad}^{0.75}}$$

$$D_s = \frac{DH_{ad}^{0.25}}{V_1^{0.5}}$$

in which V<sub>1</sub> is the inlet volume flow rate.

The expression of the specific speed used in the text is

$$N_s = N \frac{Q_{in}^{0.5}}{H_{is}^{0.75}}$$

where N is in rpm, Q<sub>in</sub> in ft3/sec, H<sub>is</sub> in ft-lbf/lbm.

These definitions are not truly dimensionless. Letting  $\omega$  be in round per second, and replacing  $H_{ad}$  by  $(gH_{ad})$ , we get the following dimensionless definitions.

$$n_s = \frac{\omega \sqrt{V_1}}{(gH_{ad})^{0.75}}$$

and

$$d_s = \frac{D(gH_{ad})^{0.25}}{\sqrt{V_1}}$$

n<sub>s</sub> and d<sub>s</sub> have been correlated for best efficiency between different type of machines. Figure 2.9 taken from Balje (1981) shows the relation between peak efficiency and specific speed, and the application domain of different types of turbomachines.

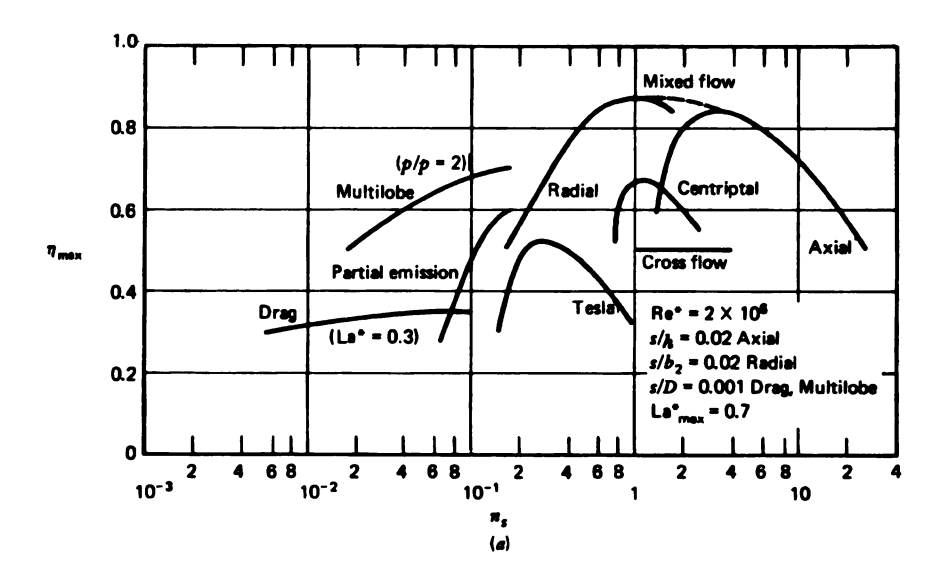


Figure 2.9 Maximum compressor and pump efficiencies as function of specific speed (Balje 1981)

Figure 2.10 shows the empirical relation between efficiency and specific speed for centrifugal impellers of the same family with similar geometrical layout (Rodgers, 1980). It clearly shows that there exists an optimum specific speed range.

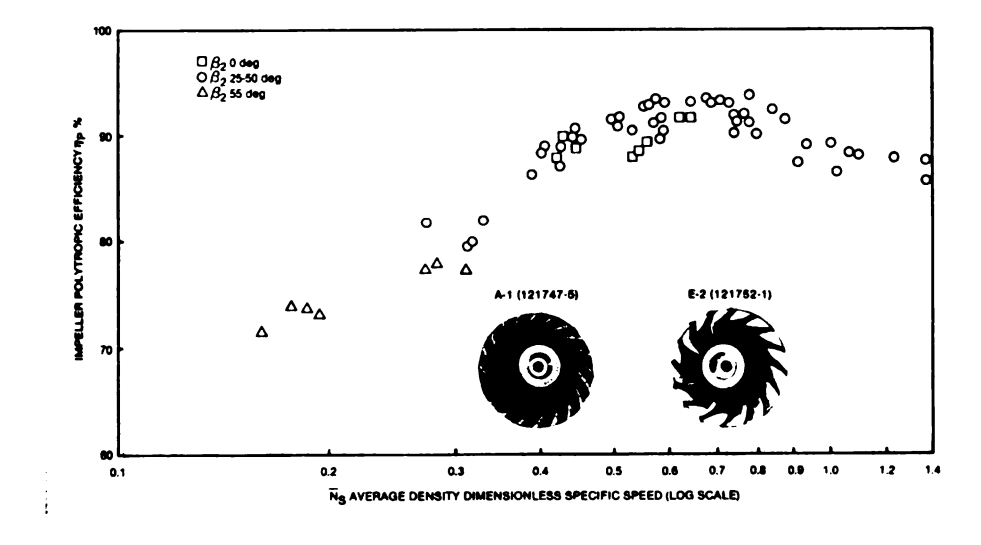


Figure 2.10 Test impeller efficiencies versus average specific speed (Rogers 1980)

er

3.

3.]

tur

The

diff

# 3. FLOW IN THE IMPELLER AND DESIGN PARAMETERS

The first part of this chapter gives initial insight into the detailed flow field in a centrifugal impeller. The Chapter starts with a review of the forces applied on a fluid element, followed by the typical secondary flows encountered. Experimental visualization of the flow field taken from the literature is then presented. It is also shown that Computational Fluid Dynamics (CFD) has become a valuable tool capable of qualitatively predicting the flow. In the second part, the different types of losses encountered in centrifugal compressors are summarized, and the main one-dimensional design parameters are reviewed.

# 3.1. Flow in the Impeller

# 3.1.1. Qualitative Description of the Flow in the Impeller

The flow in a centrifugal impeller is highly complex. It is three-dimensional, turbulent, viscous, and unsteady. The flow at the impeller exit is highly nonuniform and differs drastically from the one-dimensional picture presented in the previous chapter. The flow field in a typical centrifugal compressor is shown in Figure 3.1.

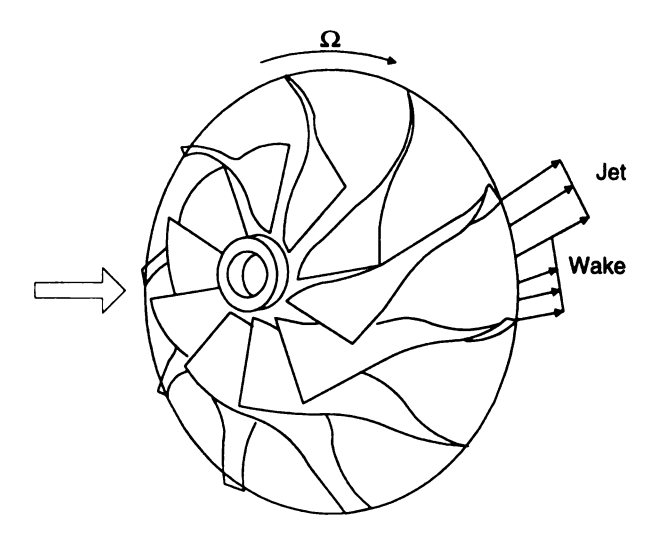


Figure 3.1 Schematic of compressor stage flow region

The flow enters the impeller through the inducer in which the relative flow is turned from the inlet direction to almost axial. The flow then enters the axial-to-radial bend. In this region, boundary layers and secondary flows have developed. As will be seen later, Coriolis forces and streamline curvature contribute to the destabilization of the flow. Two regions develop in the flow field: one with a high relative Mach number called a jet and one with a low relative Mach number called a wake. After exiting the impeller, the two regions mix rapidly due to the difference in angular momentum and enter the diffuser.

### 3.1.2. Inviscid Flow Analysis

Although the viscous effect can not be neglected when analyzing the flow in a centrifugal impeller, an inviscid analysis provides good insight into the forces applied to a fluid element moving into a blade channel. Simple but important physical knowledge can be gained.

b Ō no pe The equation of motion for the relative flow, assuming an inviscid flow with no body force, is given by

$$\frac{D\vec{w}}{Dt} + 2\vec{\omega} \times \vec{w} + \vec{\omega} \times \vec{u} = \frac{\nabla p}{\rho}$$

$$\downarrow \qquad \qquad \downarrow \qquad \qquad \downarrow$$
Relative Coriolis Centrifugal acceleration acceleration acceleration gradient

In this equation,  $\vec{w}$  represents the relative velocity,  $\vec{u}$  is the peripheral speed and  $\vec{\omega}$  is the angular velocity.

In a streamline coordinate system (s, n, b), where s is along the streamline, n is normal to the streamline in the blade-to-blade surface, and b is the binormal perpendicular to s and n, the projection of the equation of motion in the n-direction is

$$-\frac{w^2}{R_n} + 2\omega w - \omega u \cos \beta = \frac{1}{\rho} \frac{\partial p}{\partial n}$$

The different forces applied to a fluid particle are shown in Figure 3.2.

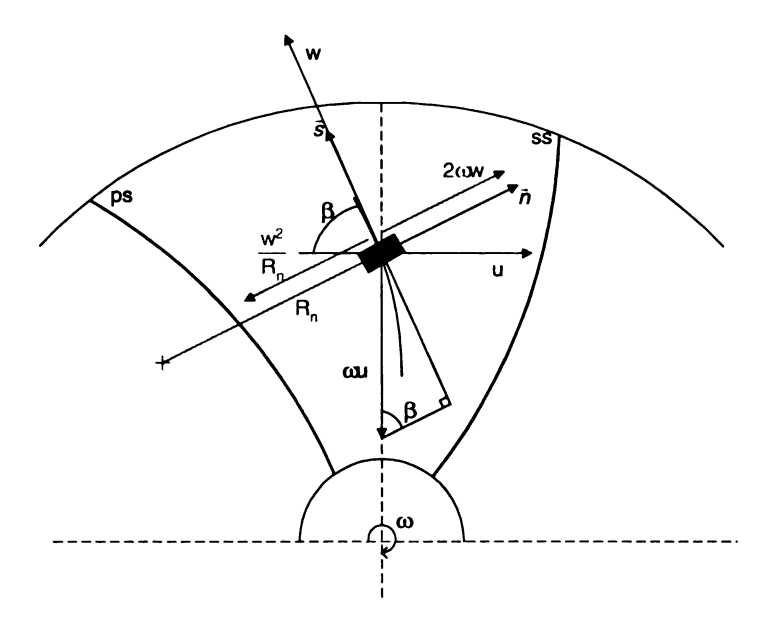


Figure 3.2 Forces acting on a fluid element inside an impeller passage

By combining the energy equation and the equation of motion, Krain (1984) derived the following approximate relation, which relates the velocity difference between the pressure side and the suction side of the blade to the mean velocity, the rotational speed and the radius of curvature (Appendix A).

$$w_{ss} - w_{ps} = \left(2\omega - \frac{w_{mean}}{R_n}\right) \Delta n \tag{3.1}$$

This approximate relation shows that

- the velocity varies almost linearly from pressure to suction side
- the velocity gradient results from the contribution of the blade curvature and of the
   Coriolis forces
- the velocity difference between pressure side and suction side is smaller for a
  backswept impeller (R<sub>n</sub>>0), than for a radial impeller (R<sub>n</sub>=∞) and for a forward
  leaning impeller (R<sub>n</sub><0). This is illustrated in Figure 3.3.</li>

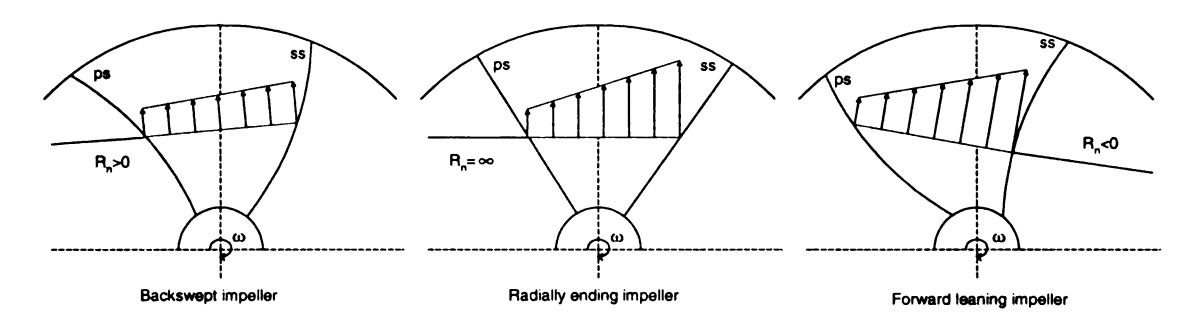


Figure 3.3 Velocity distribution in impeller passage – Inviscid analysis (adapted from Krain 1984)

Equation 3.1 has another important consequence. If we consider a blade passage with a sufficiently high radius of curvature, the last term on the right-hand side can be neglected, leading to

$$w_{ss} - w_{ps} = (2\omega)\Delta n$$

This shows that there exists inside the passage a forced vortex of strength  $2\omega$  rotating in a direction opposite to the rotor. The force created by this vortex explains why the flow does not follow the blade at the impeller exit.

The equation of motion in the meridional plane is given by

$$\frac{1}{\rho} \frac{\partial p}{\partial z} = \frac{c_m^2}{R_z} - \frac{c_u^2}{r} \cos \varepsilon \tag{3.2}$$

where  $\varepsilon$  is the local angle of the streamline considered with the axis of rotation. Close to the impeller exit, the streamline is almost radial (i.e.  $\varepsilon \cong 90^{\circ}$ ); the last term in (Eq.3.2) can be neglected with respect to the others. The equation of motion then expresses the balance between the streamline curvature force and the pressure gradient. The radius of curvature of the meridional contour is positive. The pressure gradient with respect to z is then positive, and the expected meridional velocity distribution is shown in Figure 3.4.

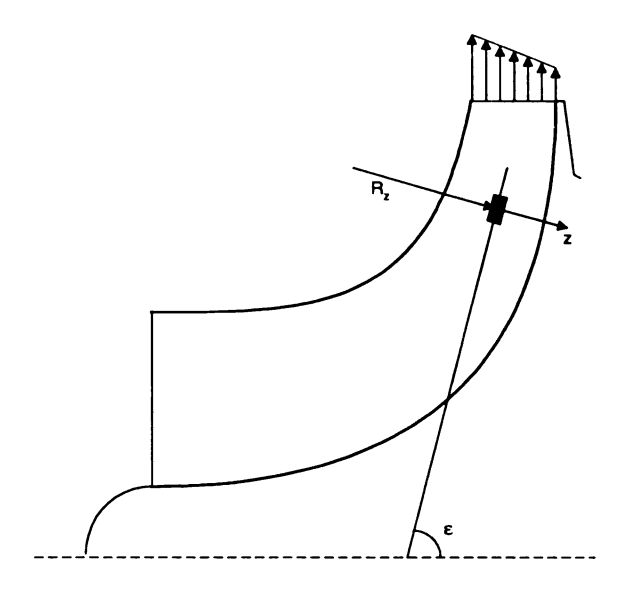


Figure 3.4 Flow in the meridional plane near impeller exit – Inviscid analysis (after Krain 1984)

This distribution of meridional velocity is not what is necessarily observed, as will be seen in the next sections. A more advanced treatment is required to predict the exit flow field.

### 3.1.3. Secondary Flows

Secondary flows are defined as the difference between the full three-dimensional inviscid solution and the real flow occurring in a component of the compressor (Van den Braembussche 1985). The fluid particles inside the boundary layer have a lower velocity, but they are submitted to the same pressure gradient as the main flow. This imbalance between the normal pressure gradient and the centripetal acceleration will therefore move the flow inside the boundary layer in a different direction than the main flow. This is called a secondary flow by contrast with main or principal flow.

Secondary flows induce cross-flows, and therefore secondary vorticity. Hawthorne (1974) developed an expression for the development of the streamwise vorticity in an incompressible and frictionless flow.

$$\frac{\partial}{\partial s} \left( \frac{\Omega_s}{w} \right) = \frac{2}{\rho w^2} \left( \frac{1}{R_n} \frac{\partial p^*}{\partial b} + \frac{\omega}{w} \frac{\partial p^*}{\partial z} \right)$$
(3.3)

In Equation (3.3),  $\Omega_s$  represents the streamwise vorticity,  $\omega$  is the rotational speed, z is the axial direction, and  $p^* = p + \frac{1}{2}\rho W^2 - \frac{1}{2}\rho U^2$  the rotary stagnation pressure. The rotary stagnation pressure is constant along a streamline for a steady, inviscid, incompressible flow similarly to the total pressure along a streamline for a steady incompressible frictionless flow. The rotary stagnation pressure reduces only because of losses. As shown by Johnson (1978), the secondary flows tend to move the low

momentum fluid towards regions of stable location which correspond to minimum reduced static pressure  $P_r = P - \frac{1}{2}\rho\omega^2 r^2$  (or relative Mach number).

From Equation (3.2), it can be seen that streamwise vorticity will be generated when a gradient of rotary stagnation pressure in the binormal direction (together with curvature) or in the axial direction (together with rotation) is present. Hence, even if the secondary flows are essentially due to the presence of the boundary layer, they can be accounted for in an inviscid analysis if the gradients of rotary stagnation pressure present at the inlet are introduced into the model.

Johnson (1978) investigated the flow in rotating bends using secondary flow theory. The movement of the low p\* fluid in the boundary layer of the impeller passage is shown in Figure 3.5. In the inducer, the boundary layers are thin, and only small secondary flows may occur. If the contribution of the blade curvature is large enough, then some vorticity will be created along the streamwise direction on the pressure side and suction side that will take the low p\* fluid from the boundary layer to the shroud (Figure 3.5). It is only when the flow starts to deviate from the axial direction to the radial direction that the secondary flows become consequent.

In the axial-to-radial bend, both Coriolis and streamline curvature are acting on the flow with equivalent strength. The boundary layers have now developed. The meridional curvature on the blade surface is in the direction of vorticity. Secondary flow transports the low-momentum fluid from the hub to the shroud.

ſ

C

3.

pre

CO1

gra

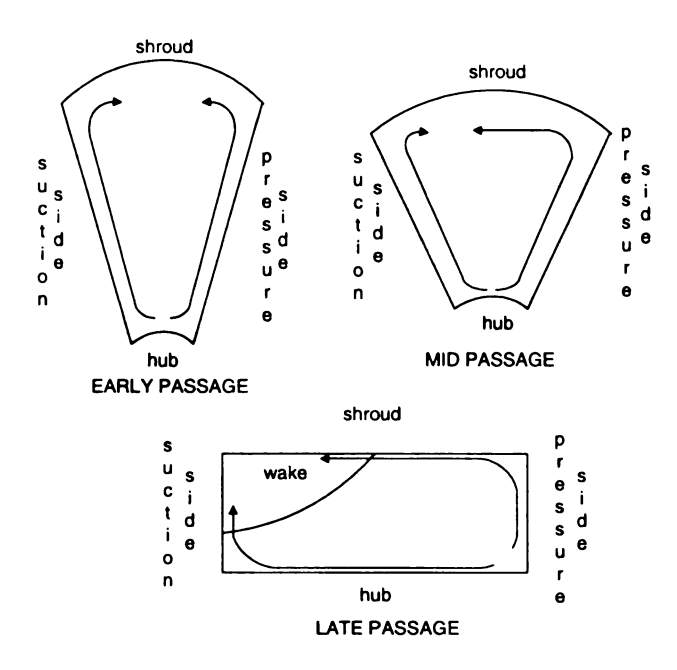


Figure 3.5 Movement of low p\* fluid in the boundary layer in an impeller passage (after Johnson 1978)

In the radial part of the impeller, Coriolis forces dominate, which results in secondary flow into the blade-to-blade plane. An accumulation of low-momentum fluid may take place in the shroud-suction region.

The flow characteristics revealed by secondary flows have been experimentally confirmed, as will be seen in section 3.1.5.

# 3.1.4. Effect of Rotation and Streamline Curvature on Boundary Layer Stability

Rotation and curvature are responsible for the stability of the boundary layer. The boundary layer on the suction side is stabilized by Coriolis forces while the one on the pressure side is destabilized. To understand qualitatively this phenomenon, let us consider a particle in the blade-to-blade plane that is in equilibrium between the pressure gradient and the Coriolis forces in a radial impeller with straight blades.

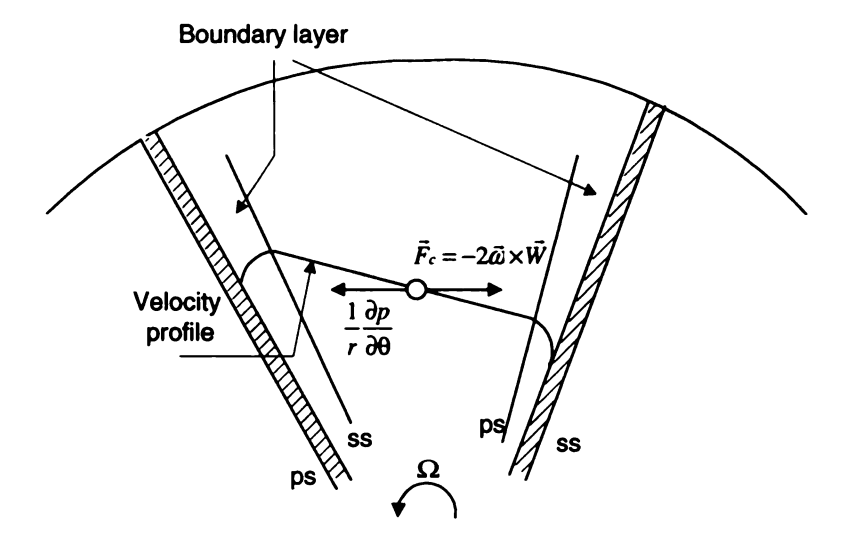


Figure 3.6 Simplified representation of the flow between two radial blades

Figure 3.6 represents a fluid particle in equilibrium in the center of the blade passage. Assume that a particle near the pressure side is perturbed and moved to an adjacent layer on the left while retaining its original velocity. Its velocity will then be lower than the velocity of a particle in equilibrium, and the Coriolis force applied to this particle will not be able to balance the pressure gradient. The particle will therefore move towards the suction side. For a particle moved out of the boundary layer on the suction side, the pressure gradient will send it back to the suction side. We see that, qualitatively, all low momentum particles will accumulate on the suction side.

The boundary layer on a convex plane is stabilized (i.e. laminarized) by centrifugal forces, whereas the one on a concave plane is destabilized (i.e. more turbulent). The laminarized boundary layer is more likely to separate under the action of the adverse pressure gradient than the one at the hub.

The same reasoning would explain the stabilization/destabilization in the meridional plane due to centrifugal forces, and therefore, why low momentum fluid may accumulate on the shroud side. Figure 3.7 summarizes the different possible cases.

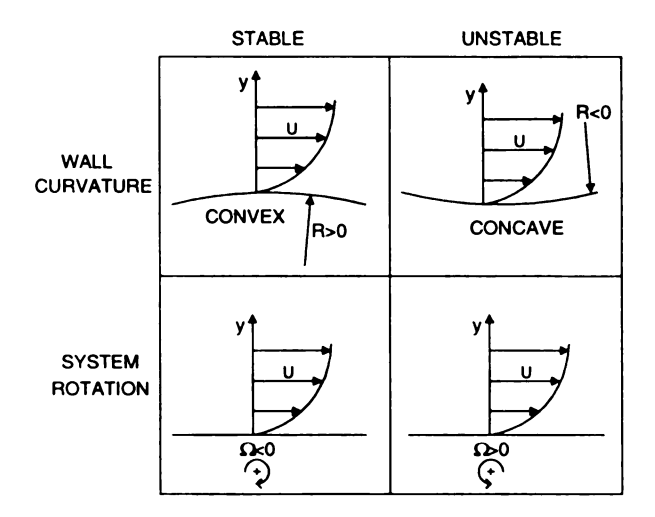


Figure 3.7 Definition of stable and unstable cases (after Johnston and Eide 1976)

Two non-dimensional numbers can be used to express the sign and magnitude of each effect. They are the gradient Richardson numbers given by

$$Ri_C = 2\left(\frac{W}{R}\right) \left(\frac{\partial W}{\partial y}\right) \text{ and } Ri_\Omega = 2\Omega \left(\frac{\partial W}{\partial y}\right)$$

Ri>0 corresponds to a destabilization (i.e. a reduction in turbulent kinetic energy compared to the normal state of flow with no rotation and curvature, Ri=0). Ri<0 has the opposite effect.

# 3.1.5. Experimental Observation

Quantitative information at the impeller exit is very difficult to obtain.

Measurements with classical probes like Pitot tubes are only approximate due to their intrusive character (especially in narrow passages) and to the unsteadiness of the flow. It

is only since the mid-seventies that laser velocimetry measurements have been performed in a high-speed impeller beginning with Eckardt (1976). Figure 3.8 shows the optical measurement planes (denoted I-V) where the velocities have been measured.

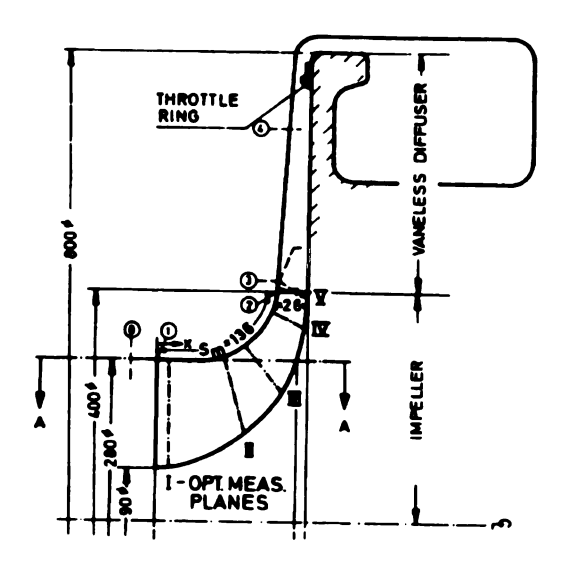


Figure 3.8 Optical measurement planes (Eckardt 1976)

Figure 3.9 shows for the radial impeller at its design point the evolution of the meridional velocity distribution (referred to the exit peripheral speed) at five different stations from impeller inlet to exit. For the sake of clarity, each measurement section along the blade has been represented as a trapezoid in which the blade spacing and width are equally spaced. From station I to II, the flow follows the blade and develops as predicted by the inviscid theory. Starting at station III, a first distortion can be noticed in the shroud stream-tube. The deficit in velocity develops rapidly in section IV and V. The area in the shroud suction side corner, often referred to as "wake", is characterized by

- a low mass-flow component of the order of 15% of the total mass flow
- a high-fluctuation intensity (up to four times higher than in the main stream)

- a steep, relatively stable velocity gradient to the surrounding flow characteristic of the separated flow.

These measurements confirmed an earlier impeller model proposed by Dean and Senoo (1960) stating that the flow does not remain attached to the blade and is in fact composed of two regions: one at high speed (jet) and one of low-momentum fluid (wake). The suction-side separation is an accumulation of low energy fluid and does not show any return flow.

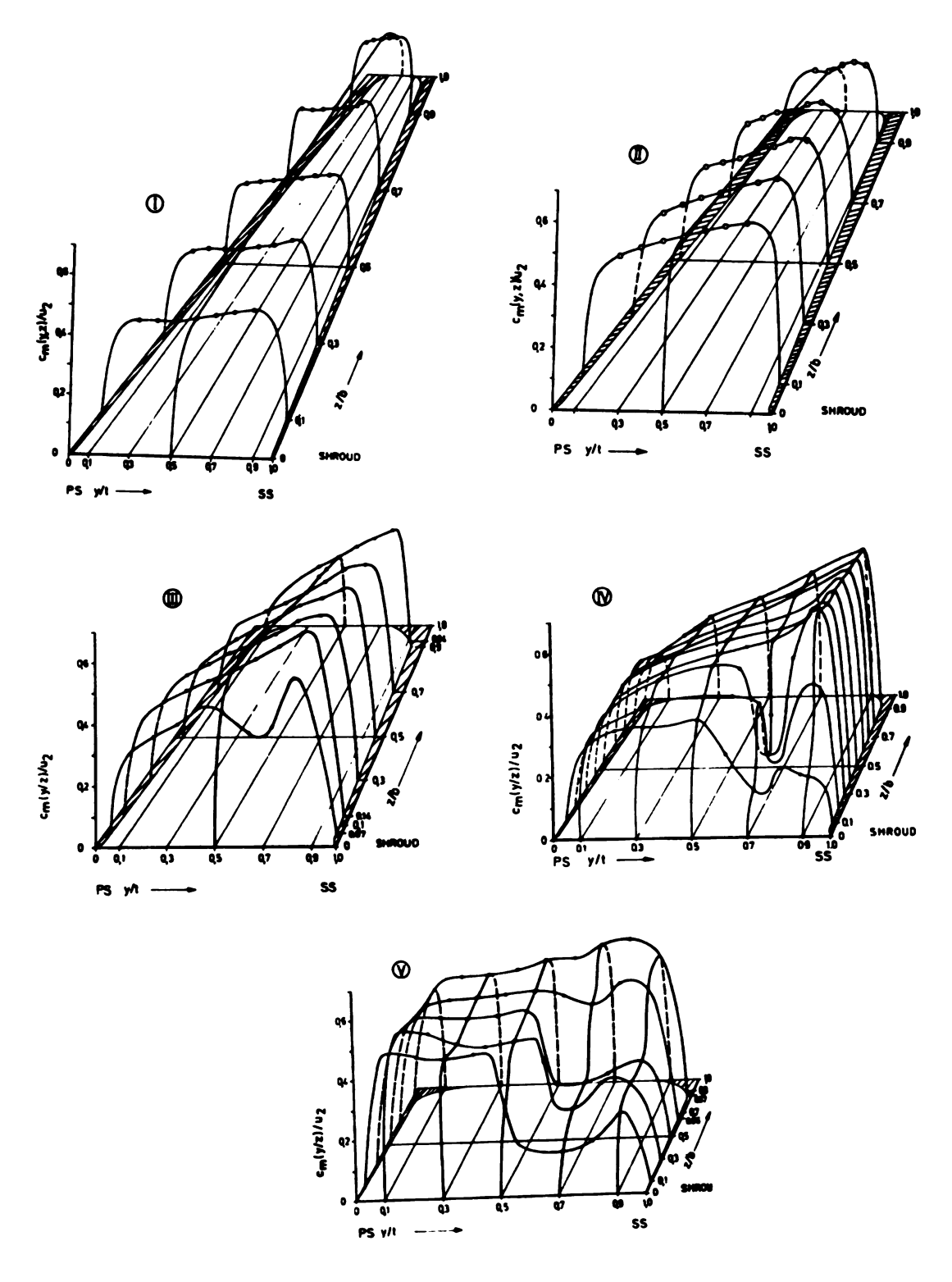


Figure 3.9 Non-dimensional velocity distribution at five stations along the impeller (Eckardt 1976)

Further studies showed that in a backswept impeller, the curvature of the blades minimizes the jet/wake phenomenon (Eckardt 1980 or Farge and Johnson 1990). Eckardt (1980) measured the flow in an impeller with 30° backsweep. Figure 3.10 shows the meridional velocity at measurement planes IV and V. Compared to Figure 3.9, it can be seen that the jet/wake pattern was also present but appeared to be weaker. Krain (1988) confirmed this trend. Better conditions were provided at the entrance of the diffuser, therefore improving the performance of the diffuser.

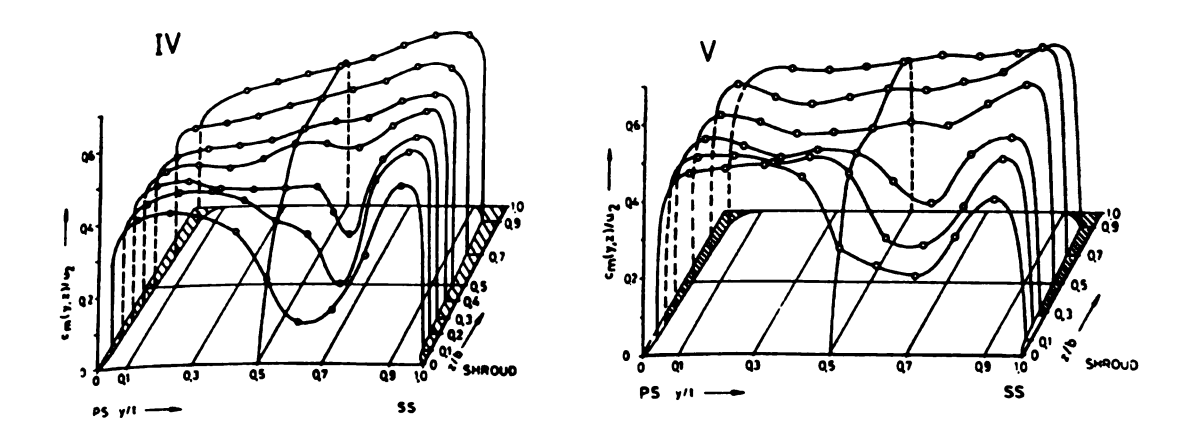


Figure 3.10 Normalized meridional velocity in backswept impeller (Eckardt 1980)

Johnson and Moore (1983) studied the influence of the mass-flow rate on the jet/wake structure. They measured pressure and velocity at five different stations of an impeller similar to the one used by Eckardt. The probes were rotating with the impeller. They found that the wake was located on the suction surface at low flow rate, at the suction surface/shroud corner at design point, and on the shroud at higher mass-flow rate. The relative strength of the secondary flow was related to the Rosby number  $Ro = \frac{W}{\omega R_A}$ , which characterized the ratio of Coriolis to inertial forces in the relative flow.

Figure 3.11 to Figure 3.13 show the rotary stagnation pressure below, at, and above the design flow rate. The regions of low p\* can be seen in Figure 3.11 to Figure

3.13. They indicate the location of the wake. Thus, it is seen that the relative magnitude of secondary flows due to curvature and rotation govern the position of the wake.

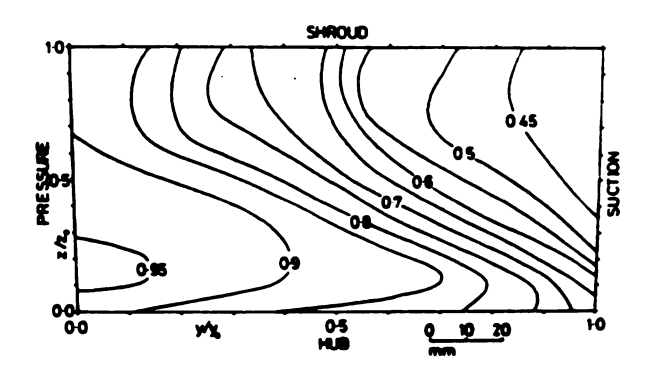


Figure 3.11 Rotary stagnation pressure at impeller exit, below design point (Johnson and Moore 1983)

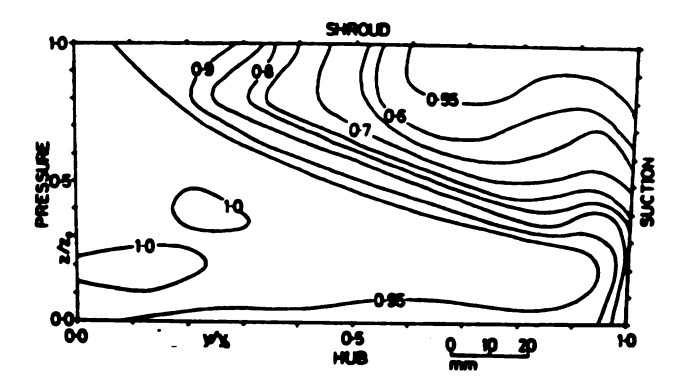


Figure 3.12 Rotary stagnation pressure at impeller exit, at design point (Johnson and Moore 1983)

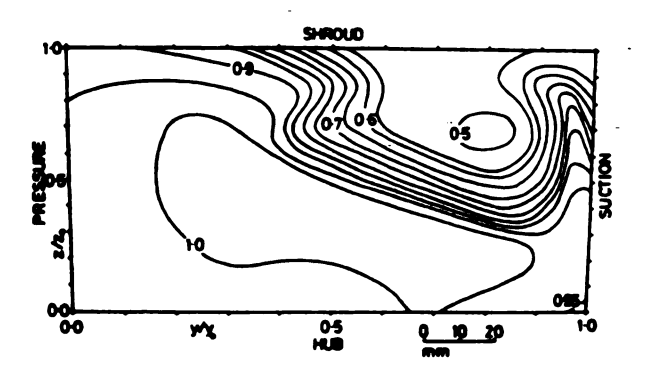


Figure 3.13 Rotary stagnation pressure at impeller exit, above the design point (Johnson and Moore 1983)

Casey et al. (1992) investigated numerically the flow field on an impeller typical of those found in multistage centrifugal machine and for which detailed experimental data were available. They used two 3-D viscous codes, the Denton LOSS3D code and the Dawes BTOB3D code. Both codes overestimated the static pressure rise, especially at low mass-flow rate; but they were overall in very good agreement with the measurements. Concerning the impeller flow field, the magnitude of the exit wake at the impeller outlet was well predicted although its position was closer to the suction side than its measured position. The calculated secondary flows showed the tendency of the flow on the blade surfaces to move towards the shroud. The main stream moved slightly toward the hub in order to compensate for the shift in mass flow in the surface boundary layers. This pattern was very similar to the one developing in rotating axial-to-radial bend (Johnson 1978) where secondary flows are dominated by centrifugal forces (Figure 3.5). CFD was therefore able to provide detailed information in regions where accurate measurements are very difficult to make.

Hathaway et al. (1993) measured the flow in a low-speed centrifugal impeller experimental facility. They used laser anemometry to measure the three-dimensional velocity field. Their optical measurement data were asserted by means of 5-hole probes, hot-wire anemometry, and surface flow visualization. The Dawes code was used to analyze the impeller. The movement of the low momentum fluids near the blade surface towards the tip of the blade predicted by the CFD was confirmed by the laser measurements. This showed the capacity of the CFD to capture the flow physics. These results obtained on a low-speed impeller were shown to be in qualitative agreement with

the measurement performed by Krain (1988) on a subsonic high-speed 4:1 pressure ratio impeller.

# 3.2. Losses in a Centrifugal Compressor

The losses in a centrifugal compressor can be classified into two categories: internal and external. The internal losses are those due to incidence, diffusion, friction, blade loading, wake mixing. The external losses are disk friction losses and seal losses.

# 3.2.1. Internal Losses

# **3.2.1.1.** Incidence

There is only one operating point at which the flow will move smoothly into the blade. Away from this point, there exists a difference between the flow angle and the blade angle. There is generally a range of incidence for which the losses are minimum. Figure 3.14 shows the losses with respect to incidence for a two-dimensional cascade as reported by Lieblein (1965).

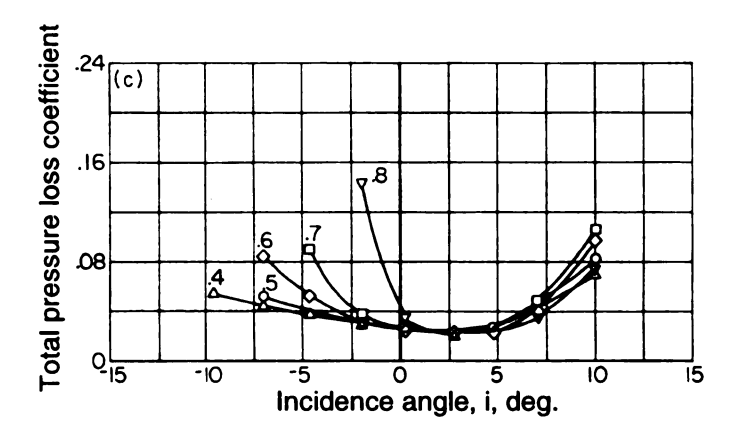


Figure 3.14 Effect of inlet Mach number on loss coefficient (Double circular arc blade cascade) Lieblein 1965

Note that the optimum incidence is a function of the Mach number and has a tendency to increase as the Mach number increases.

#### 3.2.1.2. Friction Losses

The viscous boundary layers are responsible for the friction losses. In a first approximation, the expression developed for pipe flow can be used to estimate the loss in total pressure due to friction. The classical expression is

$$\frac{\Delta p_0}{\rho} = 4C_f \frac{L}{2D} W^2$$

where  $\Delta p_0$  is the loss in total pressure,  $\rho$  is the density, L is the passage length, D is the hydraulic diameter, W is the velocity, and  $C_f$  is the friction coefficient

The main problem is to determine the value of C<sub>f</sub>. For pipe flow, the Moody chart is used to find the friction coefficient as a function of the Reynolds number and the relative roughness. Various expressions have been proposed in the literature and are not necessarily more accurate.

The interest of this relation is to show the importance of

- decelerating the relative flow as soon as possible
- maintaining the flow passage as short as possible
- keeping the hydraulic diameter of the passage as large as possible

Maintaining the passage as smooth as possible has also been shown to be beneficial, especially in narrow passages.

# 3.2.1.3. Diffusion and Blade Loading Losses

The boundary layers in compressors are subject to an adverse pressure gradient.

They are therefore more likely to separate as the flow develops along the blade. In order to prevent or to limit the separation of the flow, the diffusion of the flow must be limited.

A criterion commonly used to measure the diffusion level is

$$D = \frac{W_{\text{max}} - W_2}{\overline{W}}$$

A blade loading coefficient is used to quantify the amount of secondary flow. It is defined by

$$BL = \frac{w_{ss} - w_{ps}}{\frac{w_{ss} + w_{ps}}{2}}$$

The optimization of the velocity distribution and hence of the blade loading on a blade is a difficult and controversial issue. Dallenbach (1961) proposed a set of guidelines to apply when designing a conventional radial impeller based on some aerodynamic considerations on an airplane wing.

From boundary layer calculations on an airplane wing with various constant velocity gradients, it has been shown that "when decelerating at a slow rate, the boundary layer displacement thickness is considerably larger than when the same final velocity is

reached at a fast rate of deceleration. Since a thick boundary layer is unstable, particularly for entry into the diffuser, an initial rapid rate of deceleration seems to be desirable" (Dallenbach 1961). Thus, the preferred condition is a rapid deceleration of the mean velocity at the shroud followed by a slower rate near the outlet. This will lead to a decrease in the velocity at the hub that could generate reversed flow at the hub depending on the rate of deceleration used and the meridional shape of the impeller (curvature).

Also, it is worth mentioning that, as the friction losses are proportional to the square of the relative velocity, one should reduce the velocity as soon as possible.

As the boundary layer gets rapidly thinner on the pressure side due to secondary flows, a rapid deceleration should not be a problem (Dallenbach 1961). The flow inside the impeller will generally separate on the suction side when it gets closer to the impeller exit, limiting the pressure rise. This jet-wake flow pattern (in which no further pressure rise is achived by diffusion) will be established quickly if the blade to blade pressure difference inside the channel is large. Consequently, a light loading should be used close to the impeller exit. To achieve the desired pressure ratio, the higher loading should then be applied before the expected separation point. As the boundary layer gets bigger and more sensitive to separation as the fluid moves towards the impeller outlet, the higher loading should be applied shortly after the inlet to avoid boundary layer separation and together with a reduction of the mean velocity to maintain the peak velocity on the suction side at the minimum possible value. The maximum loading should not exceed a value around 0.65.

### **3.2.1.4. Separation Losses**

As mentioned in the previous section, high friction losses will take place as the boundary layers develop along the blade passages. The boundary layer may even separate. No further pressure rise will be achieved in the separated area, and higher losses are expected.

Nevertheless, some designers (e.g. Dean 1974) consider that a high-performance impeller will have a separated zone, which must, therefore, be modeled into the design process. The two-zone model presented in Chapter 4 uses this approach.

# 3.2.1.5. Secondary Flows

Secondary flows in centrifugal compressors have been discussed in section 3.1.3. They contribute to the deterioration of the performance by different means (Lakshminarayana 1996). They generate cross-flow velocities enhancing the three dimensionality of the flow field. They contribute to the destabilization of the flow, hence eventually promoting the separation of the flow near the shroud-suction side region. They also affect the turning of the flow and in turn the associated pressure rise in the machine.

# 3.2.2. External Losses

#### 3.2.2.1. Disk Friction

The torque required to rotate the impeller increases due to the presence of flow between the impeller disk and the non-rotating casing. Daily and Nece (1960) have investigated the torque required to rotate a smooth plane disk into an enclosed chamber.

Their results give a correlation between the torque coefficient, the relative roughness, and the Reynolds number calculated at impeller exit

$$C_{M} = \begin{cases} 3.7 \left(\frac{\varepsilon}{r_{2}}\right)^{0.1} \text{Re}^{0.5} \text{ for Re} < 3*10^{5} \\ 0.102 \left(\frac{\varepsilon}{r_{2}}\right)^{0.1} \text{Re}^{0.2} \text{ for Re} > 3*10^{5} \end{cases}$$

where Re= $U_2r_2/v$ 

The head loss due to disk friction is then expressed as

$$\Delta q_{DF} = k\overline{\rho} U_2 r_2^2 \frac{C_M}{\dot{m}} \approx k U_2 r_2^2 \frac{C_M}{Q}$$

where k is a coefficient between 0.13 and 0.25, depending on the author.

In a multi-stage machine, the volume flow rate decreases as the flow passes through the machine. The disk friction losses are therefore higher in the last stages, i.e. in the low-flow coefficient stages. At a design level, it can only be recommended to maintain the disk surface as smooth as possible.

# 3.2.2.2. Leakage Losses

Leakage losses represent the head loss due to the flow passing through the running clearance between the rotating element and the stationary casing part. It takes place between the casing and the impeller at the impeller eye, between two consecutive stages in a multistage machine.

# 3.3. One-Dimensional Design Parameters

# 3.3.1. Overall View of the 1-D Design Parameter

Figure 3.15 shows the main geometrical parameters defining the impeller:

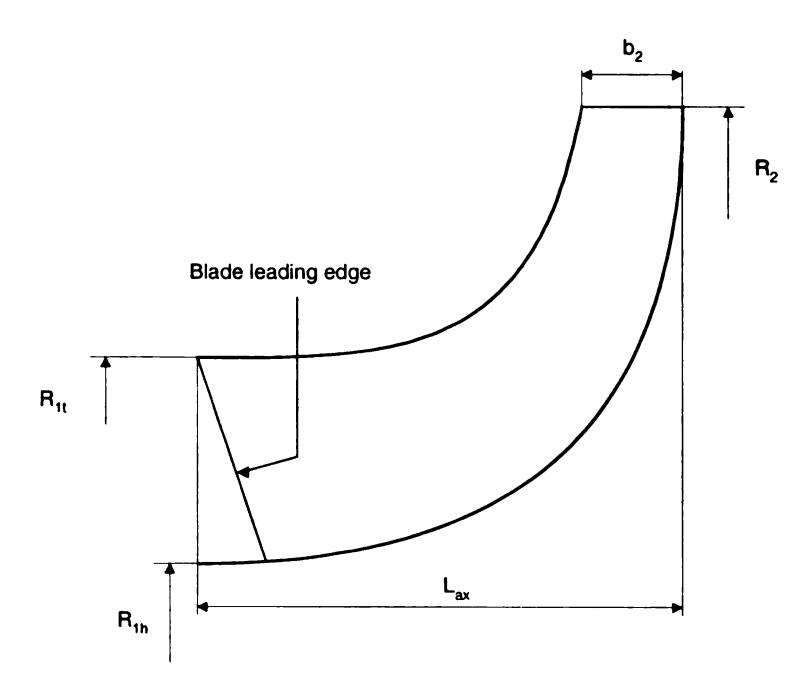


Figure 3.15 Impeller main geometrical parameters

- hub radius R<sub>1h</sub>
- shroud (or tip) radius R<sub>1t</sub>
- blade angle distribution from inlet to exit and from hub to shroud
- impeller exit radius R<sub>2</sub>
- impeller exit width b<sub>2</sub>
- blade number Z
- impeller axial length Lax

The main aerodynamic parameters are:

• velocity ratio W<sub>2</sub>/W<sub>1</sub>

- exit flow angle
- impeller exit Mach number
- choice of a slip factor for performance prediction

Table 1 shows some of the conventional limits on the inducer and impeller parameters given by Van den Braembussche (1987).

Table 3.1 Summary of the limitation on some main 1D parameters

Parameters	Critical range
$0.5 < R_{1t}/R_2 < 0.8$	Low values leads to long channel (friction)
	/ High values gives unsatisfactory meridional contour
b <sub>2</sub> /R <sub>2</sub>	Smaller values imply high friction and clearance
	losses
$0.3 < R_{1h}/R_{1t} < 0.5$	Balance between blockage and high inlet velocities
$\beta_{1t}$ < $70^{\circ}$	To avoid blockage and high turning in the inducer
65°<α2<80°	To avoid too tangential velocities at impeller exit
$W_2/W_1>0.6$	Smaller values will lead to boundary layer separation

Some of the design parameters will now be presented with respect to the development of low-flow coefficient compressors.

# 3.3.2. Inducer Hub and Tip Radius

The hub and tip radius of the inducer are determined as a function of the mass flow rate. Once the hub ratio is fixed, the tip radius is determined in order to minimize the Mach number at the tip. It will be seen in Chapter 4 that there always exists an optimum value of  $R_{\rm lt}$ .

The hub radius is determined most of the time by rotordynamics considerations. The effect of hub-to-outlet diameter ratio on the performance of a low-flow coefficient stage has been investigated by Paroubek et al. (1994). Three stage-configurations with a flow coefficient of 0.007 (A, B, and C) and three with a flow coefficient of 0.021 (D, E,

and F) have been tested. The A, B, and C impellers have the same exit width but a different inlet hub radius. Their meridional shape, blade geometry, and blade number have been chosen to maintain similar aerodynamic performance between them. The D, E, and F impellers have been derived from the A, B, and C impellers by increasing the blade width. All impellers have 60° backward-swept angle.

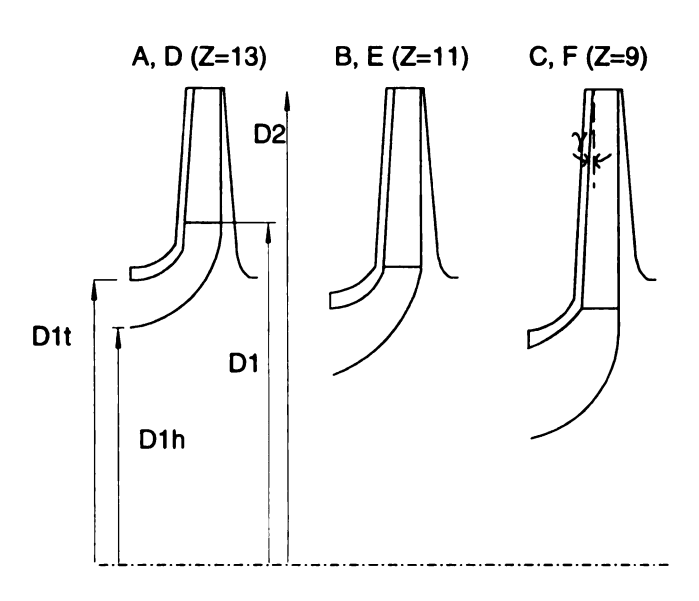


Figure 3.16 Impeller main dimension (after Paroubek et al. 1994)

Figure 3.17 shows the impeller efficiency for the tested stages. The hub-to-exit diameter ratio was found to have a stronger effect on the narrow impeller than on the wide stages. The impellers with the smallest hub diameter had the best performance: for the same relative outlet flow capacity, the deceleration is higher (i.e W<sub>2</sub>/W<sub>1t</sub> is lower) for impellers with greater hub diameters while it must be achieved on a shorter meridional contour.

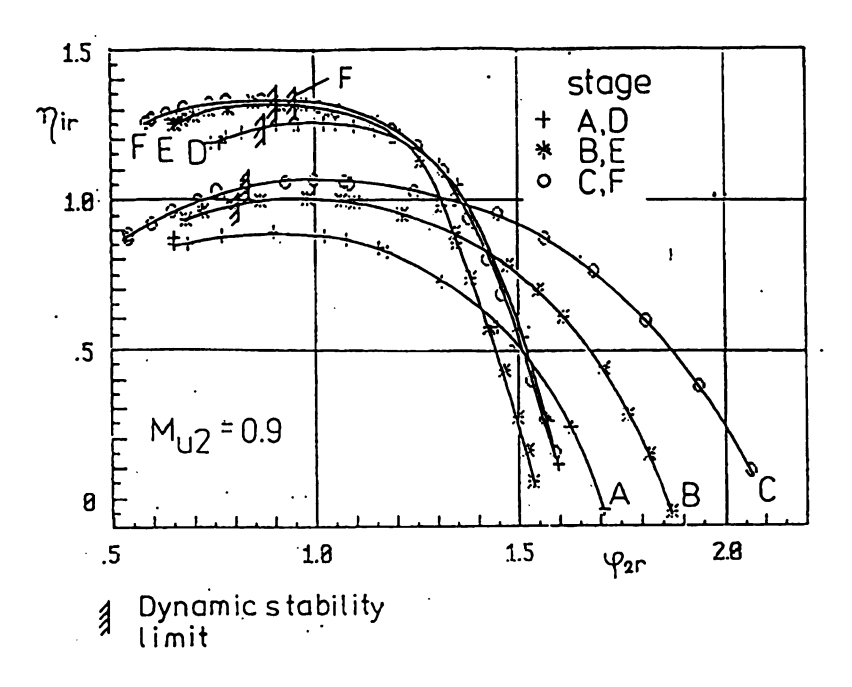


Figure 3.17 Impellers efficiency (Paroubek et al. 1994)

# 3.3.3. Exit Width

The exit width is determined based on the volume-flow rate passing at impeller exit. Based on the estimated density and the required head, the corresponding width can be determined with the continuity equation.

The effect of impeller width on the performance of low-flow coefficient stages has been studied by Paroubek et. al. (1994). The performances of the wider impellers (Figure 3.17) were, as expected, higher than the performances of the narrower ones due to the reduced friction losses. At high mass flow, the efficiency decreases faster for the wider stages. Their operating range is much smaller than the operating range of the narrow stages.

Casey (1990) suggested increasing the impeller width for a given impeller (the exit tip radius is kept identical) while adjusting the exit blade angle in order to keep the head rise capacity. The velocity levels are lower due to the larger passage area. The reduction of the friction losses due to the lower velocity is counterbalanced by the increase in blade length. The improvement of the performance is greater for impellers with lower flow coefficient.

# 3.3.4. Velocity Ratio

The maximum deceleration is an important parameter that can be correlated to boundary layer separation. The limiting value for  $W_2/W_{1min}$  varies between the authors but generally ranges between 0.5 and 0.7.

# 3.3.5. Slip Factor

The slip factor is estimated from empirical correlation or theoretical calculation. The main correlations have been developed as a function of blade number and exit blade angle. The slip factor is a function of many more parameters and should be considered as a one-dimensional approach.

The slip factor depends on the mass flow rate. Eckardt (1980) showed for his radial discharge impeller that the slip factor increased for decreasing mass flow rate. For his backward impeller, an opposite trend was found. Figure 3.18 shows the measured slip factor by Paroubek et al. The slip factor is almost constant around 0.81-0.82 for the

narrow stages. For the wider stages (D, E, F) the slip factor increases for decreasing mass flow rate similarly to the radial discharge impeller of Eckardt.

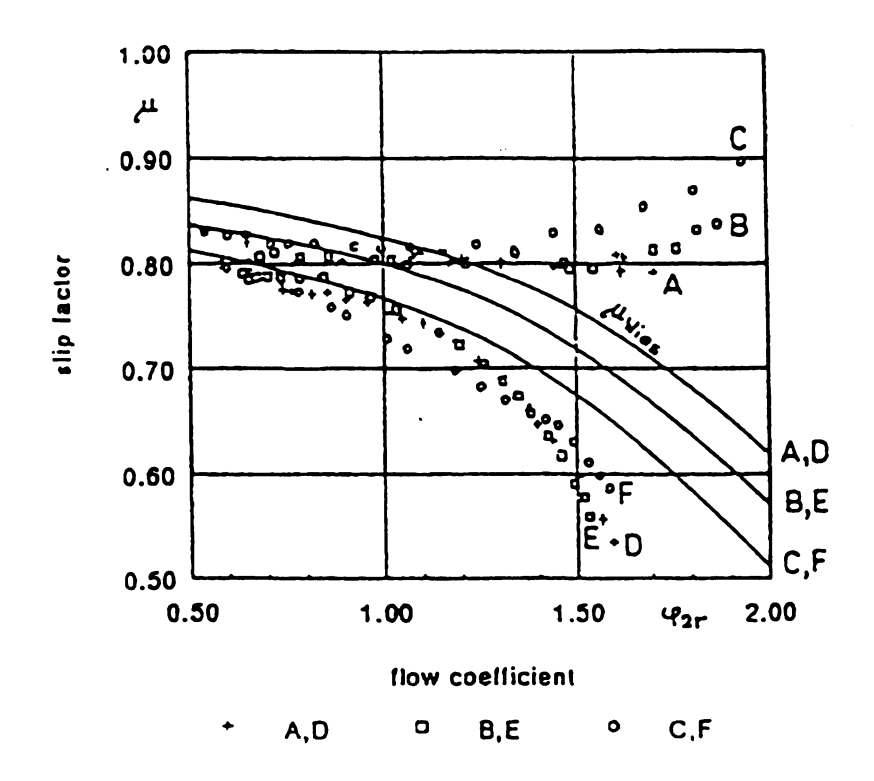


Figure 3.18 Slip factors (Paroubek et al. 1994)

It does not seem possible to establish any design rule for the choice of the slip factor. Nevertheless, the low slip factor values (around 0.8) obtained by Paroubek on his highly backward-swept impeller should be kept in mind.

# 4. ONE-D COMPRESSOR MODELING AND DESIGN PARAMETERS

A one-dimensional method and a streamline curvature throughflow method have been used to design the impellers. Both methods have been adapted from the open literature and are described in detail in Appendices B and C. This chapter presents a parametric study to obtain the geometry of five impellers satisfying the design constraints. Each impeller must perform the same duty but has a different outlet angle-outlet width combination. The one-dimensional analysis and the determination of the geometry are presented hereafter. The CFD results will be discussed in Chapter 6.

#### 4.1. Description of the 1-D Method

Various methods exist to design a centrifugal impeller. A dimensionless approach based on the established relations between specific speed, specific diameter and efficiency like the approach of Balje (1980) can be used for the preliminary sizing of the impeller. Other types of approach are the ones described by Galvas (1973) or Aungier (1995). These methods rely on the equations of fluid dynamics onto which loss models are added to describe each type of loss (incidence, friction, etc.). A third approach

proposed by Dean (1974) tries to reduce the number of correlations by introducing a diffusion level parameter to characterize the performance of the impeller.

All of these methods require the introduction of the some empirical correlations. They may therefore be more adapted to one type of impeller or another, depending on the origin of the experimental data. The two-zone model was chosen hereafter because some analysis had already been done with this model on the existing stages of the impeller family.

#### 4.1.1. Two-zone Model

The two-zone model (Japikse 1985) is an evolution of the jet-wake model proposed by Dean and Senoo (1960) and Dean (1974), and schematically shown in Figure 3.1. Japikse, after reviewing the basic assumptions and the derivation of the equations governing the jet and the wake, used the term two-zone model to personalize his approach. The author assumes that:

- (1) an isentropic core zone and a non isentropic secondary zone coexist,
- (2) the diffusion of the core flow and development of the second zone is similar to other diffuser problems
- (3) the tip static pressure may be assumed the same for each zone or corrected by a small factor,
- (4) the deviation of the second zone has a small effect on modeling; deviation of the primary zone is critical in setting overall slip,
- (5) a mixed-out state can be computed at the impeller exit for thermodynamic state evaluation and for determining average conditions.

Assumption (1) is fundamental. It is based on earlier experimental observations showing that these two regions co-exist. The jet being isentropic, all the losses can only originate in the wake. Experimental works (e.g. Rothe and Jonston 1976) in rotating diffusers have shown similarities with the flow in centrifugal impellers and have led to assumption (2). Assumption (3) is based on the condition that the pressure side and the suction side velocities must be equal at impeller exit (the Kutta condition). The experimental observations at the impeller exit showed the larger extent of the primary zone and justified assumption (4). Assumption (5) allows one to compute a mixed-out state at the impeller tip, even if in reality the mixing between the two zones will be accomplished further downstream.

The equations governing the two zones and the mixed-out conditions are presented in Appendix B. The two-zone model has been used to represent the flow in the low-flow coefficient compressors presented in this study. Its validity will be shown in Chapter 6.

#### 4.1.2. Impeller Diffusion Level

The diffusion of the relative flow that can be achieved without separation is limited. Among all the parameters that can be used to describe this limit, the impeller Mach number ratio MR<sub>2</sub> introduced by Dean (1974) is used. It is defined by

$$MR_2 = \frac{M_{W1r}}{M_{W2 \, \text{primary zone}}}$$

i.e. as the ratio of the relative Mach number at inducer tip over the relative Mach number of the primary zone (jet) at impeller exit.

An ideal Mach number ratio, which intends to account for the geometry of the impeller channel is defined by

$$MR_{2i} = \frac{M_{W1t}}{M_{W2 \, \text{primary zone, ideal}}}$$

i.e. the ratio of the relative Mach number at the inducer tip over the relative Mach number of the primary zone at the impeller exit in an ideal state assuming no blockage, no friction, and no deviation.

As stated by Dean, "MR<sub>2</sub> indicates the actual Mach number reduction the impeller achieves in its cover (or shroud) stream tube (which is the critical one)." MR<sub>2</sub> and MR<sub>2i</sub> have been correlated to obtain a state-of-the-art curve. A first general correlation between MR2 and MR2i was proposed by Benvenutti (1978) for three-dimensional impellers and for industrial two-dimensional impellers (Figure 4.1).

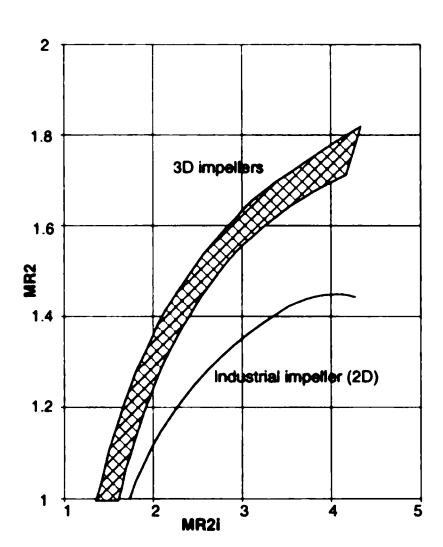


Figure 4.1 Comparison of achievable primary flow diffusion in industrial 2D impellers and in straight inlet, 3D impellers (Benvenutti 1978)

At a preliminary stage, MR<sub>2</sub> can be set to the value corresponding to the state-of-the-art. A more recent correlation proposed by Japikse (1996) was used hereafter. It will be referred to it as the "state-of-the-art" or SOA.

#### 4.1.3. Off-Design Performance

The TEIS model (Two-Elements-In-Series) was introduced by Japikse (1984) to describe the performance of an impeller and predict the overall map of a machine. In this model, the impeller is viewed as two diffusers in series: the first one extends from the inlet to the throat and acts as a diffuser or a nozzle depending on the flow conditions; the second one, from the throat to exit, is the impeller passage (Figure 4.2).

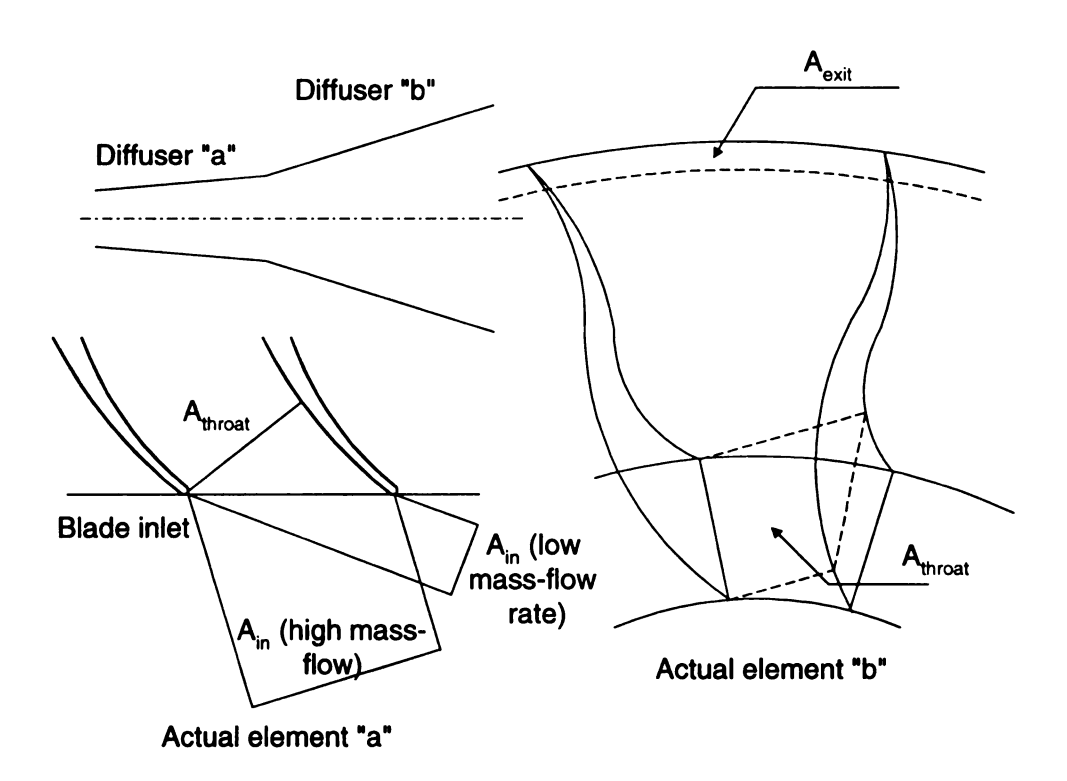


Figure 4.2 TEIS model – Diffusing passages (after Japikse 1984)

An effectiveness is used to characterize the diffusing ability of each passage. It is the ratio of actual pressure recovery to the ideal pressure recovery obtained for an inviscid flow.

The parameter  $\eta_a$  represents the effectiveness of the impeller inlet portion, which can be considered as a diffuser or a nozzle depending on the incidence. In the following equation, Cp is the pressure recovery between the inlet and the throat, and AR is the ratio of the throat area to the inlet area. Cp<sub>a</sub> is the actual pressure recovery taking place between inlet and exit. Cp<sub>a,i</sub> the ideal pressure recovery that would take place based only on the geometrical area ratio.

$$\eta_a = \frac{Cp_a}{Cp_{a,i}}$$
 where  $Cp_{a,i} = 1 - \frac{1}{AR_a^2} = 1 - \left(\frac{\cos \beta_1}{\cos \beta_{1b}}\right)^2$ 

At high mass flow, the area ratio  $AR_a = A_{th}/A_{in}$  is larger than 1, and  $Cp_{a,i}$  is negative. At low mass flow rate,  $AR_a$  is lower than 1, and  $Cp_{a,i}$  is positive. Therefore an increase of  $\eta_a$  makes  $Cp_a$  more negative at high mass flow rate and reduces the diffusion, whereas it has an opposite effect at low mass flow rate where  $Cp_a$  is made more positive.

 $\eta_b$  represents the effectiveness of the passage portion.  $Cp_b$  represents the pressure recovery between the throat and the exit.

$$\eta_b = \frac{Cp_b}{Cp_{b,i}}$$
 where  $Cp_{b,i} = 1 - \frac{1}{AR_b^2} = 1 - \left(\frac{A_{th}}{A_e}\right)^2$ 

 $Cp_{b,i}$  is only function of the geometry and not of the flow condition. Therefore,  $\eta_b$  will affect the impeller diffusion over the whole operating range.

From  $\eta_a$  and  $\eta_b$ , the diffusion ratio DR=W<sub>1t</sub>/W<sub>2p</sub> can be calculated (Appendix B), and all the subsequent aero-thermodynamics variables.

A maximum diffusio ratio  $DR_{max}$  (or  $DR_{stall}$ ) is used to limit by a reasonable physical value, the maximum diffusion achieved at low mass-flow rates in the impeller. It sets the diffusion to a constant value for mass flow rate below the limiting point.

Once the values of these three parameters have been determined, the performance of the impeller at various rotational speeds and various mass flow rates can be predicted.

## 4.2. One-Dimensional Analysis

A one-dimensional Fortran code has been developed to solve the equations describing the two-zone model of Japikse (1985) for the case of a perfect gas. The flow in the vaneless diffuser is calculated following the approach of Johnston and Dean (1966).

In this chapter, the code has been applied to design five impellers with different outlet blade angles and outlet widths fulfilling the design requirement. All the designed impellers have the same inlet flow coefficient. The objective was to investigate the effect of the exit blade angle on the impeller flow field and on the impeller performance.

#### **4.2.1. Design Constraints**

The exit conditions of an existing stage provide the inlet conditions (total temperature and total pressure) of the stage to be designed. The impellers must pass the required mass flow at the design rotational speed and provide an increase of head between 7,000 and 8,000 ft-lbf/lbm, which corresponds to a pressure ratio around 1.18 at specified inlet conditions. Geometrically, the hub diameter, exit diameter, and impeller axial length are fixed.

#### 4.2.2. Modeling Assumptions

When solving the system of equations for the two-zone model and mixed-out conditions, a few parameters have to be assumed in order to equate the number of unknowns with number of equations:

- (1) The slip factor is set by the Wiesner correlation. As it was observed that these values were generally high, a value 0.03 lower than the correlation was used.
- (2) The impeller Mach number ratio was set by the state-of-the-art curve.
- (3) The ratio  $\chi$  of the mass contained in the secondary zone to the total mass flow was set to 0.15, which is in the range of the recommended values.
- (4) The inlet blockage and inlet distortion were first guessed, and then reevaluated with the help of CFD (Appendix E). A blockage of 5% and a hub-to-shroud distortion of 1.3 were used.

This ensures the closure of the system of equations and allows the calculation of all the thermodynamic conditions at inlet and outlet. The validity of assumption (2) and (3) is studied in the next section.

## 4.2.3. Influence of the Modeling Assumptions on the Choice of the Geometry

The influence of the secondary flow mass fraction  $\chi = \frac{\dot{m}_{sec}}{\dot{m}}$  and of the Mach number ratio MR<sub>2</sub> on the performance prediction has been investigated.

The two-zone model recommends using a value of  $\chi$  between 0.02 and 0.30. Considering the AA impeller configuration, whose geometry will be given in Chapter 5,

the value of  $\chi$  has been varied between these two extremes for various values of  $MR_2$  but at a constant slip factor. As the geometry is fixed,  $MR_2$  sets the diffusion into the primary zone.

Figure 4.3 shows the effect of  $\chi$  and MR2 on the area ratio  $\epsilon$  between the secondary zone and the outlet area. At low values of MR2, the wake area is nearly independent of the secondary zone mass fraction. For a fixed value of MR2, greater than 1.0, diffusion occurs into the jet; and as expected, the wake area increases as the assumed mass flow into the wake increases (increasing values of  $\chi$ ). For a given  $\chi$ , the velocity in the wake increases as MR2 increases; and because the mass flow in the wake is constant, the area of the wake must reduced. It will be seen in Figure 4.5 that the range of values covered by  $\chi$  and MR2 is limited. In particular, the lower left end of the curves MR2=1.2 and MR2=SOA corresponds to 0 aerodynamic blockage and should not be considered.

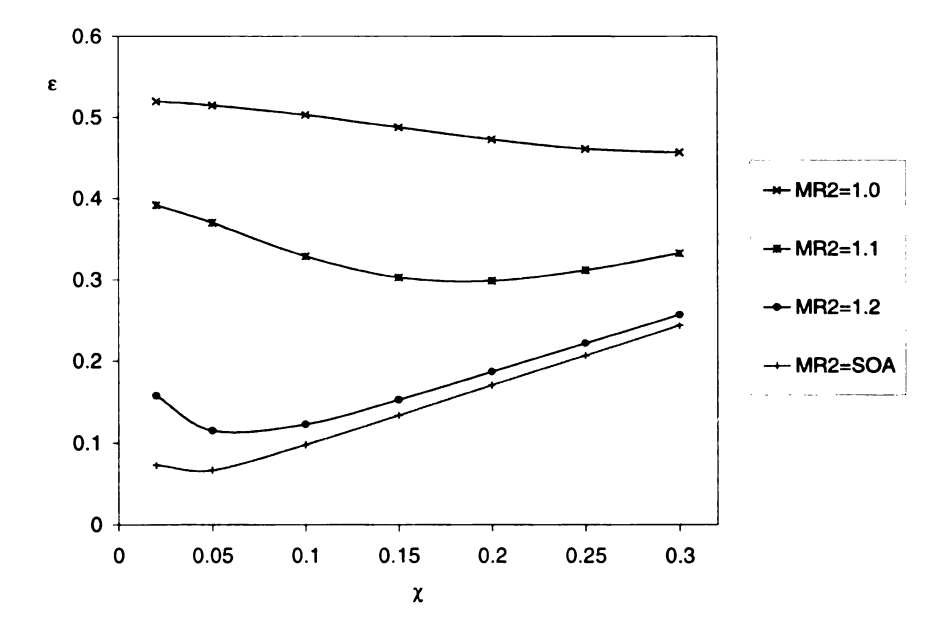


Figure 4.3 Effect of  $\chi$  and MR2 on the wake width

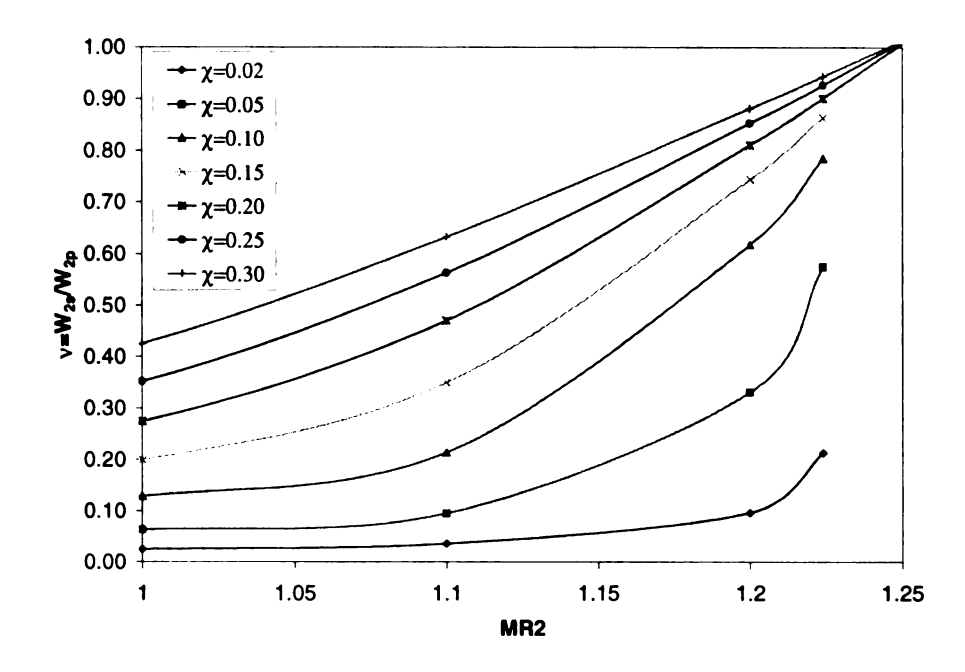


Figure 4.4 Effect of  $\chi$  and MR2 on  $v=W_{2s}/W_{2p}$ 

Figure 4.4 shows how MR2 and  $\chi$  influence the velocity ratio between the jet and the wake. For small values of  $\chi$ , the velocity of the wake remains small and does not exceed 20% of the jet velocity.  $\chi$  has a large influence on v for MR2 larger than 1.0. As more diffusion occurs in the jet, the velocities between the two zones get closer, especially for large values of  $\chi$ . Values of MR2 greater than 1.2 should not be considered as is explained below.

Figure 4.5 shows the effect of MR2 and  $\chi$  on C=W<sub>2m</sub>/W<sub>2p</sub> and on the deviation into the primary zone. C is an indication of the amount of aerodynamic blockage at impeller exit. C varies linearly with MR2 because the velocity in the primary zone is directly proportional to MR2 and independent of  $\chi$ . The mixed-out velocity W<sub>2m</sub> is only slightly influenced by  $\chi$ . As the diffusion of the primary zone increases, the relative velocity in the wake increases, affecting in turn the deviation in the primary zone. It is

assumed that the secondary zone follows the blade. The deviation of the mixed-out conditions is fixed by the slip factor. Therefore, the deviation of the primary zone is adjusted to satisfy the continuity equation. In reality, the primary zone will contain most of the mass flow and will deviate from the blade by a few degrees, reducing the work input. Hence, all values of  $\delta_{2p}$  above  $-5^{\circ}$  should be excluded. The lower horizontal line in the figure indicates the values of  $\chi$  and MR2 corresponding to a deviation of the primary zone by 5°: this corresponds to values of MR2 greater than 1 for  $\chi$ =0.3, and greater than 1.15 for  $\chi$ =0.02. Also, the velocity ratio between the secondary and the primary velocity should remain lower than 1.0 to satisfy the initial assumption of a high speed zone (jet) and a low-momentum zone (wake). Otherwise, most of the mass flow would be passing into the wake, and there would be hardly any jet left anymore. Furthermore, at the exit of the impeller there should be a minimum of 10% of aerodynamic blockage (Pampreen 1981). Only values of C smaller than 0.9 should therefore be considered. The upper horizontal line in the figure indicates the values of  $\chi$  and MR2 corresponding to a blockage of 10%. An upper limit for MR2 can then be set around 1.13 (with the value of the assumed slip factor). This maximum value is the same for all the range of values covered by  $\chi$  because C is independent of MR2.

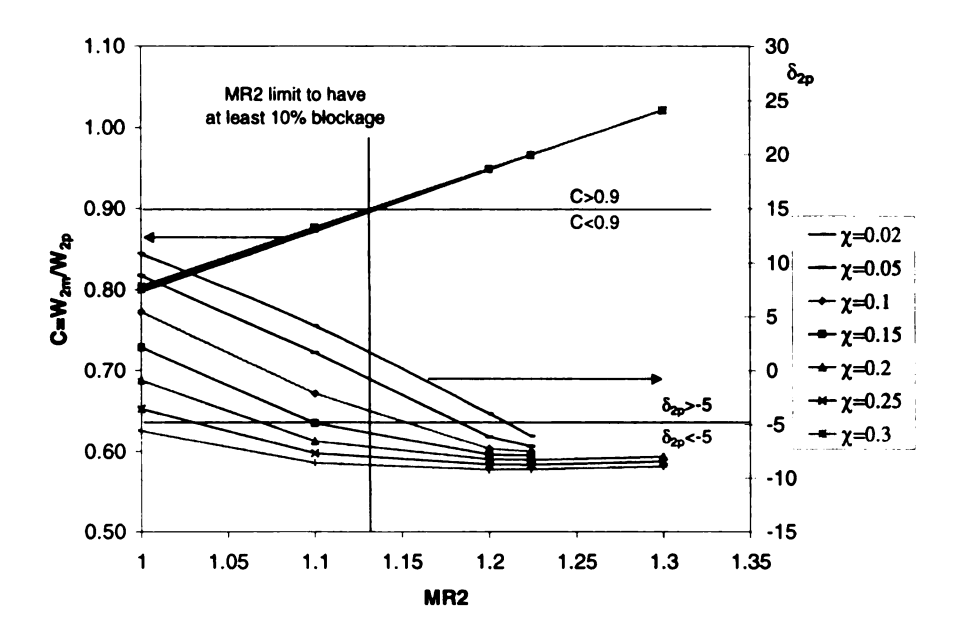


Figure 4.5 Effect of  $\chi$  and MR2 on C=W2m/W2p and on  $\delta_{2p}$ 

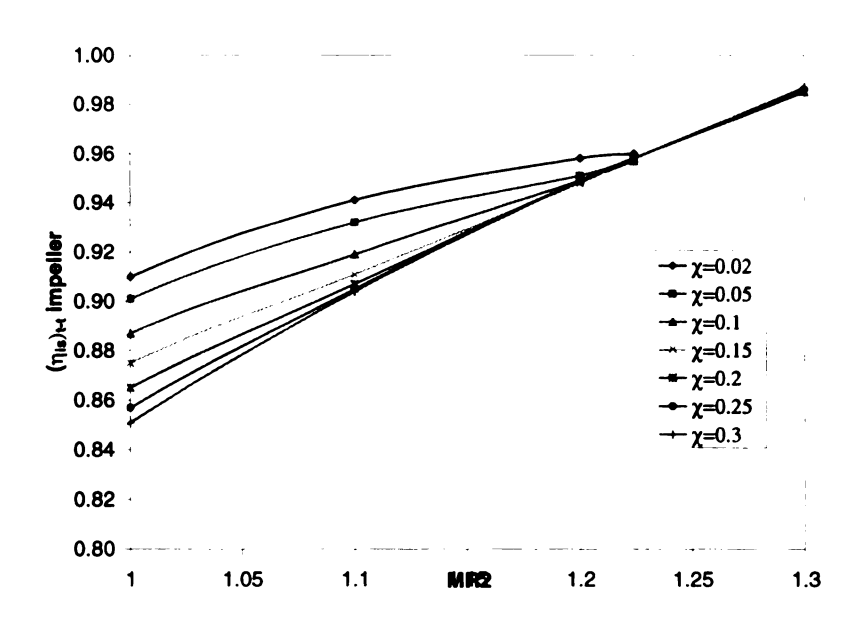


Figure 4.6 Effect of  $\boldsymbol{\chi}$  and MR2 on the impeller efficiency

Figure 4.6 shows the effect of MR2 and  $\chi$  on the impeller efficiency. As MR2 increases, the relative area of the wake decreases. Because all the losses are generated into the wake and into the mixing process between the jet and the wake, the impeller efficiency approaches 1.0. Consequently, the pressure ratio in the impeller increases with MR2 as shown in Figure 4.7. The effect of  $\chi$  is small in the useful range of MR2 (for a constant slip factor). The cases corresponding to MR2 values greater than 1.2 are unrealistic for the given geometry as they lead to very small aerodynamic blockage.

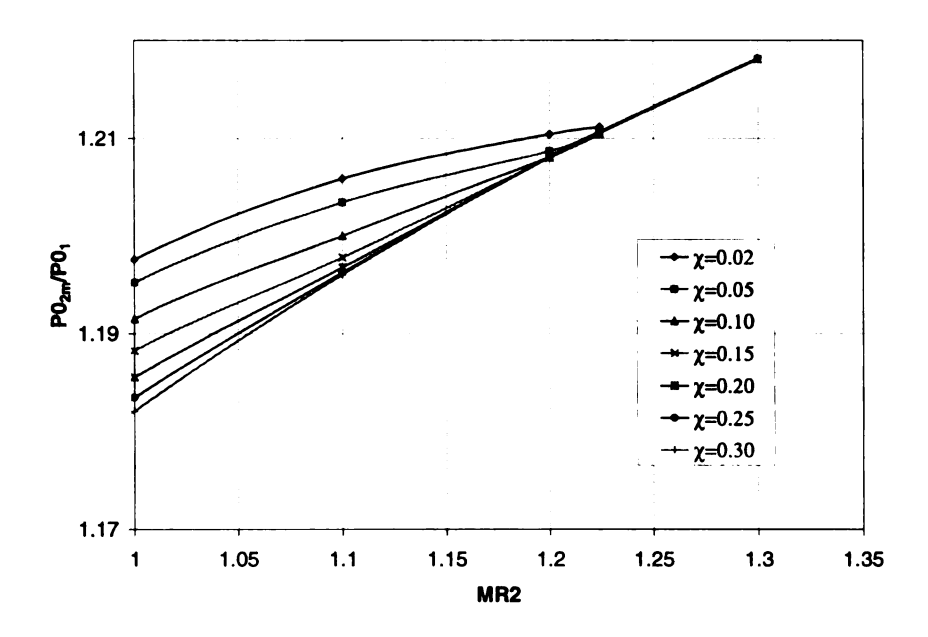


Figure 4.7 Effect of  $\chi$  and MR2 on the impeller pressure ratio

These systematic calculations have shown that MR2 should be chosen between 1 and 1.15 for the chosen slip factor. The  $\chi$  ratio should be kept between 15 and 25%. When calculating with a constant slip factor, the deviation of the primary zone should lie in the expected range of -5 to -10°. The implication of these results on the choice of the TEIS model will be discussed in Chapter 6.

## 4.2.4. 1-D Impeller Design

#### **4.2.4.1.** Inducer

The objective of the inducer is to guide the flow from axial to radial, increasing its angular momentum. A designer will draw particular attention towards:

- minimizing the inlet relative Mach number (keep it subsonic)
- choosing the inlet blade angle in order to get a slightly positive incidence at design point (Rodgers, 1964)
- checking the throat area to ensure the passage of the required mass flow rate at design

Figure 4.8 shows the calculated inlet tip relative Mach number Mw1t for various inducer tip-to-hub diameter ratios. For a small value of the inducer tip radius, the axial component of velocity is large and the tip peripheral speed is low. As the tip radius is increased, the area increases, hence reducing the axial velocity but increasing the inducer tip peripheral speed. Therefore an optimum radius ratio always exists, where both effects compensate and for which Mw1t is minimum.

Once the velocity triangles are obtained at hub, mean, and shroud, the blade angle can be set to obtained the desired incidence which was chosen to be slightly positive at hub, mean, and shroud.

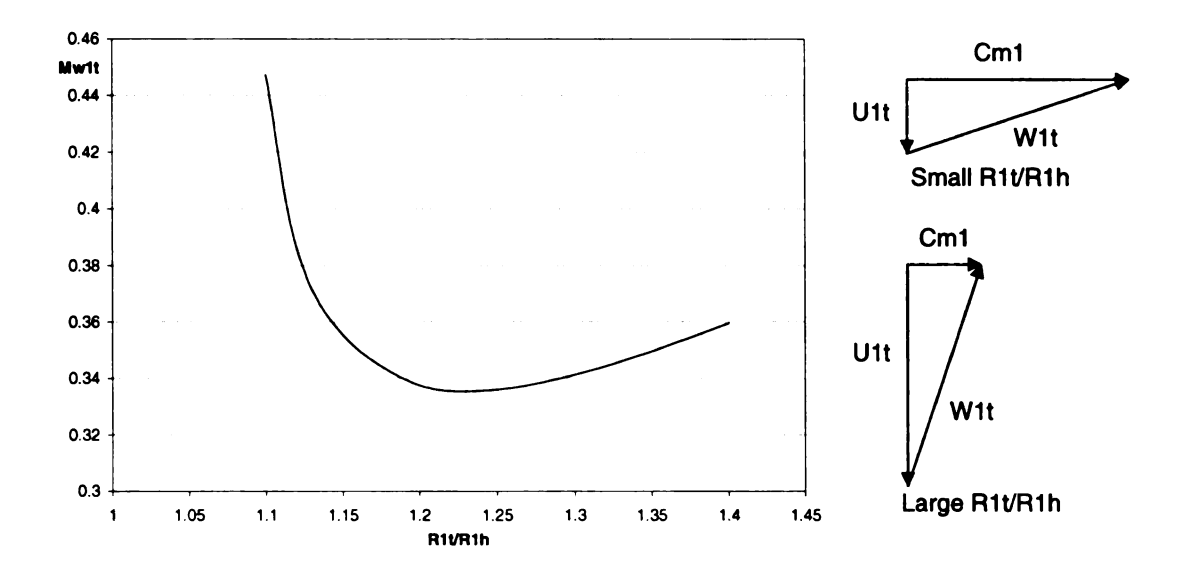


Figure 4.8 Influence of the hub-to-shroud inlet radius ratio on the shroud inlet relative Mach number

## 4.2.4.2. Impeller Exit Width and Exit Blade Angle

The determination of the optimum impeller exit width and exit blade angle is much more difficult as it involves many more parameters. The following calculations have been made for a constant slip factor assumed to be three points lower than the slip factor of Wiesner's correlation. The exit tip radius is fixed. The mass flow in the secondary zone is kept constant at 15% of the total mass-flow. The Mach number ratio is set to the value of the state-of-the-art. By doing so, there is a minimum value of b<sub>2</sub> that can be used, below which the area of the secondary zone becomes smaller than 10% of the exit area and falls out of the assumptions of the model. The width of the diffuser is set at 75% of the impeller exit width to ensure a larger inlet flow angle at the diffuser entrance. Figure 4.9 shows the predicted stage total-to-total pressure ratio at the design point for the 54 cases run.

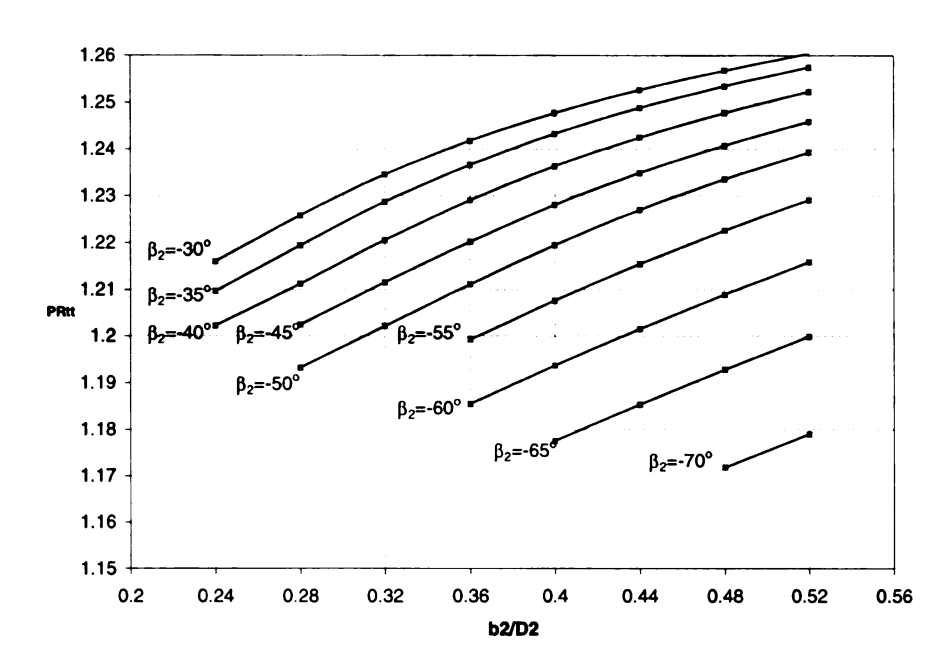


Figure 4.9 Stage total-to-total pressure ratio as a function of impeller exit width and impeller exit blade angle

Figure 4.10 shows the exit tangential velocity, which expresses directly the work done by the impeller.

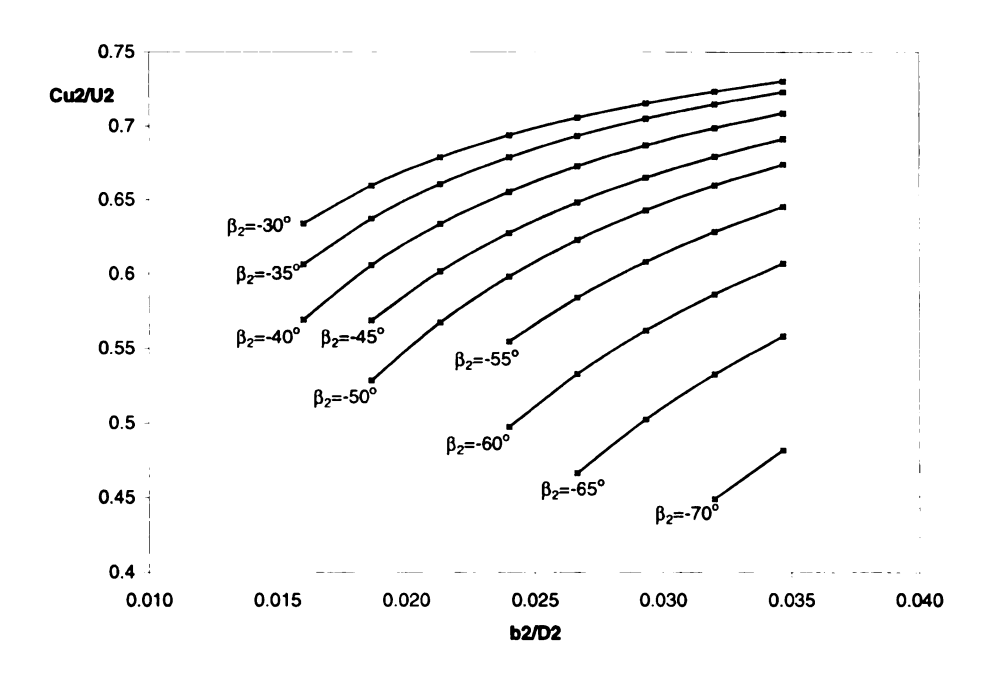


Figure 4.10 Impeller exit tangential velocity versus impeller width

A line of constant Cu2/U2 corresponds to a line of constant work input. The choice of the geometry was based on the stage pressure ratio rather than the impeller work input in order to include the diffuser in the design process.

The relative velocity ratio  $W_2/W_{1tip}$  is shown in Figure 4.11. It characterizes the relative diffusion on the shroud streamtube. It remains higher than 0.6 for most cases. When the velocity ratio becomes smaller than 0.6, boundary layer separation can be expected and higher losses will occur.

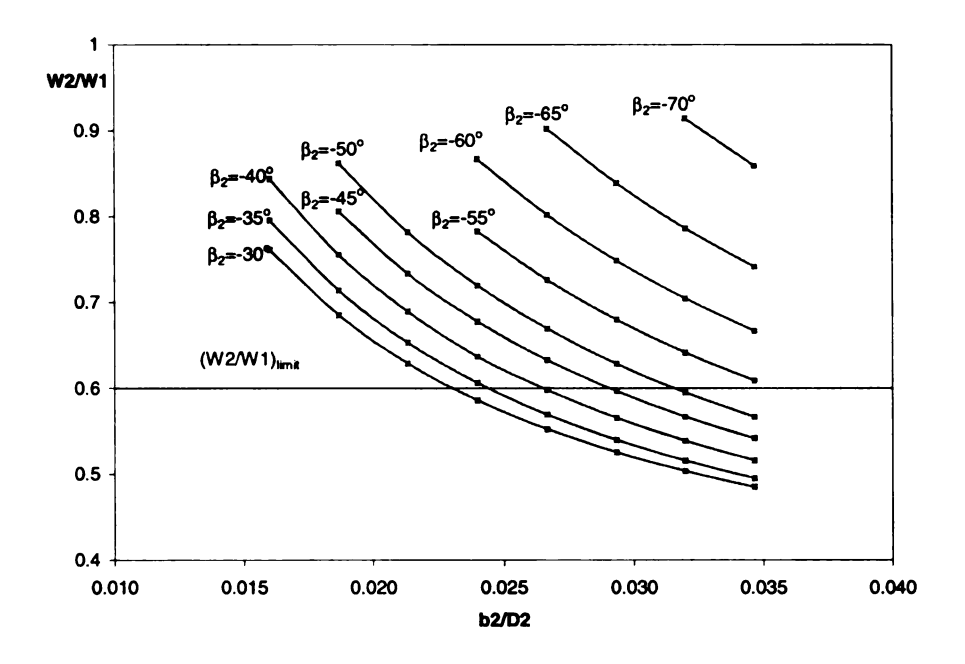


Figure 4.11 Relative velocity ratio as a function of impeller exit width and impeller exit blade angle

Figure 4.12 shows the absolute flow angle at impeller exit  $\alpha_{2m}$ . The exit impeller flow angle should not be too tangential to avoid high losses and to maintain an acceptable range in the vaneless diffuser. The curve representing  $\alpha_{critical}$  vs.  $b_2/D_2$  is adapted from Senoo (1978). If the flow angle at the diffuser entrance is higher than the critical flow

angle, rotating stall inside the diffuser should be expected. At the design point, the flow at the impeller exit should be at least 10° smaller than the critical flow angle to ensure an acceptable operating range.

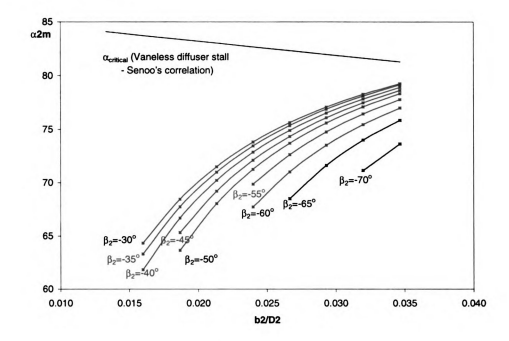


Figure 4.12 Impeller exit absolute flow angle vs. impeller exit width and impeller exit blade angle

The performance prediction for the vaneless diffuser must be taken into account when sizing the impeller. Indeed, the best compressor performance can only be achieved if the impeller and the diffuser reach their maximum performance at the same mass-flow rate. Figure 4.13 and Figure 4.14 show the pressure recovery and the total pressure loss coefficient between diffuser inlet and diffuser exit. The method used to calculate the flow in the vaneless diffuser is presented in Appendix B. The friction coefficient is determined as a function of the diffuser inlet Reynolds number. It increases as the diffuser becomes narrower and as the inlet velocity decreases. Hence, as the diffuser width is reduced, the pressure recovery decreases and the loss coefficient increases. One would therefore believe that the widest diffuser should be used to maximize pressure recovery and

minimize the total pressure loss. It should be kept in mind that the flow in a wider diffuser will be more tangential, and therefore more likely to become unstable. Furthermore, lower inlet flow angles lead to longer flow path and higher friction losses.

The pressure recovery predicted by this method is generally optimistic. A slightly lower value should be expected in the actual machine.

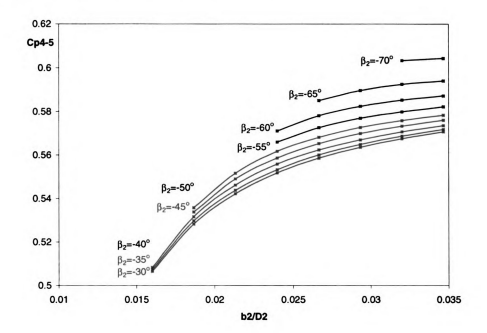


Figure 4.13 Diffuser pressure recovery as a function of impeller exit width and exit blade angle

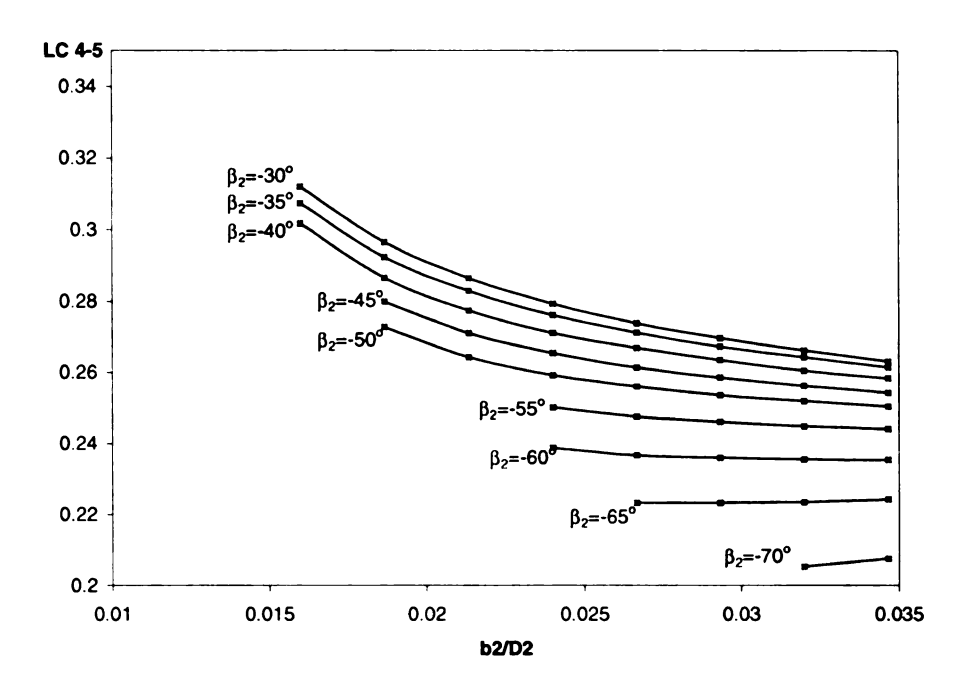


Figure 4.14 Diffuser total pressure loss coefficient as a function of impeller exit width and exit blade angle

Based on this analysis, the geometry of five candidate impellers able to provide a total-to-total pressure ratio around 1.19 was selected. The exit blade angles were chosen between -50 and -70° because of the relatively low pressure ratio that needs to be achieved. An impeller with a more radial outlet blade angle will require a too narrow outlet width. The corresponding geometry (obtained from Figure 4.9) and some of the performance parameters are given in Table 4.1. The head coefficient, the efficiency, and the pressure ratio (PR) are given for the stage (impeller and diffuser) and are based on total-to-total conditions. The denomination used is AA, followed by the value of the outlet blade angle. The AA70 has a smaller work input than the four other impellers, but the expected total-to-total pressure ratio is close to 1.19 due to the reduced losses in the diffuser.

**Table 4.1 Geometry of the five selected impellers** 

					-
	AA50	AA55	AA60	AA65	<b>AA</b> 70
b2	0.30	0.34	0.40	0.49	0.58
β2	-50	-55	-60	-65	-70
σ	0.84	0.845	0.85	0.86	0.87
$C_{u2m}/U_2$	0.549	0.537	0.533	0.539	0.522
$W_{2m}/W_{1t}$	0.82	0.82	0.80	0.77	0.79
$\alpha_2$	66.0	68.2	71.0	74.5	76.4
$\beta_2$	-61.6	-65.0	-68.6	-72.0	-75.2
CP <sub>45</sub>	0.55	0.56	0.58	0.59	0.61
LC <sub>45</sub>	0.27	0.25	0.24	0.22	0.21
$(\eta_{is})_{tt}$	0.825	0.835	0.838	0.83	0.841
Πιι	1.198	1.195	1.194	1.195	1.189

This performance prediction at design point will be revised in Chapter 6 based on the CFD results.

## 4.3. Streamline Curvature Throughflow Method

As seen in Chapter 3, an inviscid analysis is generally not able to predict accurately the flow in a centrifugal impeller especially near the impeller exit. Nevertheless, it is useful to establish the initial geometry based on such a method. Many aerodynamic criteria have been developed for inviscid flow that allows the designer to adjust the meridional contour and the blade angle distribution. A streamline curvature code has been developed to analyze the impeller. The method requires the introduction of relaxation factors to ensure numerical stability.

#### 4.3.1. Description of the Quasi-3D Method

A streamline curvature method is an iterative procedure for obtaining a solution of the flow field starting from an initial guess of the streamsurface shape. It assumes an axisymmetric flow. As mentioned by Denton (1978), this may be regarded as being obtained by circumferentially averaging all flow properties or by solving for the flow on a mean blade-to-blade streamsurface whose thickness and inclinations are determined by the geometry of the blade rows. The method is described in details in Appendix C.

#### 4.3.2. Definition of the Blade Geometry

The impeller geometry is defined by the shape of the meridional contour at the hub and at the shroud. Bezier polynomium have been used to describe the contours. Details on this procedure can be found in Appendix C.

When designing any impeller, the blade angle distribution at the hub and the shroud is prescribed as a function of the relative distance along the meridional contour. The local circumferential position  $\theta$  at hub and shroud is then calculated by

$$\theta = \int \frac{\tan \beta}{r} dm$$

where r is the radius along the meridional contour.

The  $\theta$  distribution (also called wrap angle distribution) can be adjust at the hub and at the shroud by adding any constant at inlet, leading to

$$\theta_{hub} = (\theta_{hub})_{entry} + \int \frac{\tan \beta_{hub}}{r} dm \text{ and } \theta_{shroud} = (\theta_{shroud})_{entry} + \int \frac{\tan \beta_{shroud}}{r} dm$$

The  $\theta$  distribution then determines the lean angle distribution  $\gamma$ , which characterizes the inclination of the blade (i.e. how tilted the blade is with respect to the radial direction). Mathematically,  $\gamma$  is expressed by

$$\tan \gamma = r \frac{\partial \theta}{\partial b}$$

where b is the distance along a quasi-orthogonal. The convention adopted herein for the sign of the lean angle assumes that the blade leans forward in the direction of rotation for positive lean.

Letting  $(\theta_{shroud})_{entry}=0$ , and  $(\theta_{hub})_{entry}=(\theta_{ref})$ , the lean angle at inlet is shown in Figure 4.15.

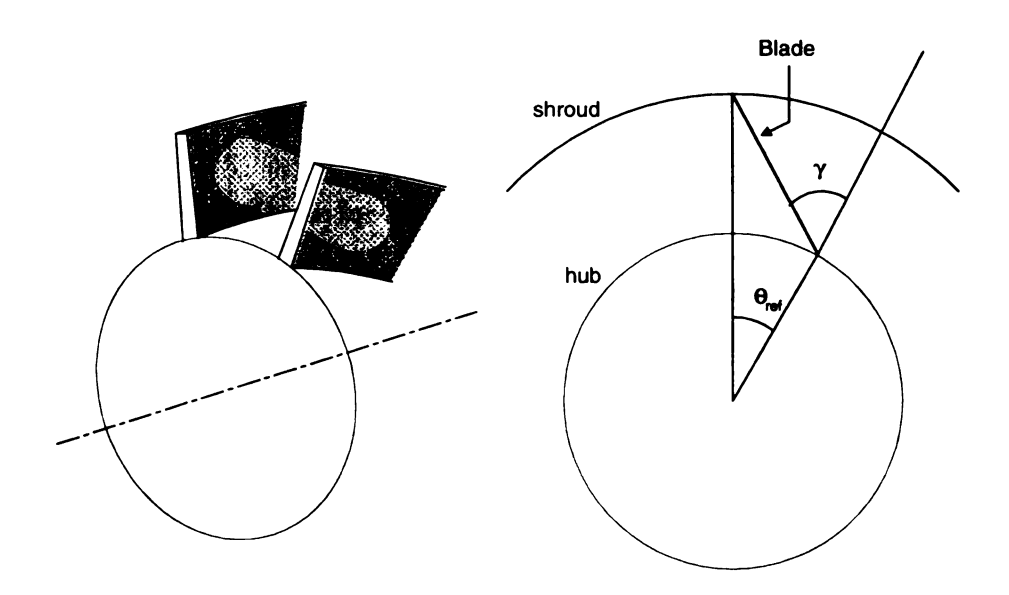


Figure 4.15 Definition of the lean angle

The lean angle at the impeller exit is called the rake angle  $\tau$  (Figure 4.16). High values of the rake angle are undesirable in narrow impellers because they will induce more aerodynamic blockage. The entry value of the wrap angle and the blade angle must

therefore be adjusted to obtain a low lean angle. The validity of the lean angle distribution will be determined in the end by stress analysis.

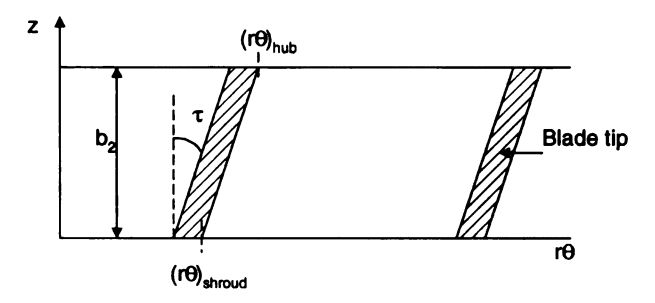


Figure 4.16 View of the impeller tip and definition of the rake angle

The blade thickness distribution normal to the blade is prescribed as a function of the relative distance along the meridional contour. Using the local blade angle, the wrap angle on the pressure side and on the suction side of the blade can be evaluated.

#### **4.3.3.** Impeller Blade Shape for the Five Impellers

To adjust the blade contour of the impeller and the blade angle distribution, a commercial software available at Solar Turbines Inc. was used. The resulting geometry is compromise between the blade loading distribution, the lean angle distribution, the and smoothness of the curvature distribution.

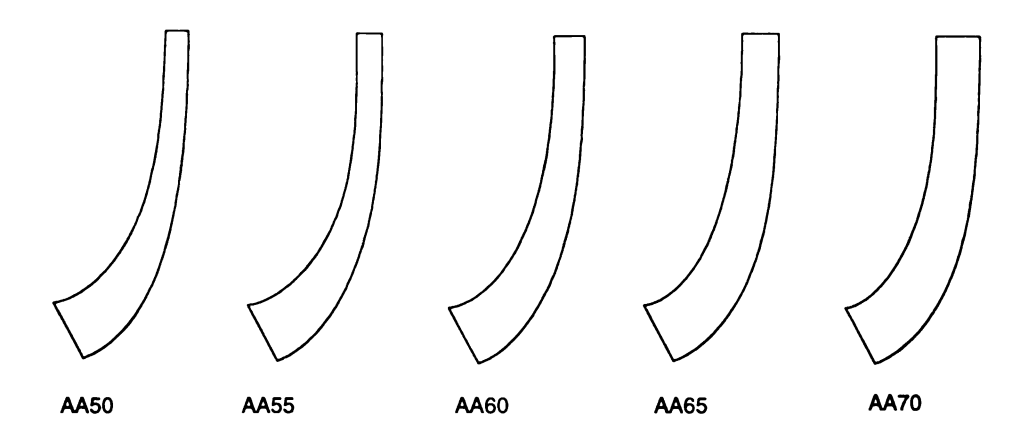


Figure 4.17 Impellers meridional contour

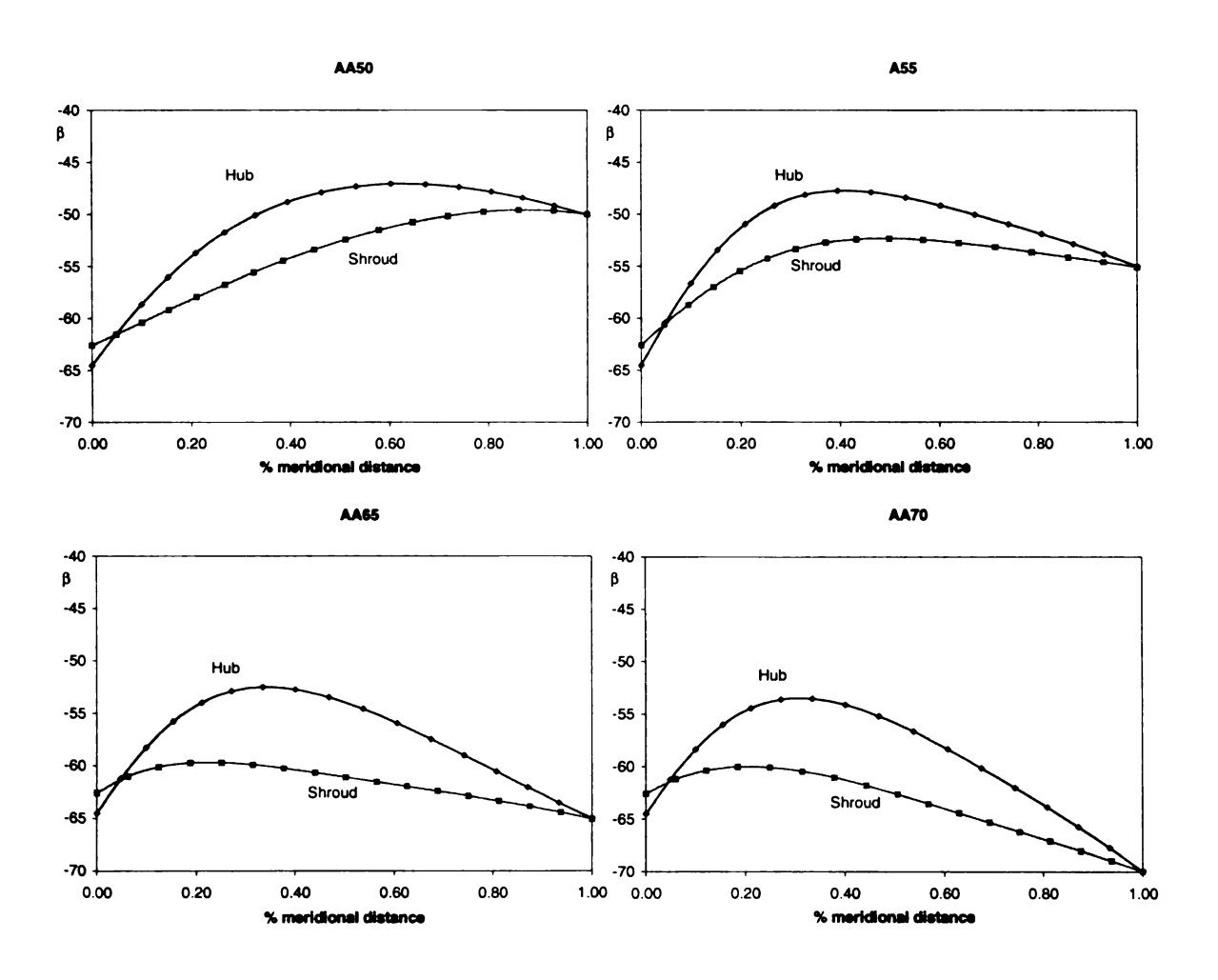


Figure 4.18 Blade angle distribution for the AA50, AA55, AA65, and AA70

## 4.3.4. Velocity Distribution and Blade Loading for the Five Impellers

The blade angle distributions, the meridional contours, and the hub wrap angle at entry were adjusted to satisfy acceptable velocity distributions, blade loading, and lean angle distribution. The momentum at the exit of the blade was prescribed, based on the assumed slip factor. The following blade-to-blade loadings were obtained. The maximum loading was located between 50 and 70% of the meridional length, and its maximum value was kept below 0.7. Thirteen blades were used.

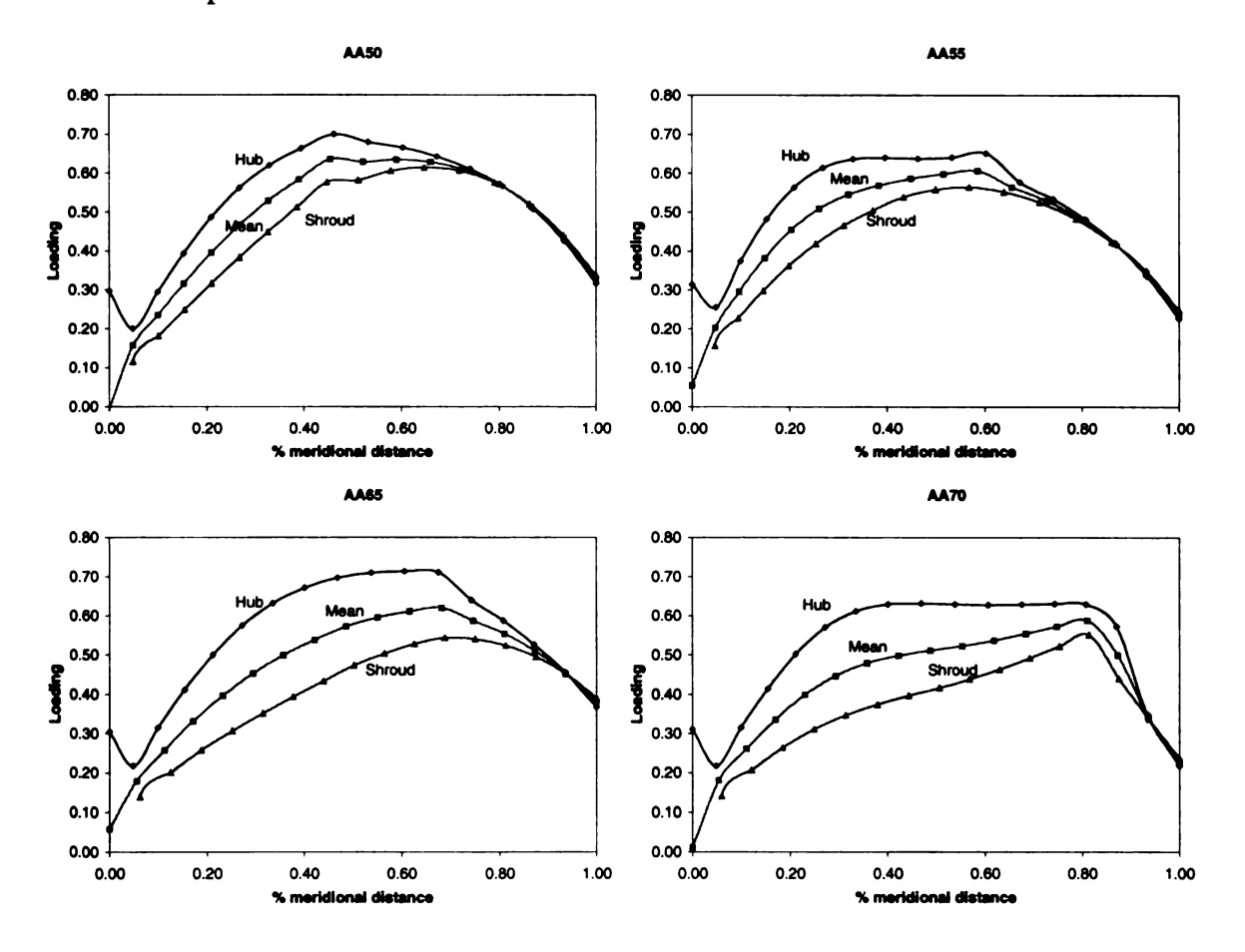


Figure 4.19 Blade-to-blade loading for the impellers

These impellers have been analyzed with CFD and will be reviewed in Chapter 6.

# 5. DESIGN AND ANALYSIS OF FOUR LOW-FLOW COEFFICIENT COMPRESSORS

This Chapter presents the one-dimensional, the streamline curvature, and the CFD analysis of four stages that have been designed as an extension of an existing family of impellers. The flow is analyzed qualitatively at design and at off-design conditions. The flow between the four impellers is compared to determine the effect of the blade passage width.

## 5.1. Design Requirements

## **5.1.1. Inlet Design Conditions**

In a multi-stage compressor, the exit conditions of one stage provide the inlet conditions of the next stage. All the impellers have the same rotational speed and the mass-flow rate passing through the machine is the same for all stages.

The existing family of impellers consists of ten shrouded. The four new stages that will be added will be denoted AA, AB, AC and AD. The AA impeller has the largest flow coefficient, followed by AB, AC, and AD.

The existing family of impellers has been designed for a made-up gas corresponding to the one used in the field of application of the machine. The specific

gravity, the pseudo-critical pressure and temperature of the gas are given. The specific heat, the viscosity and the compressibility can be determined as a function of pressure and temperature.

The inlet conditions of the AA impeller are set to the reference conditions, which are an inlet total pressure of 750 Psia (52 bars) and 580°R (322 K). An equivalent mass-flow rate and equivalent rotational speed have been calculated, which conserve the volume flow rate corresponding to the exit conditions of an A1 stage.

## **5.1.2.** Impeller Sizing

## **5.1.2.1.** Choice of the Outlet Blade Angle

The one-dimensional method used to design the impeller has been described in Chapter 4. It has been shown that various combinations of exit blade angle and exit blade width will satisfy the design requirements. For the four impellers designed as part of the existing family, the exit blade angle was set to -60° from radial. Many reasons led to this decision:

- The low-flow stage will be added to an existing family. It is very important to ensure an adequate matching between all stages to ensure maximum range, head, and efficiency. Keeping a similar exit blade angle will ensure a similar head-flow curve.
- The wake appears to be weaker in a high-backswept impeller as noticed by Farge and Johnson (1990) or Chen et al. (1996). The wake-mixing losses should, therefore, be minimized.
- The stability of the compressor is improved by increasing the exit blade angle (see Chapter 2)

• With a high backward-swept angle, the absolute velocity at the diffuser entrance is lower than the one provided by a radial impeller at an equal power input. A lower loss takes place in the diffuser, improving the stage efficiency.

All this considerations lead to the design of impellers with an exit blade angle of – 60°.

#### **5.1.2.2.** Modeling Assumptions

The performances of the impeller are also affected by the distortion of the incoming flow from hub to shroud. This is an important concern for multistage machines because each impeller (except the first one and last one) may play the role of a front stage or of a rear stage. For a front stage, the flow is coming out of a radial inlet and is rather uniform from hub to shroud.

In case of a middle or a rear stage, the flow entering the impeller exits from a return channel. The last turn from radial to axial and the residual swirl at the exit of the return vane lead to a distorted flow. The curvature of the hub and shroud side highly influences the velocity profile. The incidence at the shroud increases, whereas the one at the hub decreases. Figure D.1 in Appendix D shows the velocity profile at the impeller inlet obtained from a CFD simulation. A parameter AK=Cm<sub>shroud</sub>/Cm<sub>mean</sub> is used to characterize this distortion. AK increases as the curvature of the bend increases, i.e. as we go towards lower flow coefficient compressors.

The objective for the sizing of these impellers was to maintain similar velocity triangles between the four impellers at inlet and exit. This procedure does not necessarily minimize the inducer tip Mach number, but the Mach number value is not really an issue

for these low flow stages (Mw1tip ≈ 0.4). Also it was shown in Chapter 4 that the minimum Mach number as a function of tip-to-hub ratio was relatively flat.

Table 5.1 shows the inlet conditions and dimensions used for each impeller.

**Table 5.1 Impeller main dimensions** 

	AA	AB	AC	AD
P00 (psi)	750	888.9	1049	1263
T00 (R)	580	607	635	664
R1t (")	4.18	4.13	4.06	4.00
β1h (°)	-64.49	-65.7	-65.1	-65.0
β1t (°)	-62.66	-63.4	-63.5	-63.0
b2 (")	0.4	0.36	0.32	0.28
β2 (°)	-60	-60	-60	-60

A constant deviation of 4° for the primary zone and an MR2 value corresponding to the state of the art lead to the velocity triangles presented in Table 5.2. These assumed values are slightly different from those used in Chapter 4. The main concern here was to ensure continuity between these four designs and the existing family of impellers.

**Table 5.2 Design velocity triangles** 

	AA	AB	AC	AD
$C_{m1}/U_2$	0.218	0.210	0.208	0.209
$C_{m2}/U_2$	0.183	0.181	0.179	0.183
$C_{u2}/U_2$	0.573	0.578	0.585	0.581
$\alpha_{2m}$	72.3	72.6	73.0	72.5
$W_2/U_2$	0.465	0.459	0.452	0.457
W <sub>2</sub> /W <sub>1tip</sub>	0.74	0.75	0.75	0.76
$C_{m2}/C_{m1}$	0.84	0.86	0.86	0.88
σ (slip factor)	0.890	0.893	0.894	0.899
$\eta_{t-t}$ rotor (w/o leak) (%)	93.4	93.4	93.3	93.2

The revised performance prediction will be presented in Chapter 6.

## 5.2. Streamline Curvature Throughflow Analysis

## **5.2.1.** Geometry

The meridional contour and blade angle distribution were set to satisfy the following criteria:

- Smoothness of the curvature and slope distribution of the meridional contours
- Acceptable velocity distribution
- Acceptable blade loading
- Reasonable lean angle distribution

The blade thickness distribution was kept identical to the A1 impeller. The impeller exit rake angle was set at 15°. The choice of the velocity distribution and the blade loading have been discussed in 3.2.1.3.

The meridional contour and blade angle distribution for the AA, AB, AC, and AD impellers are shown in Figure 5.5 and in Figure 5.2. They have been obtained after a few iterations between the streamline curvature throughflow analysis and the CFD analysis.

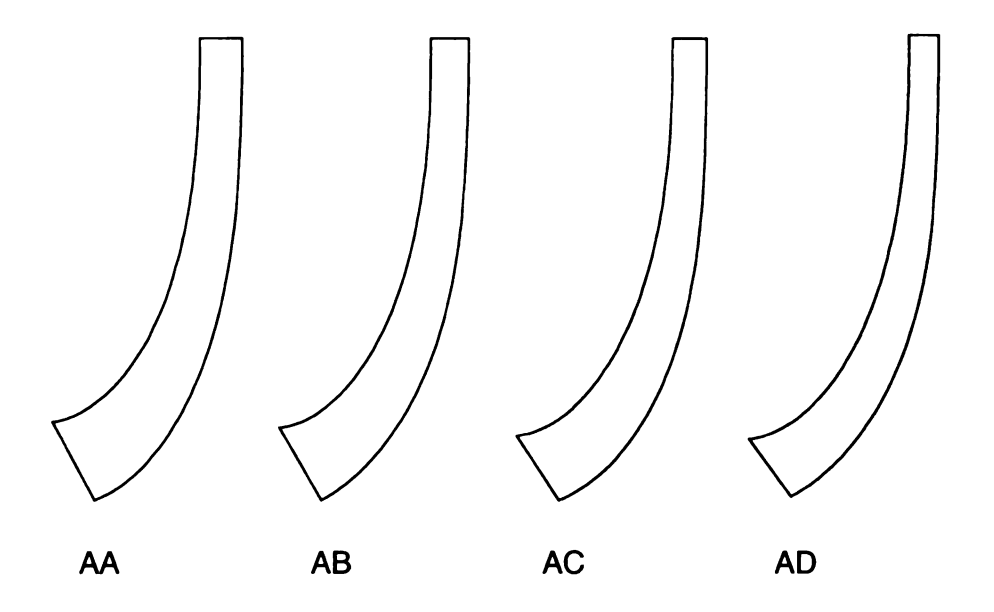


Figure 5.1 Meridional contours of impellers

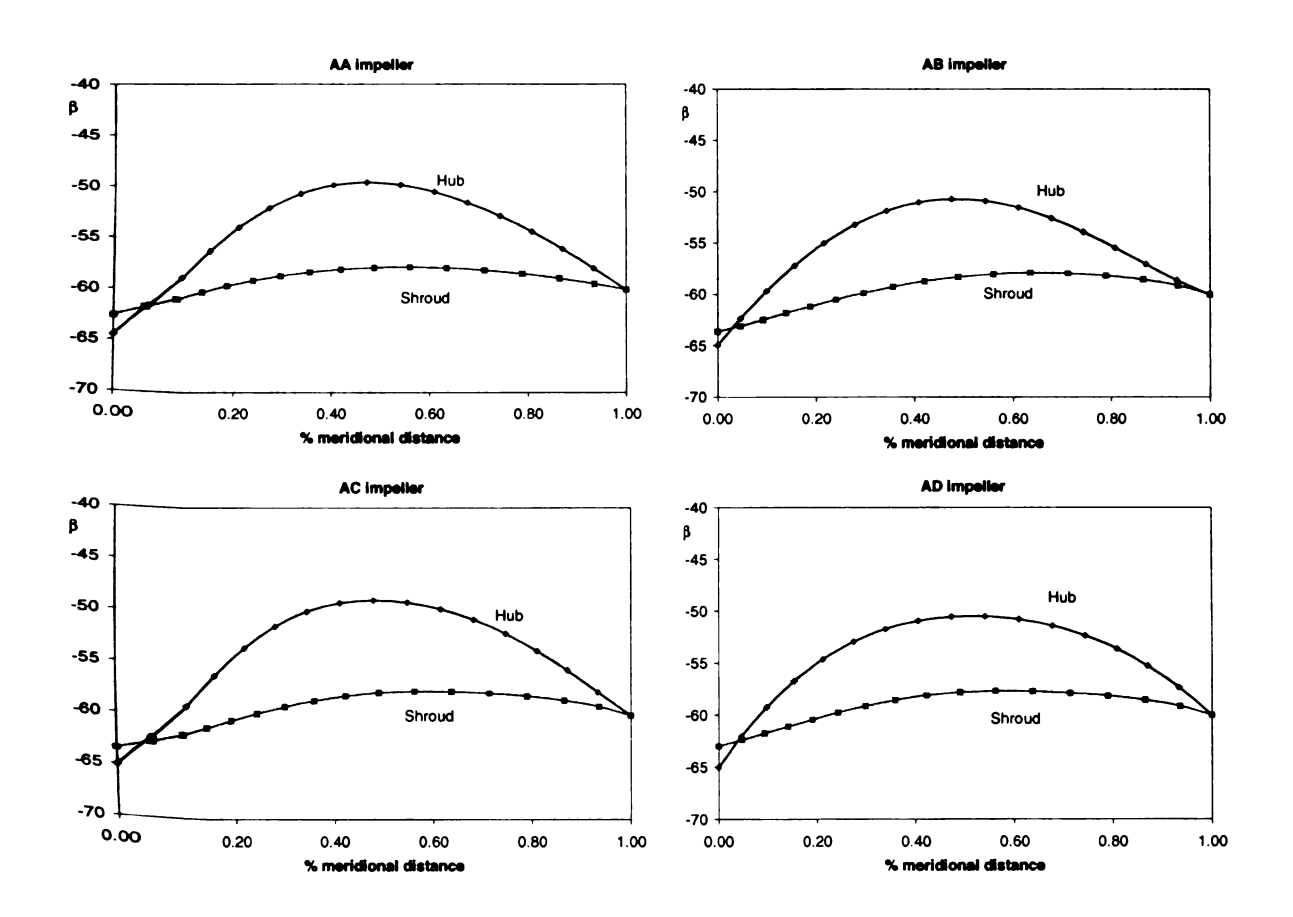


Figure 5.2 Blade angle distributions

#### **5.2.2.** Streamline Curvature Analysis

The velocity distributions along the impeller at the hub, mean, and shroud are shown in Figure 5.3 for the AA impeller.

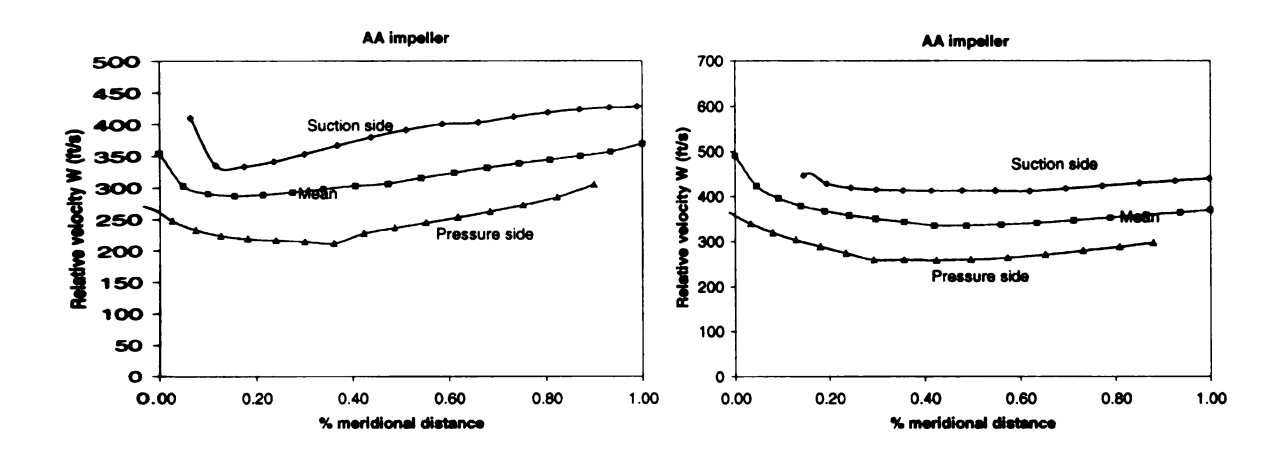


Figure 5.3 Relative velocity distribution at hub (left) and shroud (right) for the AA impeller at design point

The blade-to-blade loadings obtained with the streamline curvature program for the four low-flow stages are shown in Figure 5.4. The method assumes a linear variation between pressure and suction side. They were calculated based on the assumption of a slip factor of 0.85, from which the exit momentum was calculated. The values of the maximum loading are located around 50% of the meridional length and are all below 0.65. The apparent discontinuity in the blade loading results from the imposed outlet momentum, which forces the tangential velocity to match the prescribed value.

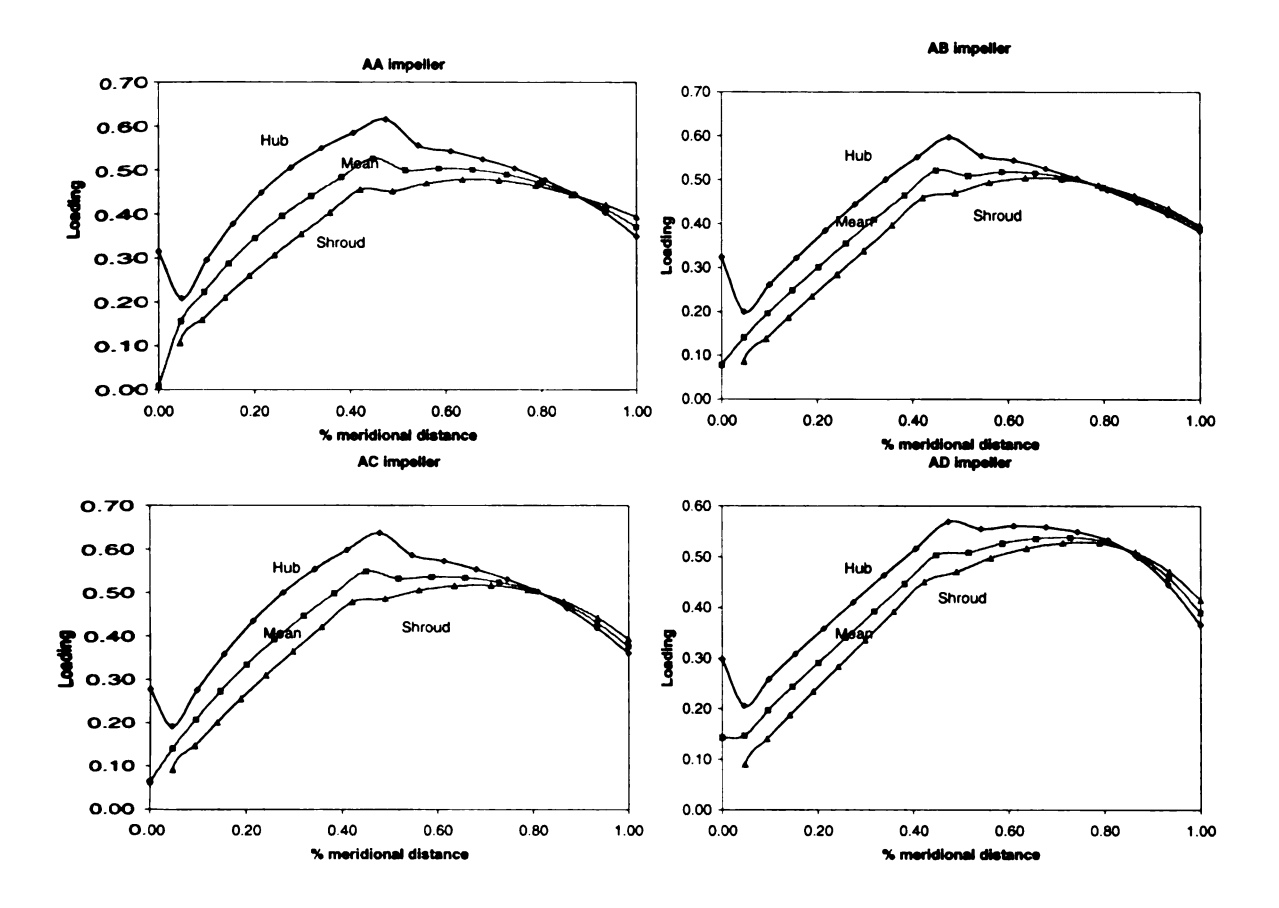


Figure 5.4. Blade-to-blade loading

## 5.3. CFD Analysis

## 5.3.1. Presentation of the Commercial Software TASCflow

The 3-dimensional viscous code used for the flow field analysis is the commercially available code TASCflow (version 2.7) from AEA Technology. TASCflow is a general purpose CFD software package for a wide range of industrial applications. It can solve incompressible as well as compressible flows. The code has been used by many researchers. Its capability to describe the flow characteristics in centrifugal machines has

been shown by various authors (Cooper et al. 1994, Howard and Ashrafizaadeh 1994, or Flathers and Bache 1996). Dalbert and Wiss (1995) compared the numerical simulations of the NASA compressor Rotor 37 performed with the Dawes code (BTOB3D) and with TASCflow to the detailed experimental measurement performed at NASA. Both codes provided good predictions of overall values. The efficiencies were predicted to within +/-1.5%. The total-to-total pressure ratio was slightly over-predicted especially at off-design conditions. The turbulence model of TASCflow was considered to be superior to the classical Baldwin-Lomax model used in the Dawes code. Based on these encouraging reports, TASCflow was chosen to model the impellers.

#### **5.3.2.** Equations Solved

The equations solved are the Reynolds-stress averaged Navier-Stokes equations in primitive variable form, and the time-averaged mass and energy equations in the rotating frame of reference. The equations are expressed in a finite-volume formulation, which is fully conservative. In the mean form, the equations solved are as follows.

The conservation of mass:

$$\frac{\partial \rho}{\partial t} + \frac{\partial}{\partial x_j} (\rho u_j) = 0$$

The conservation of momentum:

$$\frac{\partial}{\partial t}(\rho u_i) + \frac{\partial}{\partial x_j}(\rho u_j u_i) = -\frac{\partial p}{\partial x_i} + \frac{\partial}{\partial x_j}\left\{\mu_{eff}\left(\frac{\partial u_i}{\partial x_j} + \frac{\partial u_j}{\partial x_i}\right)\right\} + S_{ui}$$

where  $\mu_{eff}=\mu+\mu_t$ .  $S_{ui}$  is the momentum source term. For flows in a rotating frame, the effect of Coriolis and centripetal forces are modeled in the code by

$$\vec{S}_u = -2\vec{\Omega} \times \vec{U} - \vec{\Omega} \times (\vec{\Omega} \times \vec{r})$$

The energy equation, in which the work of the viscous forces is neglected, is solved

$$\frac{\partial}{\partial t}(\rho H) - \frac{\partial P}{\partial t} + \frac{\partial}{\partial x_{j}}(\rho u_{j}H) = \frac{\partial}{\partial x_{j}}\left(\lambda \frac{\partial T}{\partial x_{j}} + \frac{\mu_{t}}{Pr_{t}} \frac{\partial h}{\partial x_{j}}\right) + S_{E}$$

$$+ \frac{\partial}{\partial x_{j}}\left\{u_{i}\left[\mu_{t}\left(\frac{\partial u_{i}}{\partial x_{j}} + \frac{\partial u_{j}}{\partial x_{i}}\right) - \frac{2}{3}\mu_{t} \frac{\partial u_{t}}{\partial x_{t}}\delta_{ij}\right]\right\}$$

where the total enthalpy is defined by  $H = h + \frac{1}{2}u_iu_i + k$ .

In the rotating frame of reference, the rotal  $I = H - \frac{\omega^2 R^2}{2}$  is advected in the energy equation in place of the total enthalpy.  $\omega$  is the rotational speed, and R the local radius.

The computational technique used to solve these equations is classified as pressure based, as opposed to density based time marching. The discretization scheme is second-order accurate. It uses a directionally sensitive, upwind discretization scheme known as Linear Profile Skew upwinding (LPS) (Raithby 1976) combined with a physically based correction term known as Physical Advection Correction (PAC) (Van Doormaal et al. 1987). These features retain false diffusion and false total pressure losses that would occur due to flow directionality and streamwise gradients but at a very low level.

The turbulence model used is a standard k-\varepsilon model combined with a wall function approach. The wall function approach eliminates the necessity of discretely resolving the large gradients in the thin near-wall region. The wall function equations have been

derived under the assumption that the nearest grid point to the surface has a  $y^+$  value between 30 and 500, where  $y^+ = \frac{\rho y_w u_\tau}{\mu}$ . Here,  $y_w$  is the distance from the wall and  $u_\tau$  is the friction velocity. This condition was very important to produce grid independent results.

#### **5.3.3.** Boundary Conditions

The boundary conditions used were as follows:

- The inlet total pressure and temperature were specified at the inlet upstream of the impeller (see the meridional view in Figure 1.1). The flow was assumed to be swirl free.
- The mass-flow rate is given as an exit boundary conditions at the exit of the diffuser.
- A periodic boundary condition is used for the side walls because only one impeller
   passage is modeled.
- The calculations are made in the rotating frame of reference. The whole grid is rotating. Because the inlet walls and the diffuser walls are stationary in reality, they are counter-rotating in the CFD calculations. They therefore appear stationary.
- A symmetry condition is used at the inlet and at the exit to represent, in a first approximation, the flow that may recirculate through the clearance of seals. No shear forces are applied to the fluid in this small region.
- The walls were modeled as hydraulically smooth.

The labyrinth seals have not been modeled in this study. It is believed that the flow will not be affected by their presence at the design point. It is understood that this approximation becomes less valid at off-design conditions.

#### **5.3.4.** Grid Specifications

The computational domain consists of part of the inlet duct, a whole blade passage with the blade in the center, and a sector of the vaneless diffuser. The length of the axial duct is about twice the axial length of the impeller, and the diffuser outlet radius is twice the impeller exit radius. The impeller grid uses an H-grid topology.

In all the models used, the computational grid consisted of 127 nodes in the streamwise direction with 70 nodes inside the impeller, 25 nodes in the pitchwise direction (J) and 25 in the spanwise direction (K). Different node numbers and grid densities were tested. It appeared that the main condition needed to obtain a grid independent solution was to respect as much as possible the criteria on y+ (Di Liberti, 1997). Once an adequate node distribution close to the node surface was established, it was found on a qualitative basis and on a one-dimensional basis that the results become independent of the grid node number (75,000 and 100,000 nodes).

The meridional view in Figure 5.5 is a projection in the meridional plane as explained in Chapter 4. The blade-to-blade view in Figure 5.6 corresponds to a projection in the  $m-\theta$  plane.

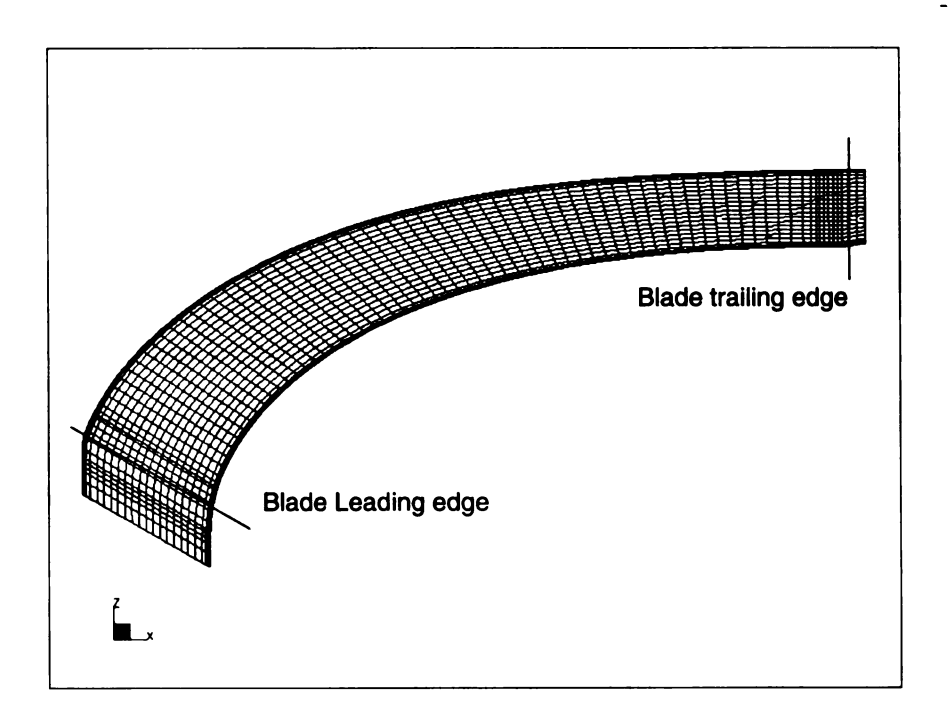


Figure 5.5 Meridional view of calculation grid (impeller only)

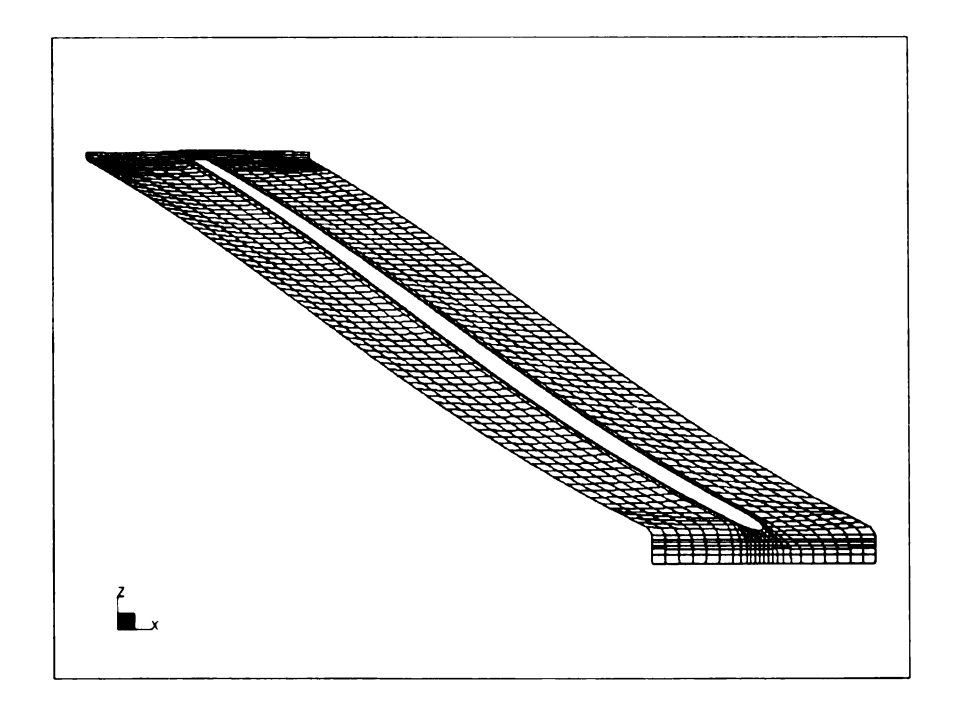


Figure 5.6 Blade-to-blade view of the calculation grid (impeller only)

## **5.3.5.** Convergence Criteria

The convergence was attained when the maximum residual for the pressure and for the three components of velocity was smaller than 1E-04. This represents a convergence by more than three orders of magnitude. It was found that the solutions were identical both qualitatively and on a one-dimensional basis to the solutions obtained with a maximum residual of 1E-05 (Di Liberti 1997).

Each calculation takes approximately 9 to 12 hours of CPU time on a Sun Ultra Sparc workstation.

## 5.4. Qualitative Analysis of the Flow Field

All four impellers have been modeled with TASCflow. The flow will now be qualitatively described in the meridional and blade-to-blade plane in terms of meridional velocity to detect zones of low-momentum, relative flow angle (to compare the deviation of each zone), and of turbulent kinetic energy. High values of the turbulent kinetic energy can be found in regions of mixing and in regions of unsteady flow (Pinarbasi and Johnson 1994).

#### 5.4.1. Flow at Design Point in the AA Impeller

The velocity vectors in the meridional plane show a flow following the meridional contour in all the surfaces between the blades (Figure 5.7). On the pressure side and on the suction side, the secondary flows show a tendency of the flow to move towards the

shroud (Figure 5.8). The curvature of the meridional contour is responsible for these secondary flows. For this impeller with no inducer, the curvature of the axial-to-radial bend dominates the effect of the blade curvature.

In the blade-to-blade plane (not shown), the flow remains attached to the blade because the incidence levels are still low. The flow is well guided by the blades from hub to shroud.

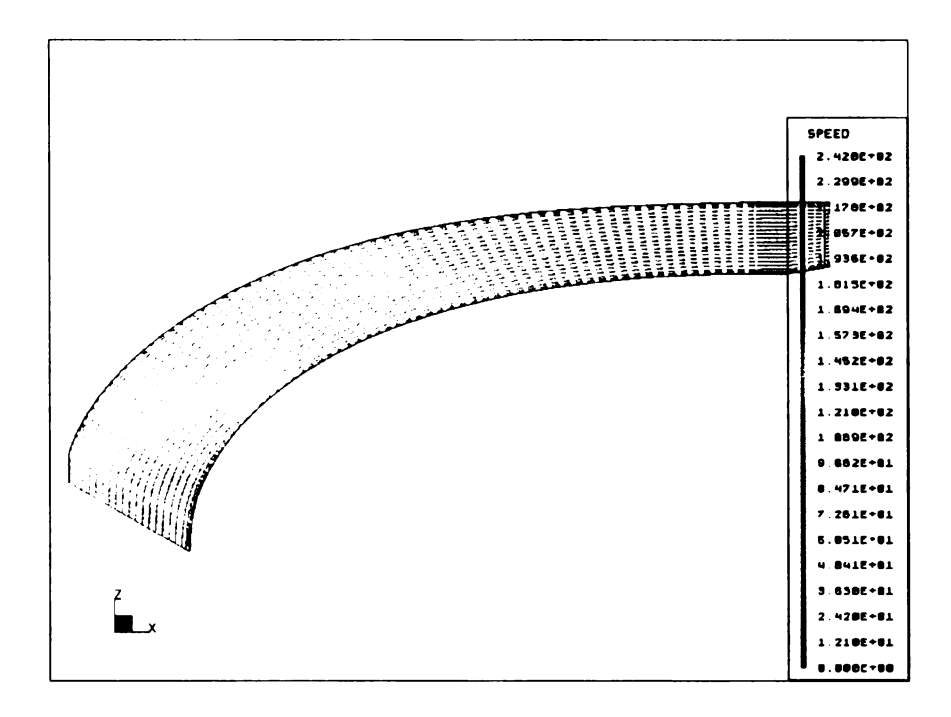


Figure 5.7 Velocity vector at mid pitch (AA impeller, design point)

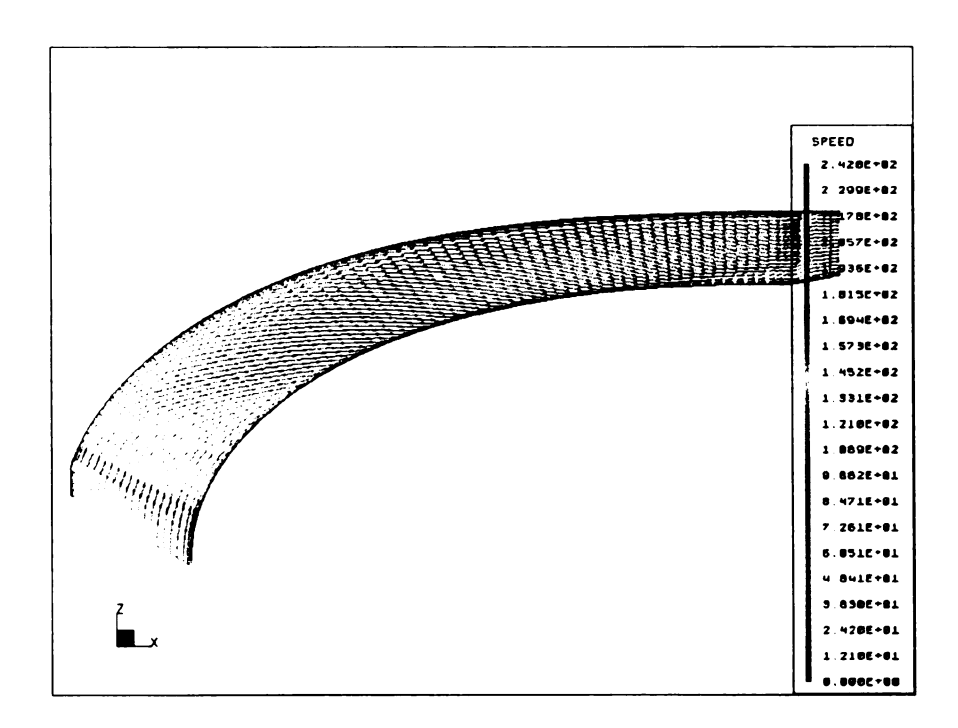


Figure 5.8 Velocity vector near the suction side (AA impeller, design point)

The flow has been analyzed at five stations along the impeller channel located at 10, 30, 50, 70, and 95% of the meridional contour. The position of the five stations (denoted respectively I, II, III, IV, and V) is shown in Figure 5.9. The objectives were to:

- analyze the development of the flow as it goes through the impeller channel from inlet to exit
- identify the possible presence of a secondary zone on the shroud suction corner
- determine the influence of mass flow rate on the location and on the extent of it

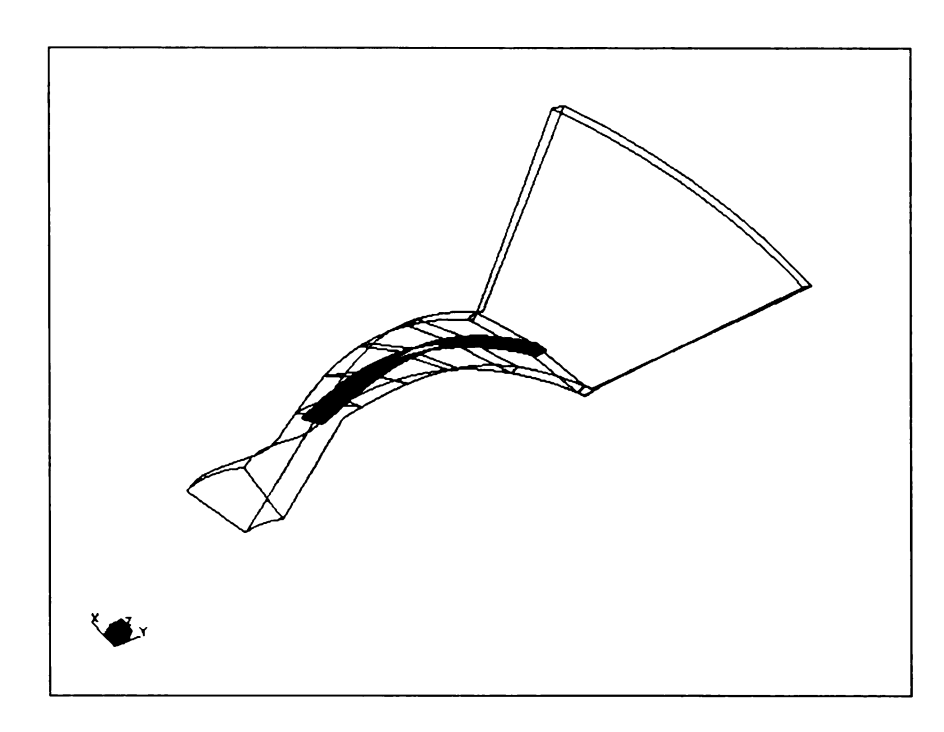


Figure 5.9 Calculating stations along the impeller channel

In Figure 5.10 to Figure 5.14, the shroud is at the top of the picture, the suction side is on the right, the hub is at the bottom, and the pressure side is on the left. As the calculations have been made with the blade in the center of the passage, one of the surfaces has been rotated to obtain a picture of the flow as it will appear between two blades. It should be mentioned that each station corresponds to a line of constant I (streamwise direction), and the resulting plane is not normal to the flow.

For the impeller at the design flow, the meridional velocity distribution at inlet is nonuniform from hub to shroud. The curvature of the inlet section generates a higher velocity at the shroud than at the hub. This can be seen in Figure 5.10, which represents the normalized meridional velocity at station I. Also, as expected, the velocities are higher on the suction side than on the pressure side.

This pattern can still be seen at station II (Figure 5.11) with a tendency for the higher velocities to be located on the right side of the passage. On the shroud suction corner, a small region can be seen with velocity level of the same order of magnitude than near the pressure side.

At station III (Figure 5.12), the velocities near the hub suction side get higher, as expected from the streamline curvature analysis. The small region on the shroud suction side corner can be seen to extend slightly more. This trend continues to develop at station IV. The flow is dominated by the curvature in the meridional plane. As the exit of the impeller is reached, the curvature is less and less important.

The flow pattern changes quickly between station IV (Figure 5.13) and station V (Figure 5.14). The particles of largest velocities can now be found near the pressure side, and to a lesser extent on the hub suction side. A region of low momentum has now clearly developed on the shroud suction side. Its extent will be defined more precisely later as the reduced relative total pressure loss contour will be shown (Figure 5.16).

Figure 5.15 shows the flow angle distribution at station V. It is seen that only a thin region at very high velocities near the pressure side is following the blade. Near the suction side, the flow is under-turned close to the surface at the hub, and following the blade near the shroud. In most of the passage, the average flow angle is between  $-65^{\circ}$  and  $-70^{\circ}$ , confirming the expected large deviation at the impeller exit.

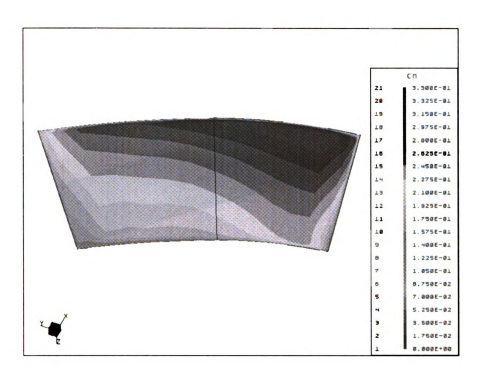


Figure 5.10 Normalized meridional velocity at station I (AA impeller, design point)

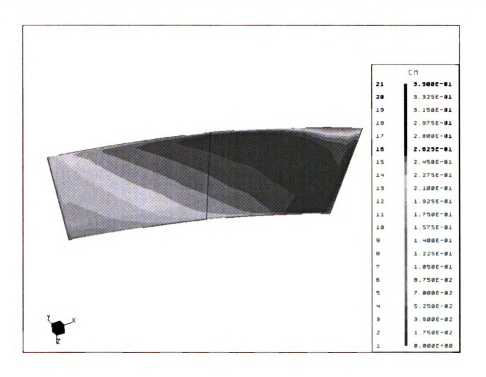


Figure 5.11 Normalized meridional velocity at station II (AA impeller, design point)

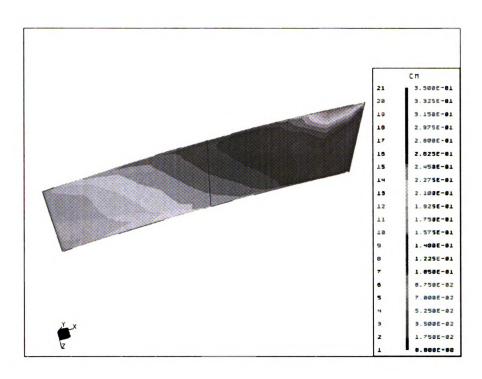


Figure 5.12 Normalized meridional velocity at station III (AA impeller, design point)

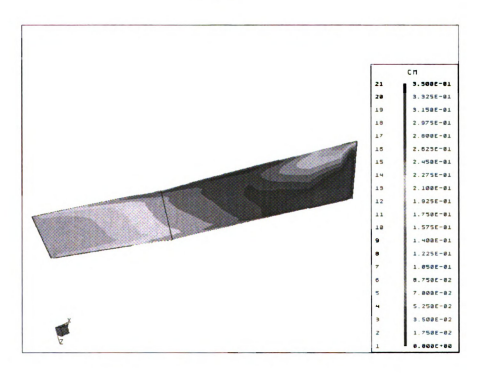


Figure 5.13 Normalized meridional velocity at station IV (AA impeller, design point)

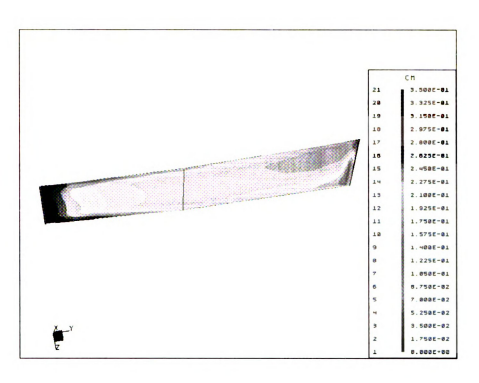


Figure 5.14 Normalized meridional velocity at station V (AA impeller, design point)

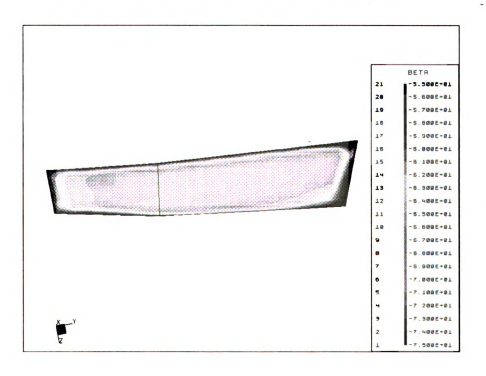


Figure 5.15 Flow angle distribution at station V (AA impeller, design point)

Hence, the two flow regions predicted by the two-zone model do not appear at the exit as distinctly as expected in terms of meridional velocity difference. The secondary zone is located in the shroud suction corner at the design point and seems to follow the blade. Close to the pressure side, the flow follows the blade; whereas the relative eddy seems to be responsible for the deviation of the flow over the entire passage.

The entropy production along the impeller passage is related to the loss in reduced relative total pressure (Eckardt 1975):

$$\frac{P_{tot}^{rel}}{\left(P_{tot}^{rel}\right)_{inlet}} = e^{-\frac{s}{R}}$$

 $(P_{tot}^{rel})_{inlet} = (P_0)_{inlet}$  for a flow with no inlet prewhirl.

The reduced relative total pressure at any grid point is calculated by

$$P_{tot}^{rel} = P \left( \frac{T_{tot}^{rel}}{T} \right)^{\frac{\gamma}{\gamma - 1}}$$

The development of the wake region can clearly be seen in Figure 5.16. A value of 1.0 corresponds to an isentropic flow. A region of small losses can be seen along the suction side at the inlet due to a slightly positive incidence. Then the wake region develops in the shroud suction side corner as explained earlier.

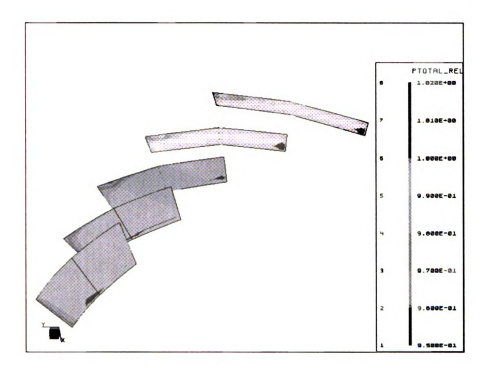


Figure 5.16 Reduced relative total pressure (normalized by P0 at inlet) (AA impeller, design point)

The turbulent kinetic energy at station V is shown in Figure 5.17. The TKE is the largest near the hub and the shroud contour and the lowest near the pressure side and in the middle passage. Intermediate values are found in the secondary zone. The regions of high TKE are found in the boundary layer and in the secondary zone. It is seen that the boundary layer near the pressure side is very thin due to the high velocities.

In the meridional plane, on the suction surface, the TKE levels can clearly be seen to decrease near the shroud at approximately 80% of the meridional length as the flow is laminarized.

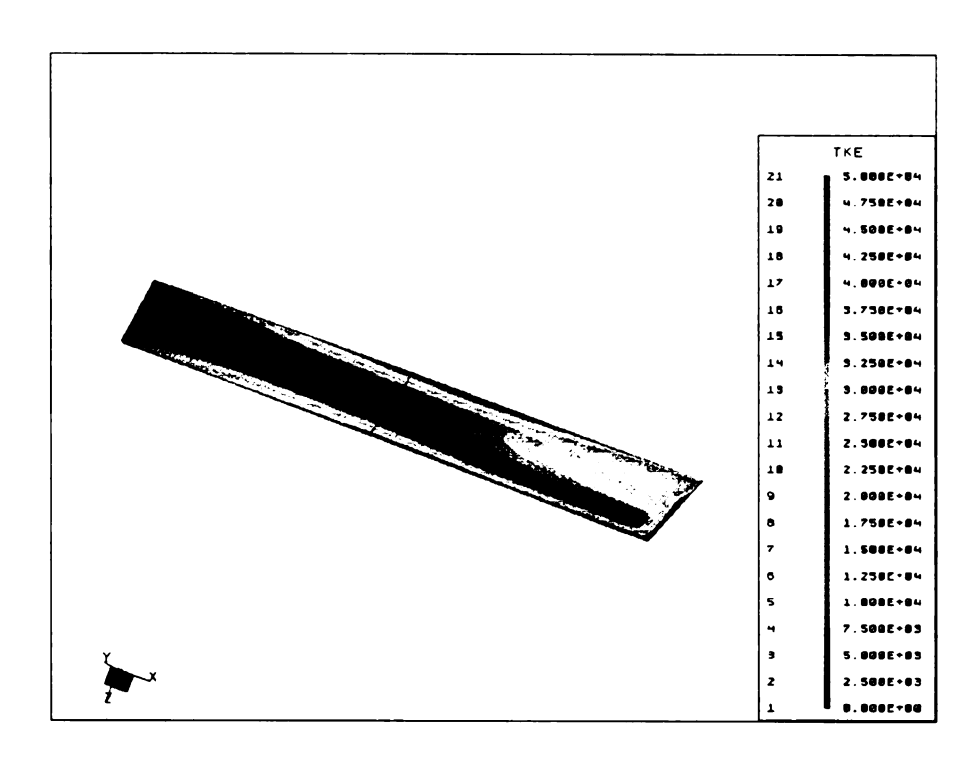


Figure 5.17 TKE distribution at station V (AA impeller, design point)

## **5.4.2.** Flow at Off-design Conditions (AA Impeller)

A simulation of the flow in the AA impeller from 60% to 140% of the design mass-flow rate has been performed. The evolution of the flow will be discussed qualitatively. Only the most relevant figures will be shown in order to keep this section to a reasonable length.

At 80% mass-flow, the flow in the meridional plane at mid pitch is still clean. The flow near the pressure side and the suction side of the blade now tends to move towards the shroud. Near the inlet, 10% away from the suction surface, a very small recirculation bubble can be seen on the shroud contour, which does not extend very much circumferentially. In the blade-to-blade view, near the shroud, this small disturbance of

the flow can be noted. Because only the velocity vectors lying on the surface are plotted, the fact that there is a recirculation along the flow path can not be seen from this plot.

At station V, the secondary zone has moved towards the hub. A region of constant velocity extends to most of the passage, the highest velocity still being located near the pressure side. The flow angle shows the highest deviation near the hub-suction side corner (around  $-13^{\circ}$ ). The flow near the pressure surface and near the suction surface follows the blade.

At 70% mass-flow rate, the recirculation on the shroud contour is very large on the suction surface and can be felt right up to the mid-passage. The velocity distributions at section I, II, and III are strongly affected by this recirculation. Low velocities can now be seen on the shroud at section I, mainly close to the suction surface. The incidence has become clearly positive at the hub. The high turbulent kinetic energy (TKE) occupies half of the passage towards the suction side. Low values of TKE are associated with the primary zone. A large area with a high deviation angle occupies the hub of the blade passage.

At 60% of the design mass-flow, the flow is separated on the shroud side. The separation extends from the shroud surface, past the mid-channel (Figure 5.19). The secondary zone occupies now most of the area near the shroud side from hub to shroud.

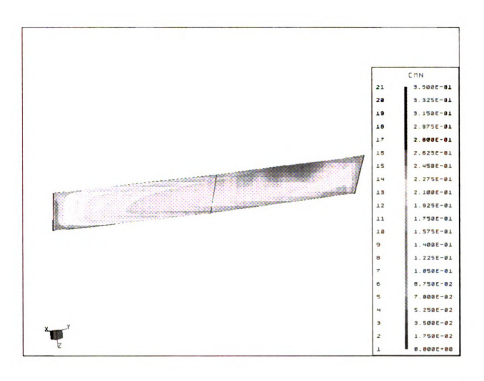


Figure 5.18 Normalized meridional velocity at station V (AA impeller, 70% flow)

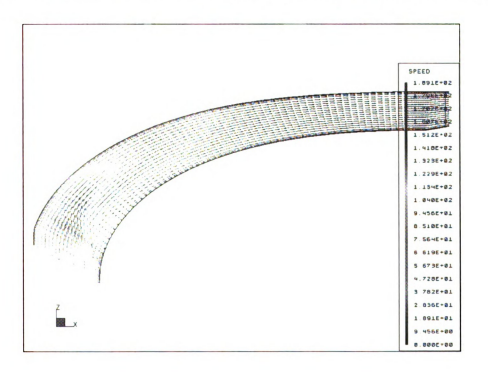


Figure 5.19 Velocity vectors at mid-pitch (AA impeller, 60% mass-flow)

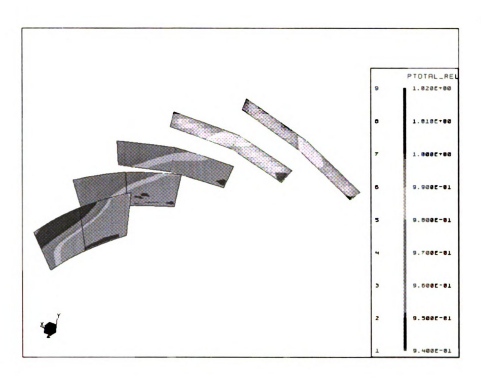


Figure 5.20 Reduced relative total pressure (AA impeller, 60% mass flow)

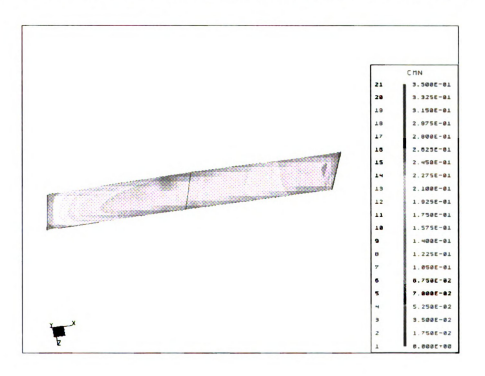


Figure 5.21 Normalized velocity distribution (Station V, A impeller, 60% mass flow)

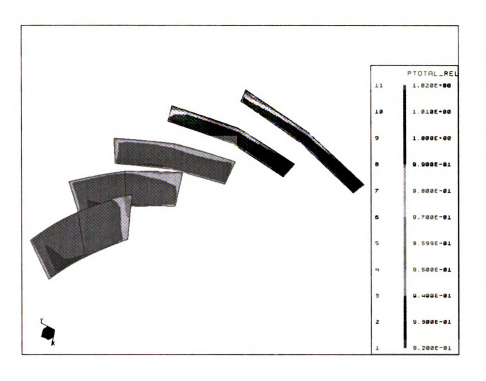


Figure 5.22 Reduced relative total pressure distribution (AA, 140% mass flow)

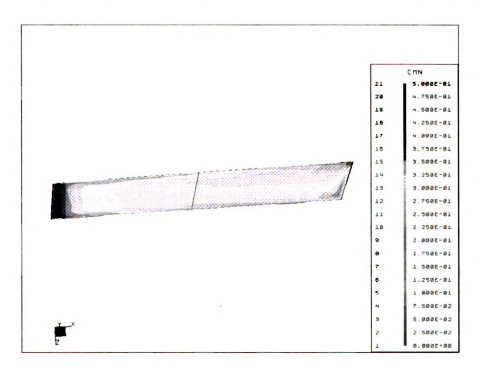


Figure 5.23 Normalized velocity distribution at station V (AA, 140% massflow)

Above the design point, the secondary zone becomes smaller. Figure 5.22 shows the reduced relative total pressure (normalized by the inlet total pressure) along the impeller for the AA impeller at 140% mass flow rate. The secondary zone is located very close to the shroud and near the suction side. At the inlet, positive incidences on the pressure side can be noticed.

The normalized meridional velocity is shown in Figure 5.23. The velocity distribution is very similar to the one at the design point.

This detailed qualitative analysis of the flow field showed the presence of a primary zone and of a secondary zone at the impeller exit. The secondary zone is clearly seen as a zone of low momentum with no backflow. Its position is seen to be close to the shroud surface above and at the design point and to extend towards the hub as the mass flow rate is reduced. The development of the wake is similar to the one reported by Johnson and Moore (1983) except near the exit, where the high backsweep angle reduces the wake development.

#### 5.4.3. Comparison Between AA and AD

The AA, AB, AC, and AD impellers have been designed to be aerodynamically similar in terms of velocity triangle and blade loading. The inlet and exit impeller widths have been adjusted in order to maintain the meridional velocity level at the inlet and outlet. Hence, the flow is qualitatively similar in the impellers, and the normalized meridional velocities can be directly compared. They appear almost identical for the four impellers. The analysis revealed that the incidence at the hub was slighlty too positive for the AC and AD impellers. The curvature of the inlet duct used for the calculation

increases as the inducer tip was reduced leading to a more distorted velocity profile for the lowest flow coefficient impellers. The same effect would be observed if the impellers were run as middle stages, and it was therefore decided to reduce the incidence rule at the hub.

In all the impellers, the development of the flow from inlet to exit is similar to the AA impeller because the curvature distribution in the meridional plane and the blade angles distribution are similar (Figure 5.1 and Figure 5.2).

In the AB impeller, the boundary layers at hub and shroud occupy a larger relative area than for the AA impeller but are not merged (Figure 5.24). In the AC and AD impellers, the zone of high TKE extends from hub to shroud near the suction side (Figure 5.25 and Figure 5.26). This will generate higher mixing losses, and hence, lower performances should be expected.

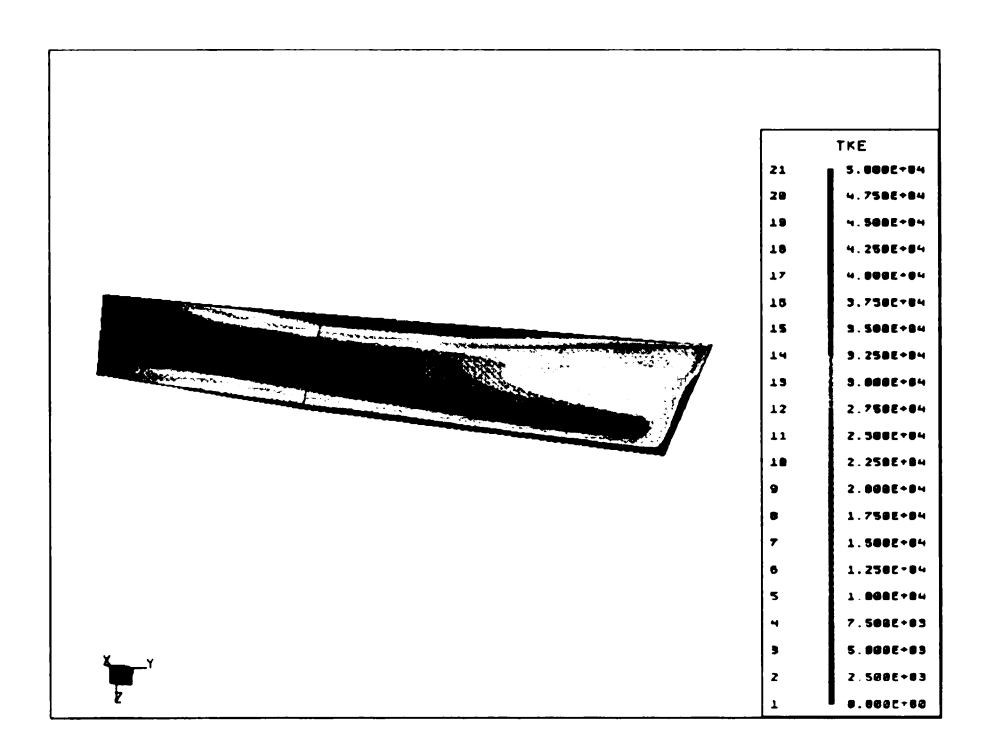


Figure 5.24 TKE at station V (AB impeller, design point)

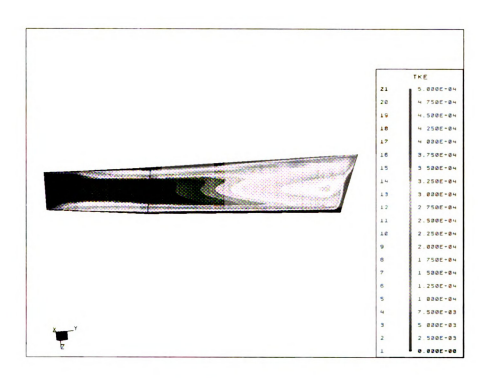


Figure 5.25 TKE at station V (AC impeller, design point)

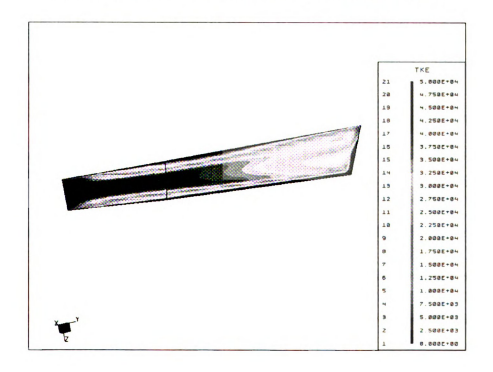


Figure 5.26 TKE at station V (AD impeller, design point)

# 6. COMPARISON OF THE VARIOUS DESIGNS

This chapter presents the quantitative analysis of the AA, AB, AC, and AD impellers and the method used to refine the off-design performance prediction. The CFD analysis of the impellers designed in Chapter 4 are presented qualitatively and quantitatively. The influence of the exit blade angle and exit width on performance is discussed. Two additional impellers (one with a straight leading edge and one with a leading edge located in the radial part) are presented.

## **6.1.** Post-Processing Technique

The CFD calculations are done in a rotating cartesian coordinate system. The velocity in the absolute frame is obtained using the relation discussed in section 2.2:  $\vec{C} = \vec{W} + \vec{U}$ . The components of velocity  $(C_x, C_y, C_z)$  are then converted to cylindrical coordinates  $(C_r, C_u, C_z)$ . Finally, the meridional velocity is calculated from the radial and the axial component through  $C_m = \sqrt{C_r^2 + C_z^2}$ . The static pressure and temperature are directly obtained from the CFD. Hence, all relevant aero-thermodynamic quantities can be calculated.

All quantities can then be mass-averaged at any desired location along the meridional contour and in particular at the stage inlet, at the impeller exit (one node after the trailing edge), and at the diffuser exit.

## 6.2. Quantitative Analysis of the AA, AB, AC, and AD Impellers

#### **6.2.1.** Performance at Design Point

The performances of the AA, AB, AC, and AD stage have been calculated in terms of total-to-total pressure ratio and isentropic total-to-total efficiency based on stage inlet conditions and diffuser exit conditions. The diffuser has been included into the calculation because the performance requirements were defined on a stage basis. Also, it would be difficult to compare an impeller efficiency based on stage inlet conditions and on impeller exit conditions with its one-dimensional equivalent. The one-dimensional method assumes that an instantaneous mixing between the jet and the wake occurs at impeller exit. In the CFD calculation, the mixing of the jet and the wake takes place after the trailing edge and expands into the diffuser.

The TASCflow model does not include the seal leakage, the disc friction losses and assumes a smooth blade surface. High efficiencies are therefore predicted as shown in Table 6.1.

Table 6.1 AA, AB, AC, AD stage performance prediction

	AA	AB	AC	AD
$(\eta_{is})_{tt}$	0.885	0.883	0.878	0.874
$\Pi_{tt}$	1.184	1.175	1.170	1.158

The friction losses are very important in narrow impellers. Koizumi (1983) showed that the wall roughness had a very large influence on the impeller efficiency. In

order to refine the performance prediction, the TASCflow analyses have been rerun for rough walls. An equivalent sand grand roughness of a 120 µinches was assumed for all walls. It corresponds to the value of the rms roughness in the impeller. The wall functions used in the CFD calculations are modified by replacing the constant in the log-law region of the boundary layer by the classic Prandtl-Schlichting sand-grain roughness relation (e.g., White 1991). The same care for the y+ values of the first grid node shall be taken as for the case of smooth walls.

The use of rough walls can be justified using an analogy with a turbulent flow in a pipe. For a pipe of diameter D and roughness k, the roughness is considered as unimportant for (k/D)\*Re<sub>D</sub><10 whereas the flow is considered fully rough for (k/D)\*Re<sub>D</sub>>1000 (White 1991). In case of the AA impeller, the Reynolds number based on the diffuser entrance is of the order of 4.10<sup>6</sup>, which leads to a (k/D)\*Re<sub>D</sub> of approximately 600. This value is in between the two limiting cases mentioned by White and justifies the use of rough walls to improve the CFD predictions.

The qualitative results were similar to the one obtained for hydraulically smooth wall. The regions of high TKE were found to be thicker as the boundary layers were more developed. The predicted efficiencies dropped by 4 points for the AA impeller and up to 6 points for the AD impellers compared to those obtained with hydraulically smooth walls. The pressure ratio dropped to 1.177, 1.168, 1.162, and 1.149, respectively.

#### 6.2.2. Consequence for the 1-D analysis

The quantitative analysis also provided some information on the conditions of the flow at impeller exit. Table 6.2 shows the mass-average velocities, pressure and temperature at the impeller exit.

**Table 6.2 Impellers exit conditions** 

	AA	AB	AC	AD
$C_{u2}$	374.8	377.9	386.9	382.2
C <sub>m2</sub>	140.8	139.8	137.7	141.0
$\alpha_2$	69.4	69.7	70.4	69.7
$\delta_2$	-7.85	-7.78	-7.53	-7.34
P <sub>02</sub>	900.3	1059.4	1268.1	1482.9
P <sub>2</sub>	850.1	1002.3	1200.5	1408.6
T <sub>02</sub>	604.2	631.3	658.9	687.2

This quantitative information has been used together with the analysis of section 4.2.3 and the qualitative analysis of section 5.4 to refine the performance prediction of each impeller. The qualitative analysis of the CFD results has shown that the exit relative flow angle was rather uniform over the exit section. It was therefore decided to use the two-zone model with a deviation of the primary zone equal to the one calculated by TASCflow. The Mach number ratio MR2 was then adjusted to match the primary zone static pressure with the average exit static pressure calculated by TASCflow. This is justified by the fact that the two-zone model assumes that the static pressures of the two zones are equal. Following the discussion of section 4.2.3, the ratio  $\chi$  of the mass in the secondary zone to the total mass flow was increased to 0.20 in order to obtain an aerodynamic blockage  $\epsilon$  of at least 10%.

Using these new model parameters, the total-to-total pressure ratio and isentropic efficiency were calculated. Also, in order to be able to compare directly these predictions with the CFD analysis, the one-dimensional model was run with no external losses (i.e. the disc friction is set to zero and the seals are not taken into account). Figure 6.1 shows the performance prediction at design point obtained with the one-dimensional model

(with and without external losses), with TASCflow (with hydraulically smooth walls and with rough walls).

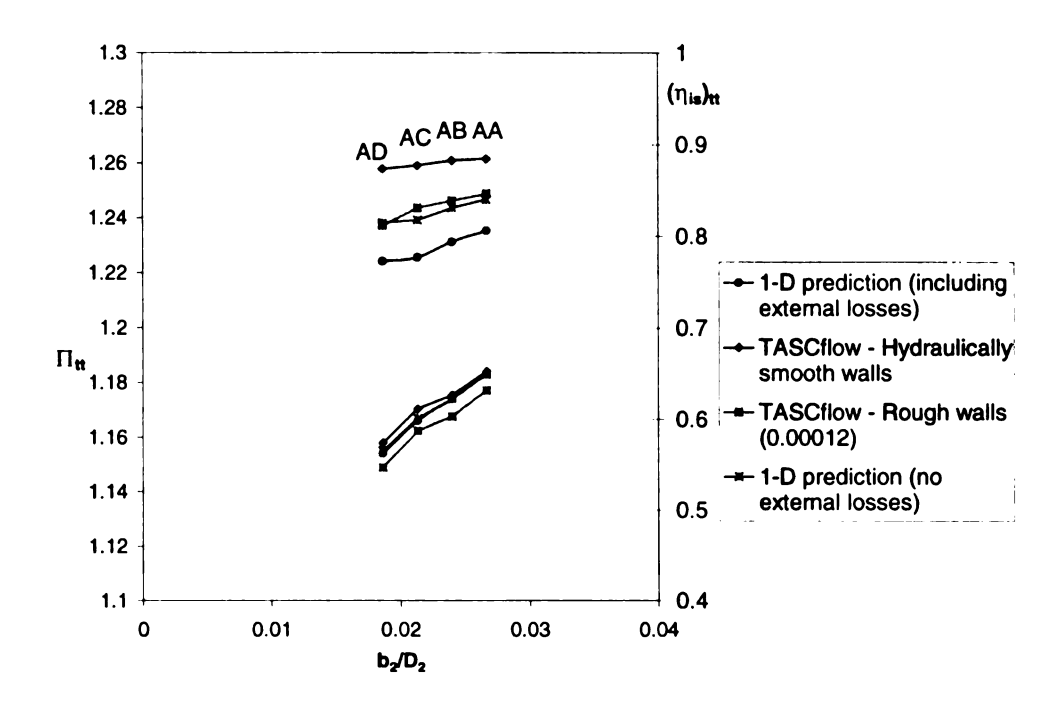


Figure 6.1 Performance prediction for the AA, AB, AC, and AD stages

As already mentioned, the efficiencies predicted by TASCflow for hydraulically smooth walls are too optimistic. The efficiencies predicted by the one-dimensional method were the lowest as they include the external losses. Nevertheless, very good agreement can be found between the TASCflow analysis with rough walls and the 1-D analysis with no external losses, the difference in efficiency being lower than one percentage point. This gives confidence in the method adopted to determine the two-zone model parameters.

In terms of total-to-total pressure ratio, there is no difference between the two one-dimensional methods because the external losses influence only the total temperature at the rotor exit. The one-dimensional prediction lies in between the two TASCflow

analyses, i.e, it over-predicts the total pressure at diffuser exit. The slip factors obtained when setting the deviation of the primary zone to the average value calculated by TASCflow are approximately 0.85. Paroubek et al. (1994) had a slip factor value of approximately 0.80 for impeller with an identical exit blade angle suggesting that the calculated slip factors would be too high.

In terms of diffuser performance, Figure 6.2 shows the diffuser pressure recovery and loss coefficient calculated with TASCflow and the one-dimensional method. The TASCflow calculation with wall roughness predicts loss coefficient 50% greater than for hydraulically smooth walls. It is encouraging to notice that the TASCflow prediction with rough walls agrees well with the one-dimensional prediction method.

The pressure recovery of the 1-D analysis is higher than the one predicted by TASCflow with rough walls. This tendency of the one-dimensional method of Johnston and Dean (1966) to over-predict the pressure recovery is known. A calculation of the diffuser flow with an integral boundary layer method would have helped to obtain a better prediction of the static and total pressure at the same time.

These results show that the TASCflow results obtained with the rough walls model are most accurate and validate the performance prediction method.

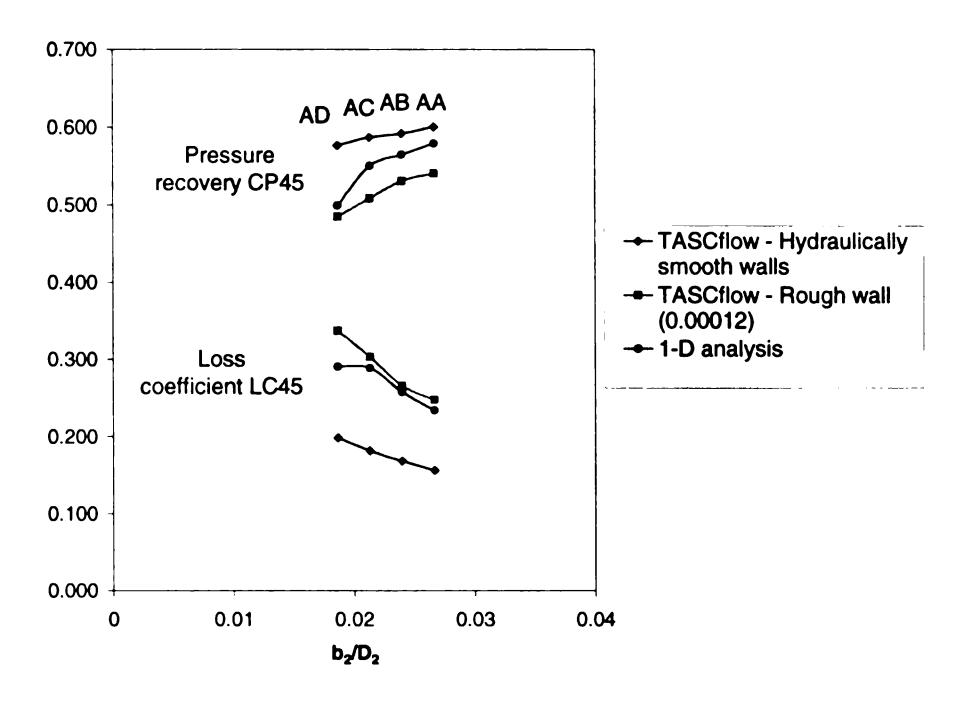


Figure 6.2 Diffuser loss coefficient and pressure recovery

#### **6.2.3.** Determination of the TEIS Models

The use of the TEIS model described in Chapter 4 for the prediction of the operating map requires a number of inputs, which can not be known precisely at the early design stage:

- the effectiveness of the inlet portion  $\eta_a$
- the effectiveness of the passage portion  $\eta_b$
- the diffusion limit DR<sub>stall</sub>
- a distribution of recirculation losses from surge to choke

Based on the experience acquired from the existing family, a constant  $\eta_a$  of 0.78 for all the stages was chosen. No recirculation was assumed at choke and design. 3%

recirculation was assumed at the surge point. The impeller passage effectiveness was determined to match the Mach number ratio at the design point. The maximum diffusion ratio was set to the value of the Mach number ratio incremented by 0.02. The TEIS models presented in Table 6.3 were then obtained.

Table 6.3 TEIS models for the AA, AB, AC, and AD impellers

	$\eta_a$	$\eta_b$	$\sigma_2$	DR <sub>stall</sub>
AA	0.78	0.44	0.846	1.151
AB	0.78	0.42	0.848	1.141
AC	0.78	0.44	0.853	1.141
AD	0.78	0.37	0.853	1.111

## **6.2.4.** Off-design Performance (AA impeller)

The flow in the four impellers has been seen in Chapter 5 to be qualitatively similar. Therefore, CFD calculations at off-design were done only for the AA impeller. The impeller has been run (with hydraulically smooth walls) at off-design conditions between 60 and 140% of the design conditions. The performances in terms of pressure ratio and efficiency have been obtained for the stage and are shown in Figure 6.3. This figure also includes the performance prediction obtained with the TEIS model with and without external losses.

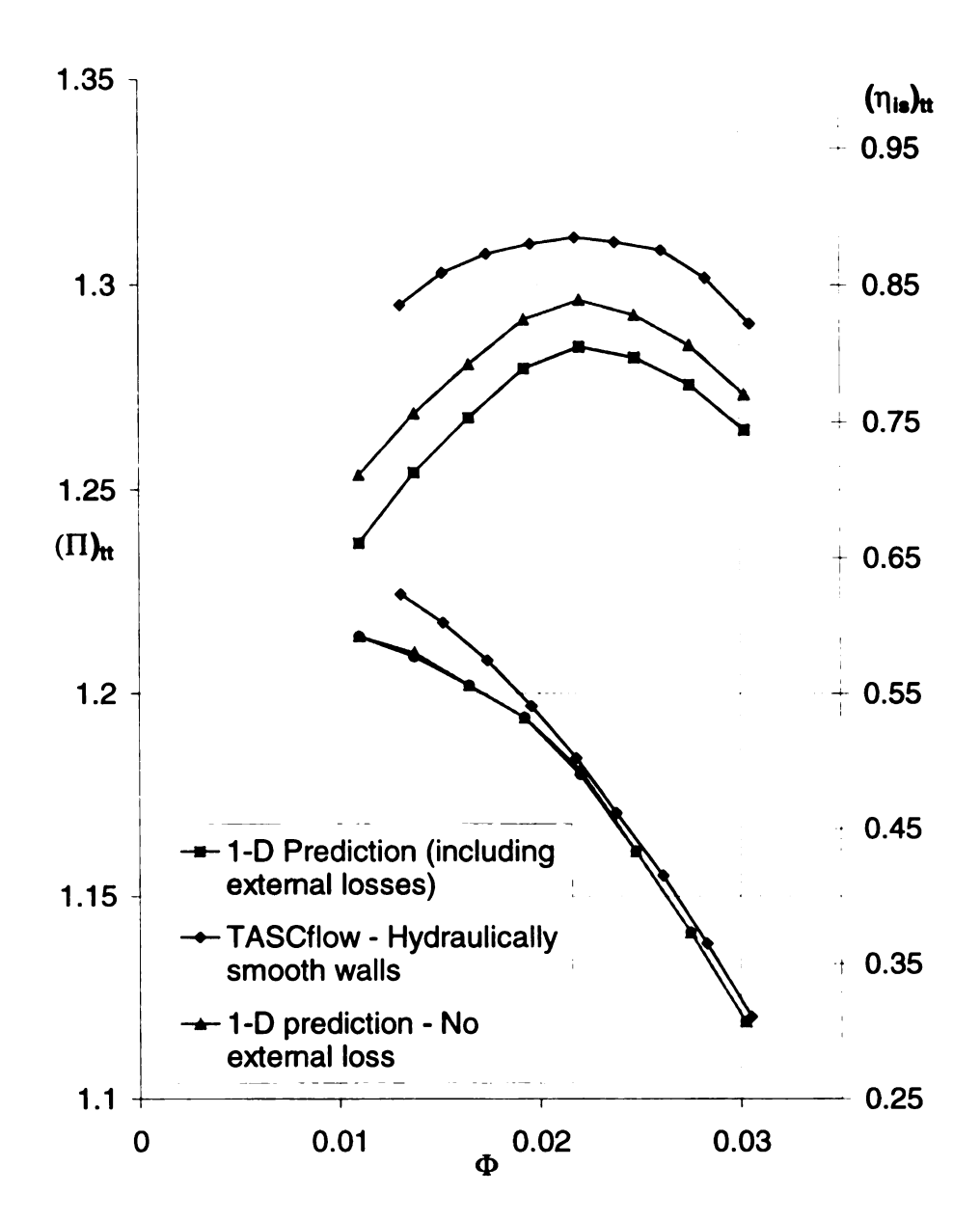


Figure 6.3 Calculated performance map for the AA impeller

The minimum flow rate for the one-dimensional prediction was set by the onset of rotating stall in the vaneless diffuser based on Senoo's criterion.

The shapes of the efficiency curve obtained by the three methods are similar. Based on the conclusion of section 6.2.2, the efficiency curve predicted by the one-dimensional method with external losses is probably fairly good. The pressure ratio is

likely to be slightly over-estimated because a constant slip factor was used for the onedimensional prediction. This slip factor was calculated at the design point in order to match the deviation of the primary zone with the value calculated by TASCflow, and then kept constant throughout the operating map.

It also appears that the criterion used to set the impeller range was not adapted. The qualitative analysis has shown that the impeller will exhibit the first sign of a recirculation at 70% mass flow, and that a large recirculation will take place at 60% mass flow rate. The minimum flow coefficient at which the impeller can be operated will therefore be around 0.015, leading to a useful range of approximately 2. Because the diffuser would stall at a lower flow coefficient, a smaller pinch ratio could have been used, leading to a wider diffuser.

# 6.2.5. Off design performance of the AA, AB, AC and AD stages

Using the TEIS model determined in section 6.2.3, the performance maps for the four impellers were determined. They are shown in Figure 6.4 in terms of isentropic head coefficient and total-to-total isentropic efficiency. The one-dimensional method includes the external losses. As already mentioned in the previous section, the last two operating points (on the left of the map) should correspond to unstable conditions and therefore be avoided.

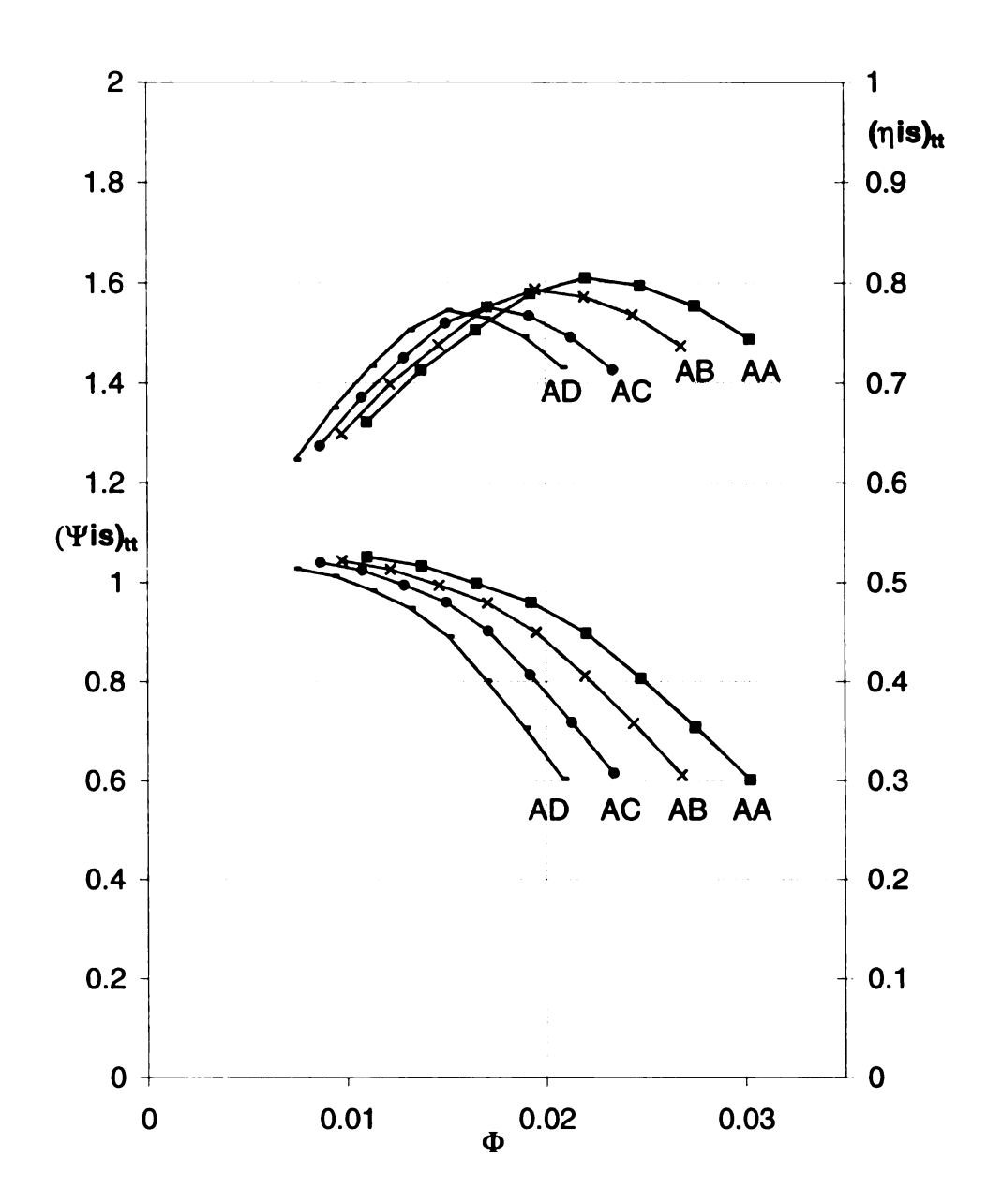


Figure 6.4 Performance map prediction of the AA, AB, AC and AD stages

The isentropic head coefficient and the efficiency decreases from the AA to the AD impeller. This decrease in performance was expected because the impeller exit width was reduced. This is also in agreement with Figure 2.10 showing that impeller efficiency decreases as the specific speed decreases.

Following the discussion of the previous section, the efficiency prediction should be accurate up to one point. The isentropic head coefficient is slightly over-estimated.

## 6.3. Validation of the Loading Estimation

The isentropic relative velocity has been calculated on the pressure and suction surface of the blade to calculate an inviscid loading. The main purpose was to compare the loading obtained by TASCflow with the one predicted by the streamline curvature throughflow method. The separation is expected to occur for blade loading higher than 0.65-0.70.

To calculate the isentropic relative velocity, a streamline from impeller inlet to impeller exit is considered. For a steady isentropic flow, the rothalpy is conserved along this streamline. The isentropic relative velocity is one that will take place on the blade if an isentropic transformation will bring the particle from the inlet total conditions to the local static pressure (calculated by TASCflow).

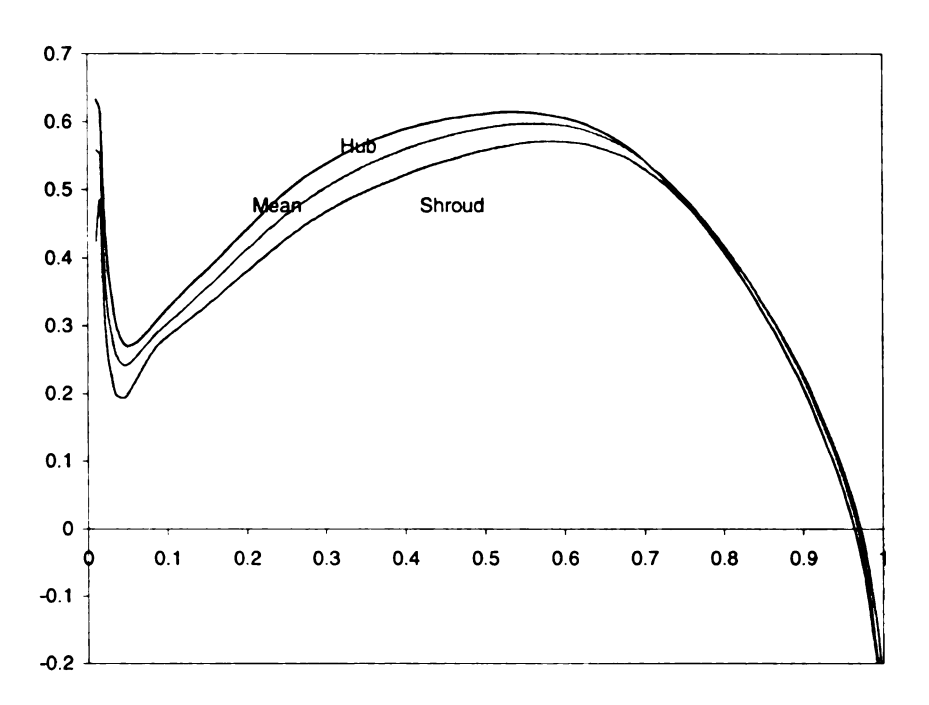


Figure 6.5 Isentropic blade-to-blade loading (AB impeller, design point)

The maximum loadings compare well with the predicted maximum loading of section 5.2.2.

# 6.4. Analysis of the Effect of Exit Blade Angle and Width

## **6.4.1. Qualitative analysis**

The four impellers designed in Chapter 4 (AA50, AA55, AA65, and AA70) were analyzed with TASCflow at design point with hydraulically smooth walls and with rough walls. They cover a range of outlet blade angles between -70 and -50°.

The four impellers exhibited similar secondary flows in the meridional plane to the one discussed for the AA impeller. At the design point, the flow follows the contour, and no zone of recirculation can be seen. Figure 6.7 to Figure 6.9 show the meridional velocity contour at station V for the AA50, AA55, AA65, and AA70. The zone of high meridional velocity near the hub gets smaller from the AA50 to AA55 and disappears in the AA65 and AA70. In these last two impellers, the zone of low meridional velocity extends from hub to shroud. The TKE contour shows that the extent of the zone of higher TKE becomes larger as the backsweep angle is increased (Figure 6.10 and Figure 6.11). The development of the wake, therefore, seems more controlled by the curvature in the meridional plane than by the curvature of the blade in the blade-to-blade plane. The wake mixing losses may therefore be higher in the AA65 and AA70 than in the AA50 and AA65. On the other hand, the velocity levels in the narrow impellers are much smaller, which will counter balance the effect.

In terms of deviation, the relative flow angle plots show that the maximum deviation is located near the center of the blade passage for the AA50 and AA55 and moves towards the shroud for the AA65 and AA70.

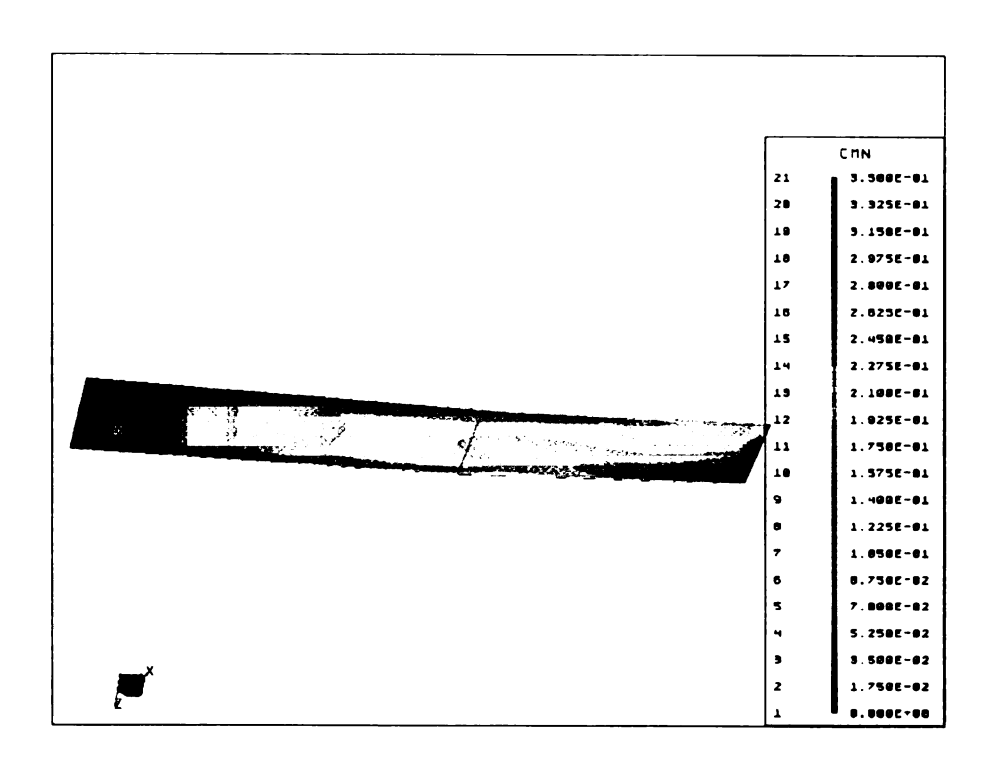


Figure 6.6 Normalized meridional velocity (AA50, design point)

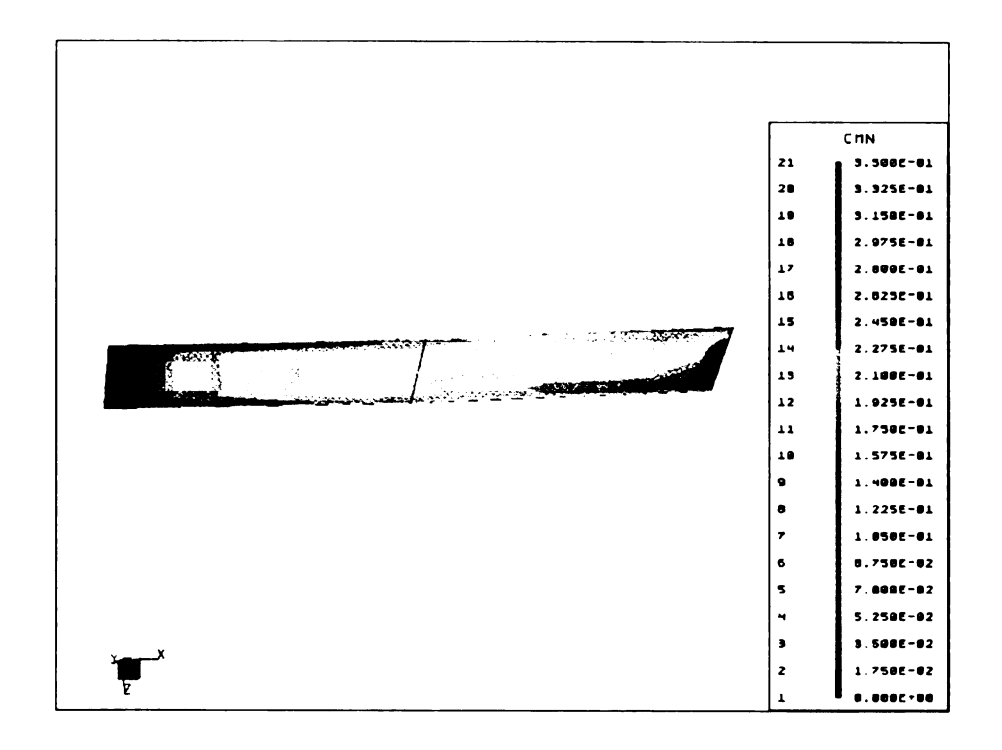


Figure 6.7 Normalized meridional velocity (AA55, design point)

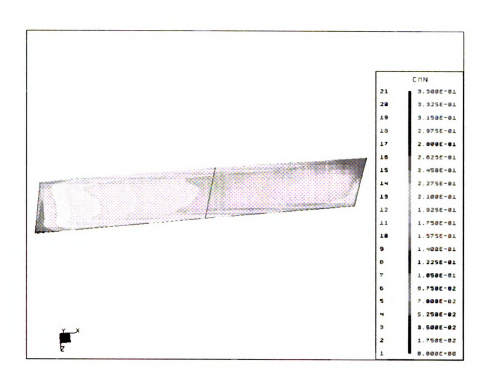


Figure 6.8 Normalized meridional velocity (AA65, design point)

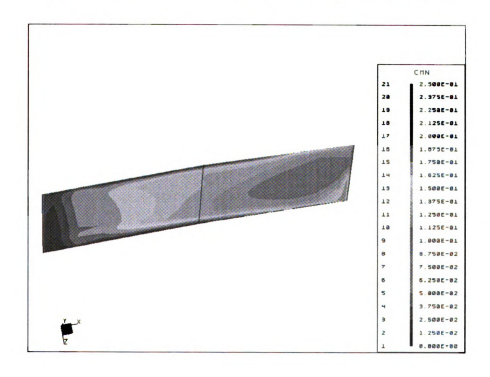


Figure 6.9 Normalized meridional velocity (AA70, design point)

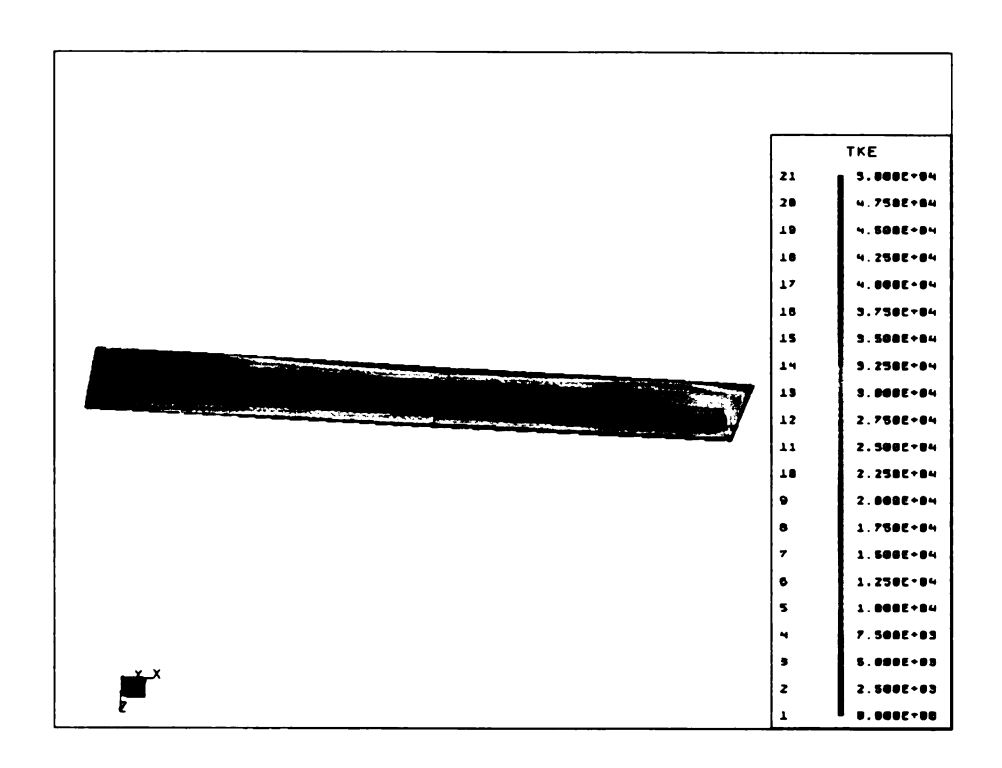


Figure 6.10 TKE contour at station V (AA50, design point)

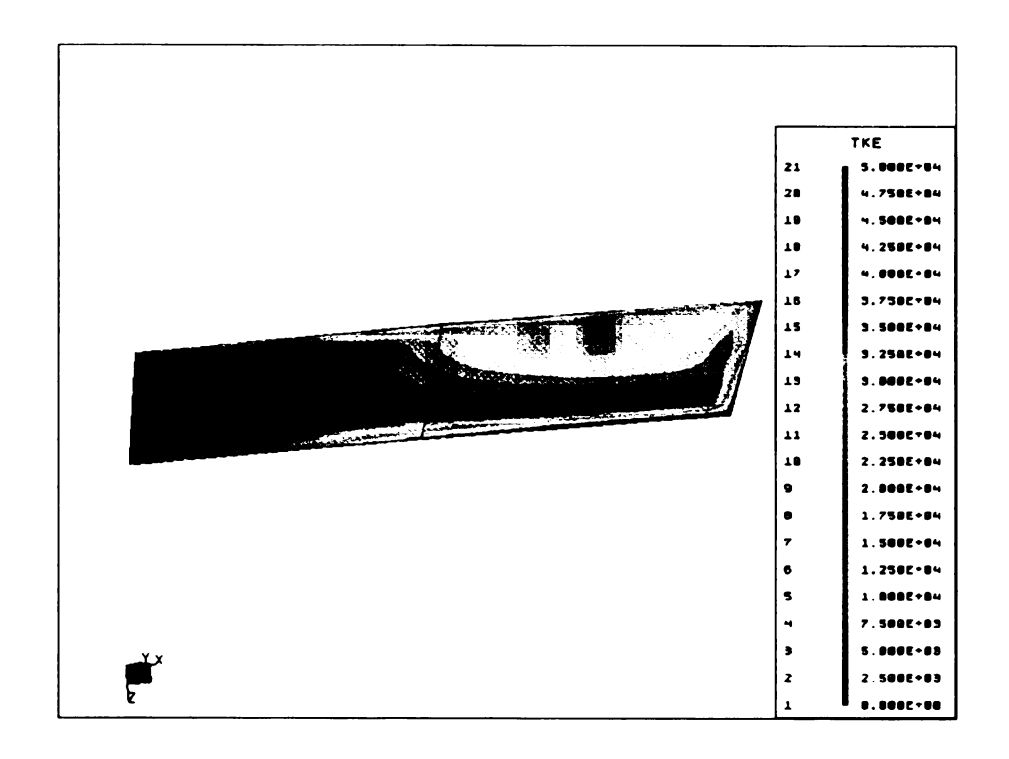


Figure 6.11 TKE contour at station V (AA70, design point)

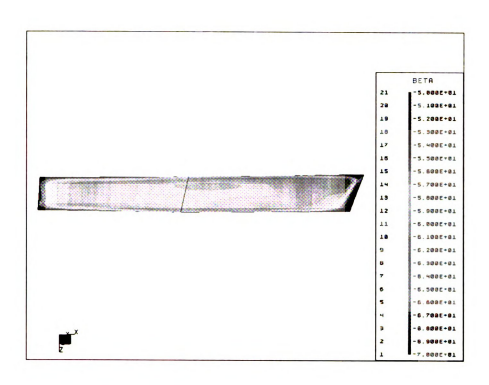


Figure 6.12 Relative flow angle at station V (AA55, design point)

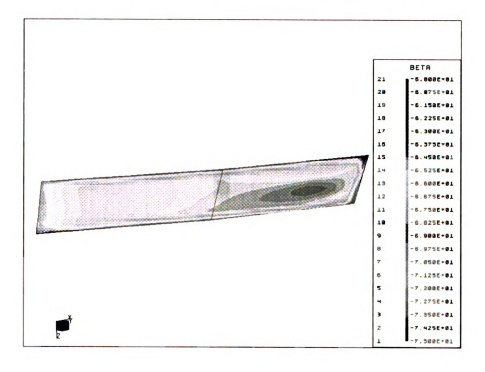


Figure 6.13 Relative flow angle at station V (AA65, design point)

### **6.4.2.** Quantitative analysis

A similar analysis to the one performed for the AA, AB, AC and AD impellers was done for the AA50, AA55, AA, AA65, and AA70 impellers. The quantitative results obtained from the CFD analysis are given in Table 6.4.

**Table 6.4 Impeller exit conditions** 

	AA50	AA55	AA	AA65	AA70
C <sub>u2</sub>	396.6	375.1	374.8	372.7	362.4
C <sub>m2</sub>	185.3	165.3	140.8	117.1	101.6
$\alpha_2$	65	66.2	69.4	72.6	74.3
$\delta_2$	-10.2	-9.4	-7.85	-6.4	-4.2
P <sub>02</sub>	909.6	899.5	900.3	899.5	894.7
P <sub>2</sub>	849.8	847.1	850.1	851.6	850.2
T <sub>02</sub>	605.6	604.2	604.2	604.1	603.4

Figure 6.14 shows the performance of the five impellers obtained from TASCflow with hydraulically smooth walls and with rough walls. The one-dimensional performance predictions at the design point with and without external losses were obtained after updating the two-zone model. The MR2 levels were adjusted to match the static pressure calculated by TASCflow.

The efficiency prediction obtained with TASCflow rough walls is very close to the 1-D prediction with no external losses. The difference is less than one percentage point for all stages. The total-to-total pressure ratio predicted by the 1-D method is higher than the one predicted by TASCflow for the case of rough walls. The apparent jump in pressure ratio between the AA50 and the subsequent impellers is due to the blade angle-exit width combination chosen at design: the absolute tangential velocity at impeller exit is higher than the other impellers (see Table 4.1).

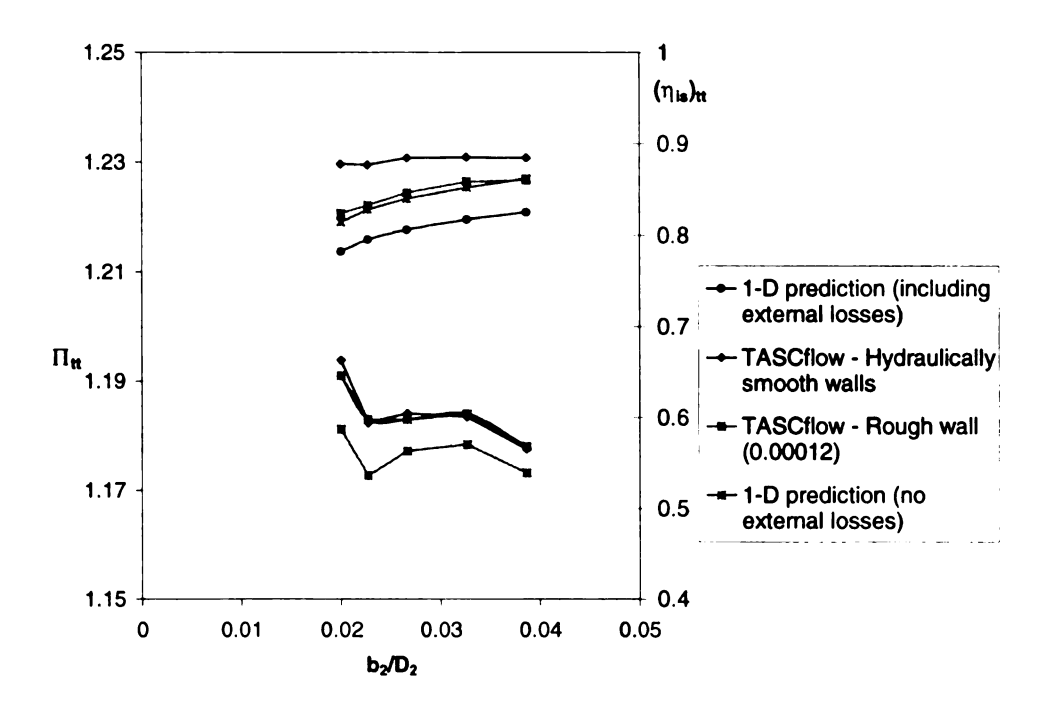


Figure 6.14 Performance at design point

Figure 6.15 shows that the loss coefficient predicted by TASCflow for the case of rough walls is in good agreement with the one-dimensional theory. The pressure recovery obtained from TASCflow is 10% lower than the one predicted by the one-dimensional method. Since the 1-D method is known to over-predict the pressure recovery, these results leads us to believe that the prediction obtained with TASCflow rough walls is the most accurate once external losses are added to it. It also nearly corresponds to the one-dimensional analysis with external losses.

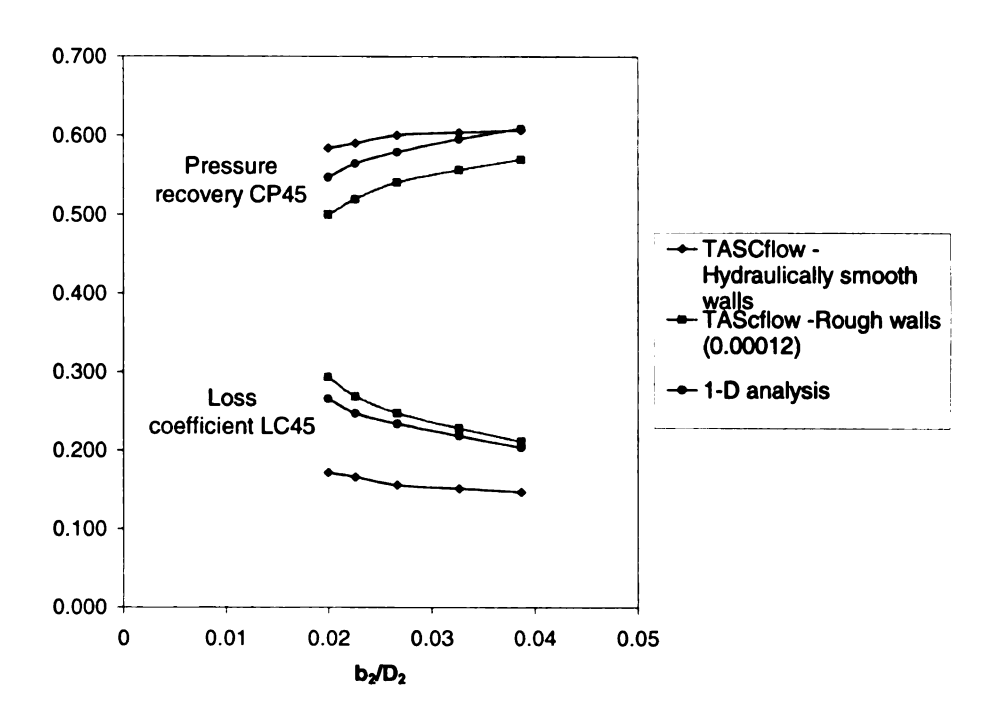


Figure 6.15 Diffuser performance at design point

The TEIS model for each impeller was determined following the method described in section 6.2.3. The models are described in Table 6.5.

**Table 6.5 TEIS models** 

	$\eta_a$	η <sub>b</sub>	$\sigma_2$	DR <sub>stall</sub>
AA50	0.78	0.46	0.853	1.15
AA55	0.78	0.38	0.841	1.13
AA	0.78	0.44	0.846	1.151
AA65	0.78	0.475	0.845	1.17
AA70	0.78	0.52	0.853	1.149

The corresponding performance map for the five impellers is shown in Figure 6.16. The highest efficiency is achieved for the widest impeller (AA70). At the design point, the highest total-to-total pressure ratio is obtained for the impeller with the smallest backsweep angle (AA50). The pressure ratio curves for the AA55, AA60, and AA65 are very similar. Considering the exit flow angle at the rotor exit, the AA60 or the AA65 should give the best compromise between stability, efficiency, and pressure ratio.

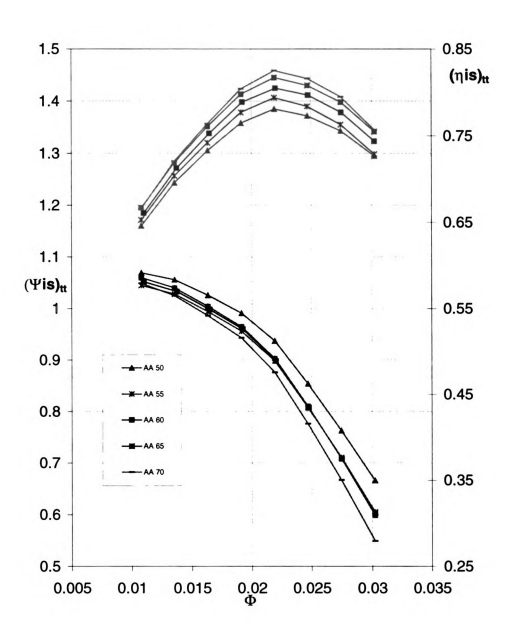


Figure 6.16 Performance prediction comparison

## 6.5. Influence of the Blade Leading Edge

To investigate the effect of blade leading edge position, the AB impeller was selected. Two additional impellers were then designed. A "straight" impeller (ABstraight) where the leading edge at hub and shroud is at the same axial coordinate and a "radial" impeller (ABradial) where the leading edge starts in the radial part of the impeller. The meridional contours and blade angle distributions were adjusted to obtain acceptable and, if possible, similar relative velocity distributions.

The main problem associated with each configuration is of structural concern. For the "straight" impeller, the  $\theta_{ref}$  has to be large to ensure an acceptable rake at exit. The lean angle at inlet then becomes very large because of the small tip-to-hub radius ratio. This may increase the aerodynamic blockage and may not be suitable for stress consideration, the blade having to support the impeller cover. For the radial impeller, the blade length being much smaller, the maximum stress will have to be checked to ensure that the blade can hold the cover.

Table 6.6 TASCflow analysis (smooth walls) – Effect of the leading edge position

	AB	ABstraight	ABradial
$C_{u2}$	377.9	369.3	380.7
C <sub>m2</sub>	139.8	140.4	147.9
$\alpha_2$	69.7	69.2	68.8
$\delta_2$	-7.8	-8.2	-6.7
$P_{02}$	1059.4	1055.2	1054.5
$P_2$	1002.3	1000.4	994.7
$T_{02}$	631.3	630.8	631.6
Π <sub>tt stage</sub>	1.175	1.171	1.171
(η <sub>is</sub> ) <sub>tt stage</sub>	0.883	0.882	0.85

The AB impeller exhibits the best stage performance. The ABstraight and the AB are very similar. The flow in ABstraight is better guided because the blade leading edge

is positioned before the one of the AB, but the additional blade length generates friction losses. In the AB radial, the blade length is much shorter, but the flow is less well guided. Separation took place on the blade, which explains the drop in efficiency.

## 7. CONCLUSIONS AND RECOMMENDATIONS

A one-dimensional and a quasi-three-dimensional program were successfully developed to design a centrifugal impeller. Ten low-flow coefficient compressors were designed and analyzed numerically. Four of them were designed as an extension of an existing family (AA, AB, AC, and AD), and this allowed a study of the influence of flow coefficient on the stage performance. Four other impellers (AA50, AA55, AA65, and AA70) were designed as a variation of the AA impeller: they have a different outlet width-outlet blade angle combinations but are aimed at providing the same stage total-to-total pressure ratio. Finally, two impellers were derived from the AB impeller to study the effect of the blade leading edge position: the AB straight with an axial leading edge and the AB radial with a leading edge located in the radial part of the impeller.

The numerical analysis provided vital information regarding the internal aerodynamics of each impeller. All impellers exhibited a jet/wake flow pattern. The high backsweep angle of the blade was responsible for the rather small extent of the wake area at the design point. The wake was found to extend towards the hub suction side region as the mass flow was reduced for the AA impeller. At the design point, as the flow coefficient was reduced (i.e. narrower impeller), the meridional velocity distribution and the wake pattern in the exit plane were very similar. The wake occupied a larger relative area because of the smaller impeller exit width.

The change in blade angle-blade outlet width showed that the wake was the largest for the impeller with the largest backsweep. Hence, the development of the wake appeared to be controlled more by the curvature in the meridional plane and the diffusion achieved, than by the exit blade angle. Even though the wake was larger in the high-backswept impeller, high performances were obtained because of the larger impeller exit area: the lower velocity levels and the wider diffuser led to a reduction in the total pressure loss.

No advantage was found by using an impeller with a blade whose leading edge is located in the radial part of the impeller. It is possible that a more careful adjustment of the inlet blade angle could have led to similar performance than the AB impeller or the AB impeller with straight leading edge.

The performances of each impeller were estimated by CFD on a stage basis for hydraulically smooth and rough walls. The necessary aero-thermodynamic quantities required to calculate the performance were mass-averaged at the impeller exit and diffuser exit. The numerical results were used to update the one-dimensional model and to generate the predicted performance map of each impeller. It was found that the one-dimensional predictions with no external losses were in very good agreement with the TASCflow analysis with rough walls. The one-dimensional model with internal losses is therefore believed to be capable of predicting the efficiency but it had a tendency to slightly over-predict the pressure ratio. The qualitative trend, nevertheless, was very accurate.

coe

be

of

na

ex

\*\*

re

th de

fl

fı

a

I

U

u

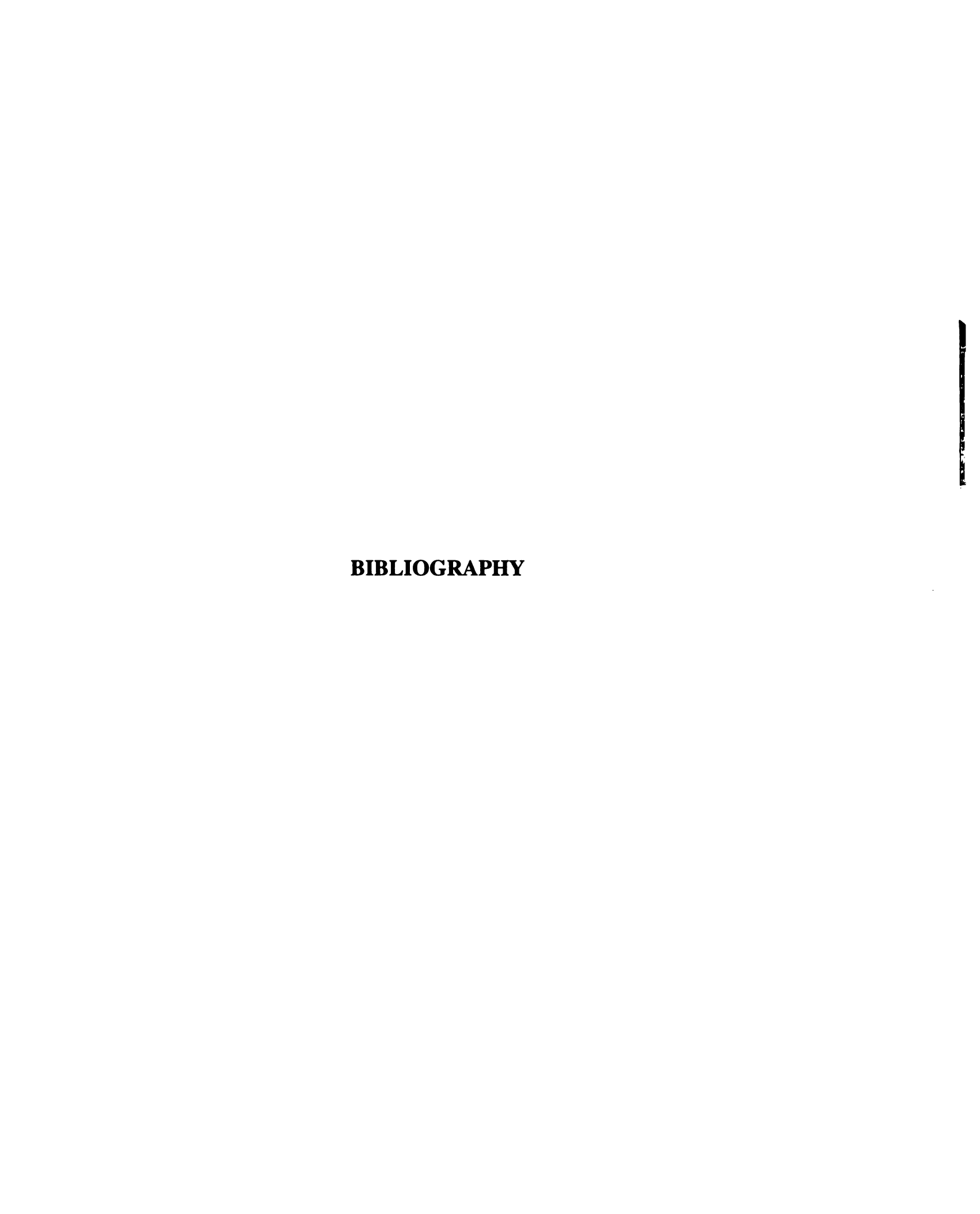
As expected, the performances of the stages were found to decrease as the flow coefficient was reduced. The impellers with 60 and 65 degrees backsweep were found to be a good compromise between efficiency level, pressure ratio, and stability. An increase of the exit blade angle with a wider outlet width would probably be helpful for the narrowest stages (AB, AC, AD).

The performance predictions quoted herein can only be quantified by an experimental testing program of research. Considering the levels of efficiency obtained with the existing family, the predicted levels of efficiency for the stages appear to be reasonable.

As an extension of the work, the back disk and the seals could be included into the CFD model. This would allow a more accurate prediction of the flow field at off-design performance on a qualitative and on a quantitative basis as recirculation of the flow through the seals will be possible. The one-dimensional model would also benefit from such an analysis.

A quantitative CFD analysis at off-design could be performed to validate the assumptions made in the one-dimensional off-design prediction method (constant slip factor, constant secondary flow mass fraction).

Even though more numerical work and experimental work remains to be done, this study has shown that numerical analysis is able to provide qualitative and quantitative information to help improve the design of low-flow coefficient compressors with high efficiency and a large operating range.



#### **BIBLIOGRAPHY**

- Aungier, R., 1995, "Mean Streamline Aerodynamic Performance Analysis of Centrifugal Compressors", J. of Turbomachinery, Vol.117, 1995, pp.360-366
- Balje, O.E., 1981, "Turbomachines a Guide to Design, Selection and Theory", John Wiley & Sons, New York
- Benvenutti, E., 1978, "Aerodynamic Development of Stages for Industrial Centrifugal Compressors. Part 2: Test Data Analysis, Correlation and Use", ASME Paper 78-GT-5
- Bosman, C. and Marsh, H., 1974, "An Improved Method for Calculating the Flow in Turbomachines Including a Consistent Loss Model", J. Mech. Eng. Sci., Vol.16, No.1, pp.25-31
- Casey, M., 1983, "A Computational Geometry for the Blades and Internal Flow Channels of Centrifugal Compressors", J. of Eng. for Power, Vol.105, pp.288-295
- Casey, M. and Roth, P., 1984, "A Streamline Curvature Throughflow Method for Radial Turbocompressors", I.Mech.E. Publications 1984-3, Computational Methods in Turbomachinery, London
- Casey, M. and Roth, P., 1984, "A Streamline Curvature Throughflow Method for Radial Turbocompressors", I.Mech.E. Publications 1984-3, *Computational Methods in Turbomachinery*, London
- Casey, M. and Marty, F., 1986, "Centrifugal Compressors Performance at Design and Off-Design", *Proc. of the Institute of Refrigeration*, London, pp.71-80
- Casey, M.V., Dalbert, P. and Schurter, E., 1990, "Radial Compressor Stages for Low Flow Coefficients", *IMEch. E.*, Den Hague
- Casey, M., Dalbert, P. and Roth, P., "The Use of 3D Viscous Flow Calculations in the Design and Analysis of Industrial Centrifugal Compressors", ASME Paper 90-GT-2

- Cooper, P., Graf, E., Luce, T., 1994, "Computational Fluid Dynamical Analysis of Complex Internal Flows in Centrifugal Pumps", *Proceedings of the Eleventh International Pump Users Symposium*, pp.83-94
- Cumpsty, N.A., 1989, "Compressor Aerodynamics", University of Cambridge, Longman Scientific Technical, UK
- Daily, J.W. and Nece, R.E., 1960, "Chamber Dimension Effects on Induced Flow and Frictional Resistance of Enclosed Rotating Disks", J. of Basic Engineering, pp.217-232
- Dalbert, P., Wiss, D.H., 1995, "Numerical Transonic Flow Field Predictions for NASA Compressor Rotor 37", ASME Paper 95-GT-326
- Dallenbach, F., 1961, "The Aerodynamic Design and Performance of Centrifugal Compressors and Mixed Flow Compressors", Society of Automotive Engineers, *Technical Progress Series*, Vol.3, pp.2-30
- Dean, R.C. and Senoo, Y., 1960, "Rotating Wakes in Vaneless Diffusers", J. of Basic Engineering, Sept. 1960, pp. 563-574
- Dean R.C., Jr., 1974, "The Fluid Dynamics Design of Advanced Centrifugal Compressors", Lecture notes, presented March 25-29, 1974 at the Von Karman Institute, Brussels, Belgium
- Denton, J.D., 1978, "Throughflow Calculations for Transonic Axial Flow Turbines", J. of Eng. for Power, April 1978, Vol. 100, pp. 212-218
- Di Liberti, J.-L. and Engeda, A., 1996, "Low-Flow Coefficient Compressors, Phase I: Literature Survey", *Contract report*, February 1996
- Di Liberti, J.-L., Engeda, A., Flathers, M., 1996, "Low-Flow Coefficient Compressors: Phase II: Preliminary Design of Four Low Flow Coefficient Compressors", Contract report, December 1996
- Di Liberti, J.-L., 1997, "Validation of the new pre-/post- processor of TASCflow for impeller analysis", Gas Compressor Engineering Report GCER, Solar Turbines
- Eckardt, D., 1976, "Detailed Flow Investigations Within a High-Speed Centrifugal Compressor Impeller", J. of Fluids Eng., Sept. 1976, pp.390-402
- Eckardt, D, 1980, "Flow Field Analysis of Radial Backswept Centrifugal Compressor Impellers Part 1: Flow Measurement Using Laser Velocimeter", In Performance Prediction of Centrifugal Pump and Compressors, ASME Fluid Conference.

- Farge T. and Johnson, M., 1990, "The Effect of Backswept Blading on the Flow in a Centrifugal Compressor Impeller", ASME Paper 90-GT-231
- Flathers, M., and Bache, G., 1996, "Aerodynamically Induced Radial Forces in a Centrifugal Gas Compressor Part 2: Computational Investigation", ASME Paper 96-GT-352
- Galvas, M. R., 1973, "Fortran Program for Predicting Off-Design Performance of Centrifugal Compressors", NASA TN D-7487
- Hathaway, M.D., Chriss, R.M., Wood, J.R. and A.J. Strazsiar, A.J., 1992, "Experimental and Computational Investigation of the NASA Low-Speed Centrifugal Compressor Flow Field", ASME Paper 92-GT-213
- Howard, J.H., Ashrafizaadeh, M., 1994, "A Numerical Investigation of Blade Lean Angle Effects on Flow in a Centrifugal Impeller", ASME Paper 94-GT-149
- Jansen, W. and Kirschner, A., 1967, "Impeller Blade Design Method for Centrifugal Compressors", *Proceedings of symposium on Fluid Mechanics, Acoustics and Design of Turbomachinery* at Penn State University, NASA SP-304, Vol.2, pp.537-563
- Japikse, D., 1984, "A Critical Evaluation of Stall Concepts for Centrifugal Compressors and Pumps Studies in Component Performance, Part 7", Presented at ASME Winter Meeting, New Orleans
- Japikse, D., 1985, "Assessment of Single- and Two-Zone Modeling of Centrifugal Compressors Studies in Component Performance: Part 3", ASME Paper 85-GT-73
- Johnson, M.W., 1978, "Secondary Flow in Rotating Bends", J. of Eng. for Power, Oct. 1978, Vol. 100, pp.553-560
- Johnson, M.W. and Moore, J., 1983, "The Influence of Flow Rate on the Wake in a Centrifugal Impeller", J. of Eng. For Power, Vol.105, pp.33-39
- Johnston, J.P. and Dean, R., 1966, "Losses in Vaneless Diffuser of Centrifugal Compressor and Pumps: Analysis, Experiment, and Design", J. of Eng. for Power, January 1966, pp.49-62
- Johnston, J.P. and Eide, S.A., 1976, "Turbulent Boundary Layer on Centrifugal Compressor Blades: Prediction of the Effects of Surface Curvature and Rotation", J. of Fluids Eng., pp.374-381
- Katsanis, T., 1964, "Use of Arbitrary Quasi-Orthogonals for Calculating Flow Distribution in the Meridional Plane of a Turbomachine", NASA TN-2546

- Koizumi, T., 1983, "Experimental Studies on Performance of Centrifugal Compressors with Very Small Flow Coefficient", *Mitsui Sozen Technical Review* 117, pp.28-39
- Krain, H., 1984, "Experimental Observation of the Flow in Impellers and Diffusers", VKI LS 1984-07
- Krain, H., 1988, "Swirling Impeller Flow", J. of Turbomachinery, Vol.110, Jan.1988, pp.122-128
- Lakshminarayana, B., 1996, "Fluid Dynamics and Heat Transfer of Turbomachinery", John Wiley & Sons, Inc.
- Lieblein, S., 1965, "Experimental Flow in Two-Dimensional Cascades", in "Aerodynamic Design of Axial-Flow Compressors", NASA SP-36, pp.183-226
- Marsh, H., 1971, "The Uniqueness of Turbomachinery Flow Calculations Using the Streamline Curvature and Matrix Through-Flow Methods", J. of Mech. Eng. Science, Vol.13, No6, pp.376-379
- Paroubek, J. et al., 1994, "Experimental Investigation and Performance Analysis of 6 Low Flow Coefficient Centrifugal Compressor Stages", ASME Paper 94-GT-43
- Pinarbasi, A. and Johnson, M.W., 1994, "Detailed Flow Measurements in a Centrifugal Compressor Vaneless Diffuser", *Journal of Turbomachinery*, Vol.116, pp.453-461
- Raithby, G. D., 1976, "Skew Upstream Differencing Schemes for Problems Involving Fluid Flow", Comp. Meth. Appl. Mech. Eng., Vol.9, pp.153-164
- Rodgers, C., 1964, "Typical Performance Characteristics of Gas Turbine Radial Compressors", J. of Eng. for Power, April 1964, pp.161-175
- Rodgers, C., 1980, "Efficiency of Centrifugal Compressor Impellers" AGARD CP 282, 7-9 may 1980
- Rusak, V., 1974, "Low Specific Speed Compressor", United States Patent 37888765, Jan.29, 1974, Inventor: Vasil Rusak, Assigned: Delaval Turbine Inc., Trenton, N.J., Filed: Nov.18, 1971
- Sapiro, L., 1995, "Centrifugal compressors Aerothermodynamic concepts for selection and performance evaluation", Internal note, Solar Turbines Inc., 1995
- Schlichting, H., 1979, "Boundary-Layer Theory", 7<sup>th</sup> ed., McGraw-Hill, New York

- Senoo, Y. and Kinoshita, Y., 1978, "Limits of Rotating Stall and Stall in Vaneless Diffuser of Centrifugal Compressors", ASME Paper 78-GT-19
- Stanitz, J.D. and Prian, V.D., 1951, "A Rapid Approximate Method for Determining Velocity Distribution on Impeller Blades of Centrifugal Compressor", NASA TN 2421
- Van den Braembussche, R., 1984, "Surge and Stall in Centrifugal Compressors" in VKI Lecture Series 1984-07, "Flow in Centrifugal Compressors"
- Van den Braembussche, R., 1985, "Description of Secondary Flows in Radial Flow Machines", in "Thermodynamics and Fluid Mechanics of Turbomachinery", Edited by A.S. Ucer, P. Stow and C. Hirsch, Martinus Nijhoff Publishers, pp. 665-684
- Van den Braembussche, R., 1987, "Centrifugal Compressors One Dimensional Design", VKI CN 134, May 1987
- Van den Braembussche, R., 1990, "Design and Optimization of Centrifugal Compressors", VKI CN 141, Oct. 1990
- Van Doormaal, J.P. and Raithby, G.D., 1987, "The Segregated Approach to Predicting Viscous Compressible Fluid Flows", J. of Turbomachinery, Vol.109, pp.268-277
- Wiesner, F., 1967, "A Review of Slip Factors for Centrifugal Compressors", J. of Eng. for Power, Oct. 1967, pp.558-572
- Wilson, D.G., 1984, "The Design and Efficiency of High Efficiency Turbomachinery and Gas Turbines", MIT Press
- Wennerstom, A.J., 1974, "On the treatment of Body Forces in the Radial Equilibrium Equation of Turbomachinery", *Traupel-Festschrift*, Juris-Verlag, Zurich, pp.351-367
  - White, F. M., 1991, "Viscous Fluid Flow", 2<sup>nd</sup> Edition, McGraw-Hill, New York
- Wilkinson, D., 1970, "Stability, Convergence, and Accuracy of Two-Dimensional Streamline Curvature Methods Using Quasi-Orthogonals", *Proc. Inst. Mech. E.*, 1969-70, Vol.184, Pt3G, Paper 35, pp.108-119

**APPENDICES** 

APPENDIX A

## Appendix A

The energy equation in rotating passages for inviscid flow is expressed by the conservation of rothalpy as follows:

$$dh_{t,rel} = \frac{dp}{\rho} + d\left(\frac{w^2}{2}\right) - d\left(\frac{u^2}{2}\right) = 0$$
 (A. 1)

Taking the derivative with respect to the n-direction of

$$w\frac{\partial w}{\partial n} - u\frac{\partial u}{\partial n} = -\frac{1}{\rho}\frac{\partial p}{\partial n}$$
 (A. 2)

The derivative with respect to the n-direction of the peripheral speed is given by

$$\frac{\partial u}{\partial n} = \omega \frac{\partial r}{\partial n} = \omega \cos \beta \tag{A. 3}$$

Plugging Eq.(A.3) into to Eq.(A.2), gives

$$w\frac{\partial w}{\partial n} - \omega u \cos \beta = -\frac{1}{\rho} \frac{\partial p}{\partial n}$$

The equation of motion on the n-direction is given by

$$-\frac{w^2}{R_n} + 2\omega w - \omega u \cos \beta = \frac{1}{\rho} \frac{\partial p}{\partial n}$$

Combining the Eq.A.4 and Eq.A.5 leads to

$$\frac{\partial w}{\partial n} = 2\omega - \frac{w}{R_n}$$

This equation can be approximately integrated along the n-direction to give

$$w_{ss} - w_{ps} = \left(2\omega - \frac{w_{mean}}{R_n}\right) \Delta n$$



# Appendix B

# One-dimensional analysis of centrifugal compressors

## **B.1 Inputs**

### **B.1.1 Geometrical**

The one-dimensional geometry as shown in Figure 3.15 must be known. This includes inducer hub and tip diameter, exit width and exit diameter, and inlet and exit blade angles at hub and shroud.

## **B.1.2** Aero-thermodynamic parameters

The operating point is given (mass-flow rate, rotational speed) and the inlet total pressure and temperature are known.

If the inlet flow is coming from a previous stage, the distortion of the inlet velocity profile is specified by the parameter Cm<sub>shroud</sub>/Cm<sub>mean</sub>. An inlet boundary layer

blockage is also introduced to take into account the development of the boundary layer between the inlet and the leading edge of the impeller. Any residual swirl must be indicated.

## **B.2 General equations**

In a one-dimensional procedure, the following relations are used:

the equation of state

$$P = \rho RT$$

• the Mach number definition

$$M = \frac{C}{\sqrt{\gamma RT}}$$

• the isentropic relations between total and static pressures and temperatures

$$T = T_0 - \frac{C^2}{2C_p}$$

$$P = P_0 \left( 1 + \frac{\gamma - 1}{2} M^2 \right)^{\frac{\gamma}{\gamma - 1}}$$

• the continuity equation

$$\dot{m} = A \rho_{st} C_m$$

which can be expressed in terms of Mach number and inlet total pressure and temperature

$$\frac{\dot{m}\sqrt{T_0}}{A_{eff} p_0} = \sqrt{\frac{\gamma}{R}} M \left(1 + \frac{\gamma - 1}{2} M^2\right)^{\frac{\gamma + 1}{2(\gamma - 1)}}$$

A<sub>eff</sub> is the area normal to the incoming velocity C.

• the geometrical relations in the velocity triangle (Figure 2.3 of Chapter 2).

#### **B.2.1 Inducer**

The continuity equation allows solving for the Mach number at mean diameter. From the isentropic relations, the static pressure and temperature are calculated. All velocities and thermodynamic quantities can then be evaluated.

The conditions at hub and at shroud are evaluated through the assumed Cm<sub>shroud</sub>/Cm<sub>mean</sub> ratio. The incidence at hub, mean, and shroud can then be calculated. The blade thickness is not taken into account.

#### **B.2.2 Impeller exit condition**

The program uses the two-zone model proposed by Japikse (1985). It is then assumed that the flow near the impeller exit is made of two regions called the primary and secondary zones and is equivalent to the jet and wake as described in Chapter 3.

The obtained system of equations contains more unknowns than equations. A closure is obtained by assuming

• the primary zone deviation or the slip factor

- the diffusion level MR2
- the ratio between the mass-flow in the secondary zone and the total mass-flow  $\chi$

The relations for calculating the conditions in the primary zone, in the secondary zone, and for mixed-out conditions will now be given for a perfect gas. They are presented the way they have been implemented.

## **B.2.2.1 Relations for the primary zone**

The Mach number at inducer tip Mw1t has been calculated in the inducer section, and the MR2 value is obtained from the MR2 vs. MR2I proposed by Dean.

$$Mw_{2p} = \frac{Mw_{1t}}{MR_2}$$
 Definition of MR2

$$I_{01} = c_p T_{1t} + \frac{W_{1t}^2}{2} - \frac{U_{1t}^2}{2}$$
 Inlet rothalpy

$$T_{2p} = \frac{I_{01} + \frac{U_2^2}{2}}{c_p + \gamma R M w_{2p}^2}$$
 Conservation of rothalpy

$$P_{2p} = P_{1t} \left( \frac{T_{2p}}{T_{1t}} \right)^{\frac{\gamma}{\gamma-1}}$$
 primary zone is isentropic

$$\rho_{2p} = \frac{P_{2p}}{RT_{2p}}$$

$$W_{2p} = Mw_{2p} \sqrt{\gamma R T_{2p}}$$

$$\beta_{2n} = \beta_{2n} + \delta_{2n}$$

$$Cm_{2p} = W_{2p} \cos \beta_{2p}$$

$$Cu_{2p} = U_2 + W_{2p} \sin \beta_{2p}$$

$$C_{2p} = \sqrt{Cm_{2p}^2 + Cu_{2p}^2}$$

$$\alpha_{2p} = a \tan \left( \frac{Cu_{2p}}{Cm_{2m}} \right)$$

$$T_{02p} = T_{2p} + \frac{C_{2p}^2}{2c_p}$$

$$\varepsilon = 1 - \frac{\dot{m}(1-\chi)}{\rho_{2p}W_{2p}A_{exit}\cos\beta_{2p}}$$
 (\varepsilon\ is the area ratio between the secondary zone and

must be greater than 0.1)

## **B.2.2.2** Relation for the secondary zone

The assumptions for the secondary zone are:

- The secondary zone follows the blade  $\delta_{2s}=0$
- The static pressure in the primary and in the secondary zone are equals

A correlation must be introduced to evaluate the power dissipated by the friction in the front cover.

The relations used are now given.

$$p_{2s} = p_{2p}$$

$$\beta_{2s} = \beta_{2bl} + \delta_{2s}$$

$$I_{02s} = I_{01} + P_{front \, \text{cov} \, er}$$

The set of following equations is solved by iterations where  $\rho_{2s}$ ,  $Cm_{2s}$ ,  $T_{2s}$ , and  $W_{2s}$  are the unknowns:

$$\rho_{2s} = \frac{P_{2s}}{RT_{2s}}$$

$$(1-\chi)\rho_{2p}Cm_{2p} + \chi\rho_{2s}Cm_{2s} = \frac{\dot{m}}{A_{out}}$$

$$W_{2s} = \frac{Cm_{2s}}{\cos\beta_{2s}}$$

$$I_{02s} = c_p T_{2s} + \frac{W_{2s}^2}{2} - \frac{U_2^2}{2}$$

The complete velocity triangles are calculated by

$$Cu_{2s} = U_2 + Cm_{2s} \tan \beta_{2s}$$

$$C_{2s} = \sqrt{Cu_{2s}^2 + Cm_{2s}^2}$$

All the remaining thermodynamics quantities in the secondary zone  $M_{2s}$ ,  $T0_{2s}$ ,  $P0_{2s}$  are calculated.

## **B.2.2.3 Mixed-out conditions**

Solve by iterations on  $\rho_{2m}$  the following set of equations:

$$Cm_{2m} = \frac{\dot{m}}{2\pi r_2 b_2 \rho_{2m}}$$

$$P_{2m} = \frac{\chi Cm_{2p} + (1 - \chi)Cm_{2s} - Cm_{2m}}{2\pi r_2 b_2 \dot{m}} + P_{2p}$$

$$T_{2m} = T_{02m} - \frac{Cm_{2m}^2 + Cu_{2m}^2}{2c_p}$$

$$\rho_{2m} = \frac{P_{2m}}{RT_{2m}}$$

Then all the remaining velocities and thermodynamics quantities are calculated at state 2m, especially:

$$\alpha_{2m} = a \tan \left( \frac{Cu_{2m}}{Cm_{2m}} \right)$$

$$\beta_{2m} = -a\cos\left(\frac{Cm_{2m}}{W_{2m}}\right)$$

$$\delta_{2m} = \beta_{2m} - \beta_{2h}$$

And the slip factor:

$$\sigma = 1 - \frac{C_{slip}}{U_2} = \frac{Cu_{2m} - Cm_{2m} \tan \beta_{2b}}{U_2}$$

If the slip factor was input, then a new deviation is specified, and the calculation iterated.

## **B.3.4 Off-design conditions**

The effectiveness of the impeller inlet portion  $\eta_a$  and of the passage portion  $\eta_b$ , and the maximum diffusion DR<sub>stall</sub> are given.

$$Cp_{a,i} = 1 - \left(\frac{\cos \beta_1}{\cos \beta_{1b}}\right)^2$$

$$Cp_{b,i} = 1 - \frac{1}{AR_b^2} = 1 - \left(\frac{A_{th}}{A_e}\right)^2$$

$$Cp_a = \eta_a Cp_{a,i}$$

$$Cp_b = \eta_b Cp_{bi}$$

$$DR_2 = \frac{1}{1 - \eta_a C p_{ai}} \frac{1}{1 - \eta_b C p_{bi}}$$

If DR<sub>2</sub>>DR<sub>stall</sub>, then DR<sub>2</sub>=DR<sub>stall</sub>

$$W_{2p} = \frac{W_{1t}}{DR_2}$$

#### **B.3.5 Vaneless diffuser analysis**

Following the meanstreamline analysis of Johnston and Dean (1966), the flow entering the diffuser is assumed to be steady, uniform, and axisymmetric. All thermodynamic quantities depend only on the meridional coordinate m. An apparent wall friction is introduced to provide a loss in total pressure. It is assumed that the wall friction is directed along the local velocity and proportional to the local dynamic head  $\rho \frac{C^2}{2}$ . The corresponding governing equations for the flow in a vaneless diffuser are:

Conservation of mass

$$\dot{m} = 2\pi b r \rho C_m = const$$

Conservation of angular momentum

$$\rho b C_m \frac{d(rC_u)}{dm} = -rC_f \rho C C_u$$

Conservation of linear momentum

$$-\frac{dP}{dm} - C_f \rho \frac{CC_m}{b} = \rho C_m \frac{dC_m}{dm} - \rho \sin \alpha \frac{C_u^2}{r}$$

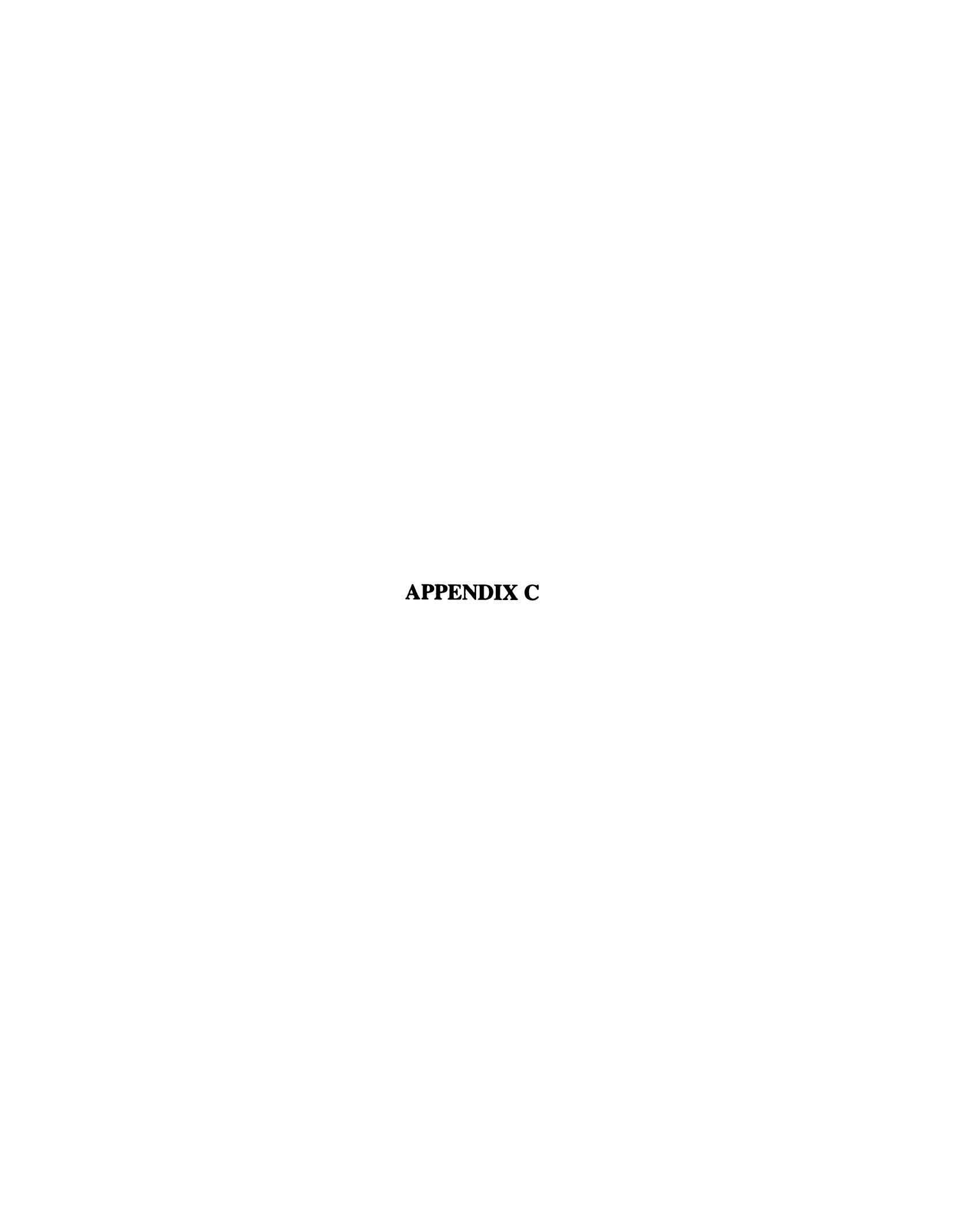
Equation of state

$$P = \rho RT$$

Energy equation

$$h + \frac{C^2}{2} = \frac{\gamma}{\gamma - 1} \frac{P}{\rho} + \frac{1}{2} (C_m^2 + C_u^2) = h_0 = const$$

The flow is assumed to be uniform in both axial and circumferential direction. By differentiating and combining these four relations, one can solve numerically for  $\rho$ ,  $C_m$ ,  $C_u$ , P and T along the diffuser meanstreamline. A finite-difference method using a fixed increment  $\Delta m$  along the meridional direction has been used in the code.



# Appendix C

## Streamline curvature throughflow method

#### C.1 Model

## **C.1.1 General equations**

The equation of motion in the relative frame for an axisymmetric isentropic flow with no body force was given in Chapter 3. The flow would in fact be axisymmetric only if an infinite number of blades were used. The force acting between the fluid and the blade are added to the equation of motion as a body force field  $\vec{F}$ .

The equation in the absolute frame of reference is

$$\frac{D\vec{C}}{Dt} = -\frac{\vec{\nabla}p}{\rho} + \vec{F}$$

Using the coordinate system shown in Figure C1, the equations of motion become (Wennerstrom 1974):

Streamline direction

$$C_m \frac{\partial C_m}{\partial m} - \frac{C_u^2}{r} \sin \varepsilon = -\frac{1}{\rho} \frac{\partial p}{\partial m} + F_m$$

Streamsurface direction

$$\frac{C_m^2}{r_c} - \frac{C_u^2}{r} \cos \varepsilon = -\frac{1}{\rho} \frac{\partial p}{\partial n} + F_n$$

Circumferential direction

$$\frac{C_m}{r}\frac{\partial (rC_u)}{\partial m}=F_u$$

The notations of Figure C.1 are used.

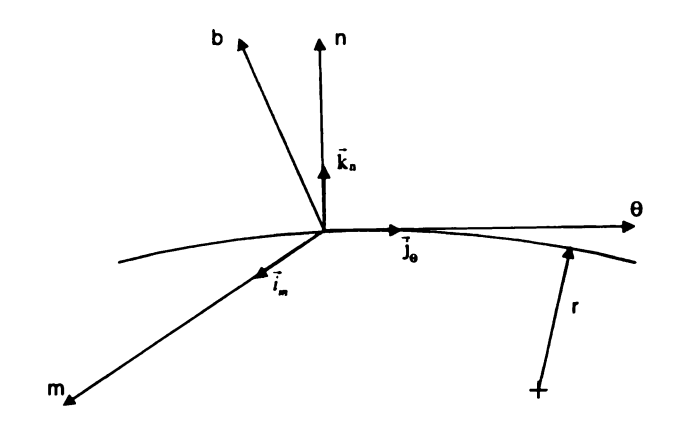


Figure C.1 Coordinate system for the general equations

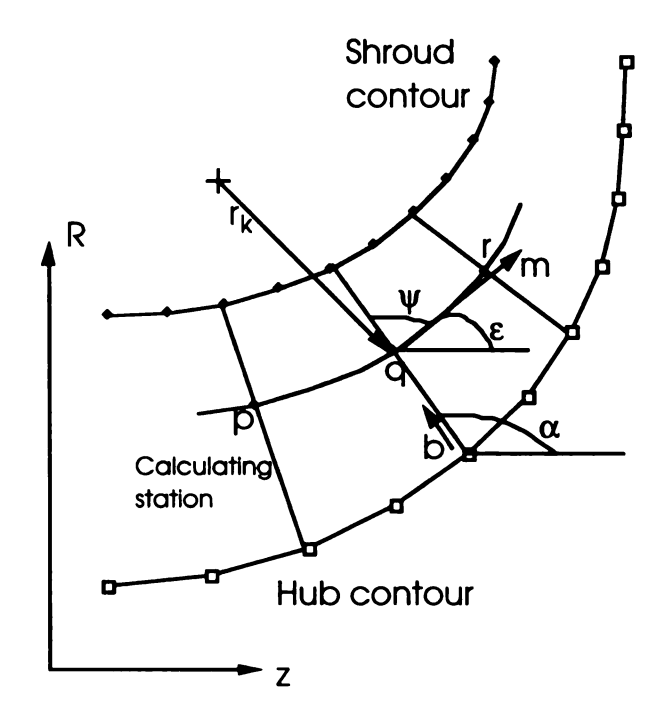


Figure C.2 Definition of the geometry and notations

The derivation of the body forces in the meridional plane has been done by Wennerstom (1974). Introducing the energy equation, the enthalpy-entropy relation, the relation between stationary and rotating frame, and after rearrangement, Equation (C.1) is obtained in which  $C_m$  is the unknown. The notations of Casey (1984) are used hereafter.

$$C_{m} \frac{dC_{m}}{db} = RET + SCT + BFT + DFT$$
 (C.1)

where:

• RET stands for simple radial equilibrium:

$$RET = \frac{dh_0}{db} - T\frac{dS}{db} - \frac{1}{2r^2}\frac{d}{db}(rC_u)^2$$

• SCT represents the streamline curvature and convective acceleration terms:

$$SCT = \frac{C_m^2}{r_c} \sin \psi + C_m \frac{dC_m}{dm} \cos \psi$$

• BFT are the blade force terms, given by

BFT = 
$$\frac{C_m}{r} \tan \gamma \frac{d}{dm} (rC_u)$$
 in the bladed region

and by

## BFT=0 in the bladeless regions

• DFT represents the dissipation force terms given by

DFT = 
$$(\cos \psi \cos^2 \beta + \tan \gamma \sin \beta \cos \beta)$$
T  $\frac{ds}{dm}$  in the bladed region

and by

DFT = 
$$\cos \psi T \frac{ds}{dm}$$
 in the bladeless region.

## **C.1.2** Continuity equation

The integrated mass flow rate along a station is given by

$$\dot{m} = \int (2\pi r - Z\delta) \rho C_m \sin \psi \, db$$

where C<sub>m</sub>sin $\psi$  represents the velocity normal to the quasi-orthogonal.

A quasi-orthogonal has been defined by Katsanis (1964) as "any curve that intersects every streamline between the flow boundaries exactly once, as does an orthogonal to any streamline." The quasi-orthogonal (Q.O.) are not perpendicular to the streamline. They are fixed at the beginning of the calculation and remain unchanged regardless of any change in the streamline position.

## **C.1.3 Additional equations**

## C.1.3.1 Angular momentum

The angular momentum is calculated by assuming that the flow follows the blade.

$$(rC_u)_q = (rC_m \tan \beta_{bl} + \omega r^2)_q$$

In reality, the flow does not follow the blade at inlet due to incidence level and at exit due to slip. The following modified equation proposed by Casey et al. (1984) is used:

$$(rC_u)_q = \gamma_i (rC_u)_i + \gamma_o (rC_u)_o + (1 - \gamma_i)(1 - \gamma_o)(rC_m \tan \beta_{bl} + \omega r^2)_q$$

 $(rC_u)_i$  represents the inlet momentum due for example to prewhirl.  $(rC_u)_o$  represents the exit momentum that can be calculated once a slip factor is assumed.  $\gamma_i$  is a parabolic function varying between 1 at the leading edge and 0 at a quarter of the meridional length. Similarly,  $\gamma_o$  is a parabolic function varying between 0 at three-quarter of the meridional length and 1 at the trailing edge. These functions allow the angular momentum to vary smoothly between inlet and exit.

## C.1.3.2 Enthalpy change

The change of enthalpy along a streamline between two points p and q is calculated using the conservation of enthalpy along a streamline.

$$(h_0)_q = (h_0)_p$$

In a rotating component, it is the rothalpy I which is conserved

$$I=h_0-\omega rC_u$$

The following equation can be used in all cases, with  $\omega=0$  for stationary elements:

$$(h_0)_q = (h_0)_p + \omega [(rC_u)_q - (rC_u)_p]$$

The angular momentum is calculating as mentioned in C1.3.1.

#### C.1.3.3 Loss models

The program offers to deal with isentropic flow or to introduce a loss model. An entropy change and an angular momentum variation due to friction are used along the streamline in order to obtain a more realistic prediction of the flow field. The two relations used to calculate the change in entropy and the change in momentum are due to Traupel and Eckert and Schnell

$$dS = C_d \frac{2}{D_h} \frac{W^3}{T C_m} dm$$

and

$$d(rC_u) = C_f \frac{2W}{D_h} \frac{C_u}{C_m} rdm$$

## **C.1.3.4 Density calculation**

The density is calculated as a function of the enthalpy and the entropy by the relation proposed by Marsh (1971)

$$\frac{\rho}{\rho_0} = \left[ \frac{h_{0i} - \frac{C_u}{2} - \frac{C_m^2}{2}}{h_{0i}} \right]^{\frac{1}{\gamma - 1}} e^{\frac{s - s_{0i}}{R}}$$

For rotating parts

$$\frac{\rho}{\rho_{0i}} = \left[ \frac{I + \frac{\omega^2 r^2}{2} - \frac{C_m^2}{2} (1 + \tan^2 \beta)}{h_{0i}} \right]^{\frac{1}{\gamma - 1}} e^{-\frac{s - s_{0i}}{R}}$$

In these two relations,  $\rho_{0i}$  and  $h_{0i}$  represent the total density and the total enthalpy at inlet.

## C.2 Representation of the impeller meridional contour

The hub and shroud contours of the impeller in the meridional contour are defined by means of Bezier curves. A Bezier curve is a parametric representation of a curve in space. A set of N+1 points (called polygon points) are required to construct a Bezier curve of degree N. Only the first and the last points effectively lie on the curve. For example, the expression defining a second -order Bezier curve is

$$\overrightarrow{OM} = (1-u)^2 \overrightarrow{OP}_1 + 2u(1-u)\overrightarrow{OP}_2 + u^2 \overrightarrow{OP}_3$$

where O is the origin of the coordinate system, M is a point on the curve, P1, P2, P3 are the polygon points, and u is a parameter varying between 0 and 1 along the curve. For u=0, M=P1; and for u=1, M=P3. The corresponding curve is shown in Figure C3.

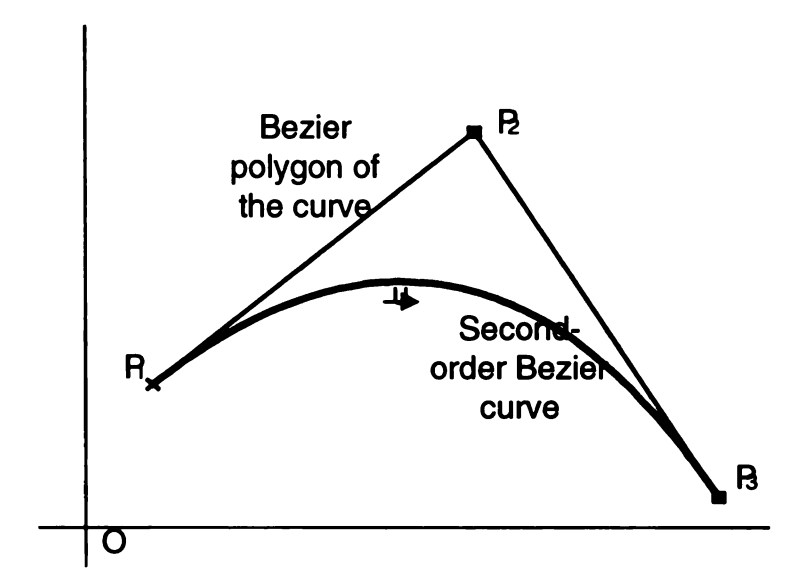


Figure C3. Example of Bezier curve

The point P2 does not lie on the curve, but the tangents at P1 and P3 are in the direction of P2.

The general expression for a Bezier curve of degree N is

$$\overrightarrow{OM} = \sum_{k=1}^{N+1} B_k^N(u) \overrightarrow{OP}$$

with 
$$B_k^N(u) = {N \choose k-1} u^{k-1} (1-u)^{N-k+1} = \frac{N(N-1)...(N-k+2)}{(k-1)!} u^{k-1} (1-u)^{N-k+1}$$

Any Bezier curve can be used in the program provided that the polygon points defining it are given.

## **C.2.1 First guess of the streamlines**

The number of streamlines and stations is chosen by the user. As a compromise between accuracy and time calculation, 8 streamlines and 15 stations are chosen.

When the hub and shroud contours are defined, the quasi-orthogonals can be constructed by varying linearly the parameters u on the hub and shroud curves and joining the corresponding points.

The position of the streamlines for the first iteration is obtained by dividing the length of each quasi-orthogonal by the number of streamlines. The corresponding points on each Q.O. are then joined together to form a first guess of the streamline. An example of the corresponding calculation grid is given in Figure C4.

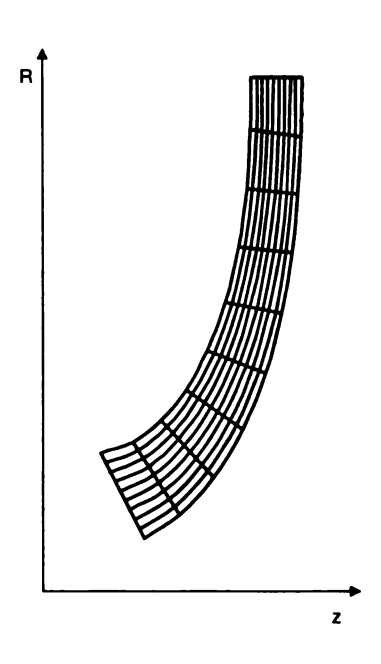


Figure C4. Example of calculation grid

## C.2.2 Slope and radius of curvature

In order to solve the equation of motion, the slope and radius of curvature have to be known at each point. A finite-difference method based on three points does not give a good estimation of the radius of curvature, especially if the slope of the curve is higher than 1 (Katsanis 1964).

In order to solve the problem, a local coordinate system is defined at each station.

The new coordinate system is defined in Figure C5.

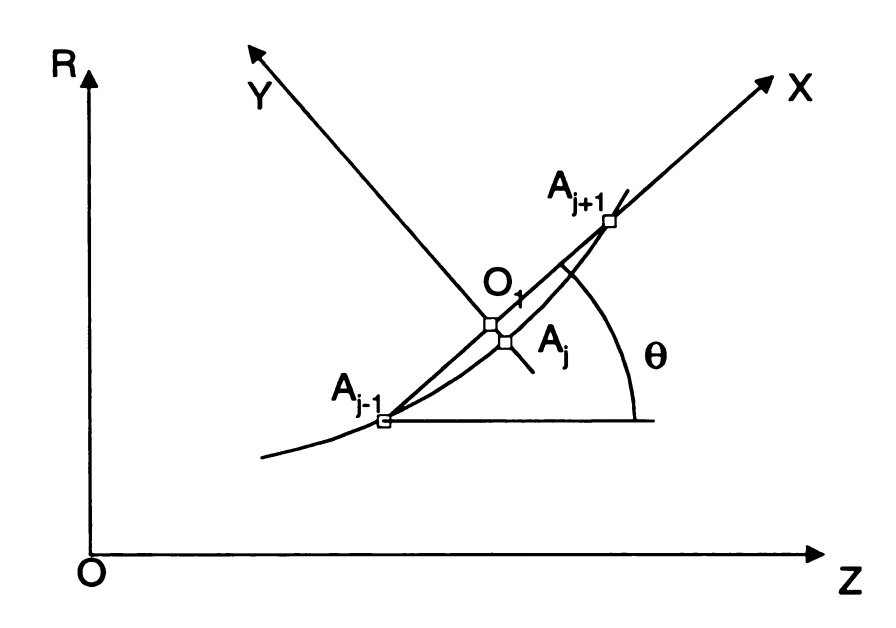


Figure C5. Local coordinate system

To calculate the slope and the radius of curvature at  $A_j$ , a parabola passing through  $A_{j-1}$ ,  $A_j$ ,  $A_{j+1}$  is constructed which has the following characteristics:

- $\bullet f(X_{o_1}) = Y_{A_j}$
- $f(Y_{A_{i+1}}) = 0$

where  $Y=f(X)=aX^2+bX+c$  and (X,Y) are the coordinates in the local coordinate system.

The slope at A<sub>i</sub> is then given by

$$\tan \varepsilon = \left(\frac{dY}{dX}\right)_{X=0} = b$$

and the radius of curvature by

$$Rc = \frac{\left(1 + \left(\frac{df}{dx}\right)_{X=0}^{2}\right)^{1.5}}{\left(\frac{d^{2}f}{dx^{2}}\right)_{X=0}} = \frac{\left(1 + b^{2}\right)^{1.5}}{2a}$$

This method gives a good estimation of the radius of curvature. The values of the radius of curvature calculated analytically on the hub and shroud contour and the ones obtained by the approximated method have been compared. The difference is less than one thousandth. At the end points, this method is less accurate and can be in error by 10% to 20%.

## C.2.3 Blade angle and blade thickness distribution

The blade angle is defined by a third-order polynomial in  $m/m_T$  where m represents the meridional distance along the hub (or the shroud) and  $m_T$  the total length of the meridional hub (or shroud) contour. A typical blade angle distribution is shown in Figure 4.4.

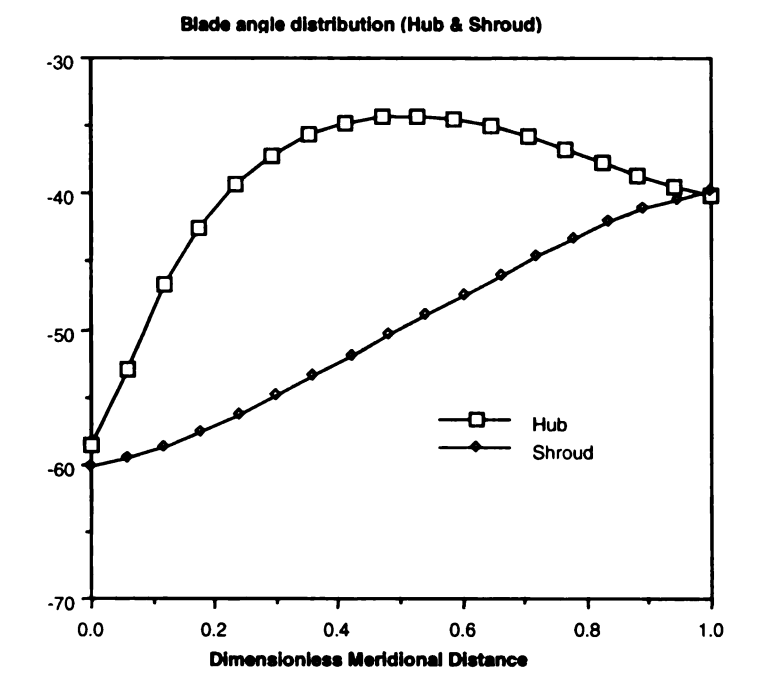


Figure C6. Typical blade angle variation

Similarly, the blade thickness at hub and shroud are defined by means of thirdorder polynomial.

## **C.3 Method of solution**

The momentum equation is first solved using a second-order Runge-Kutta scheme as proposed by Katsanis (1964). Considering the equation  $\frac{dC_m}{dm} = f(C_m, b)$ ,

Cm at the (j+1)st streamline can be estimated by

$$\begin{cases} Cm_{j+1}^* = Cm_j + \left(\frac{dCm}{dm}\right)_j \Delta m \\ Cm_{j+1}^{**} = Cm_j + \left(\frac{dCm}{dm}\right)_{j+1} \Delta m \\ Cm_{j+1} = \frac{Cm_{j+1}^* + Cm_{j+1}^{**}}{2} \end{cases}$$

The continuity equation is then integrated along a quasi-orthogonal using a spline fit curve (piece-wise cubic interpolation). As shown by Marsh (1971), the "family of velocity profile obtained by solving [the momentum equation] cannot intersect". Assuming a value of the velocity at the hub, the momentum equation is solved along the Q.O. The corresponding mass flow rate through the Q.O. can then be evaluated with the continuity equation. If the calculated mass flow is different from the input mass flow, the assumed velocity at the hub is modified accordingly until convergence is reached. The procedure is repeated for all the Q.O. Once the meridional velocity has been calculated, the position of the streamlines is updated until convergence.

Once convergence has been reached at each station, the positions of each streamline can be updated. To avoid over-correction, only a fraction of the new solution is used, leading to the following relation:

$$y_{new} = y_{old} + f * (y_{calc} - y_{old})$$

where f is a damping factor (e.g.0.1).

The slope and radius of curvature is updated together with the enthalpy, angular momentum and velocity gradients. The calculations can then be repeated until convergence is reached on the streamline positions.

The flow in the blade-to-blade plane can also be quickly evaluated from

$$\frac{dW}{d\theta} = \frac{C_m}{W} \frac{d(rC_u)}{dm}$$

and the assumption that the relative velocity varies linearly in the blade to blade direction (Stanitz and Prian 1951).



#### Appendix D

# Estimation of the Inlet Blockage and of the Hub-to-Shroud Velocity Variation

The AA impeller was analyzed with a radial inlet. The inlet boundary condition (pressure, temperature, velocity direction,  $\epsilon$ , TKE) was derived from the return vane analysis of the A1 return system. The meridional velocity profile from the hub to the shroud in front of the leading edge is shown in Figure D.1.

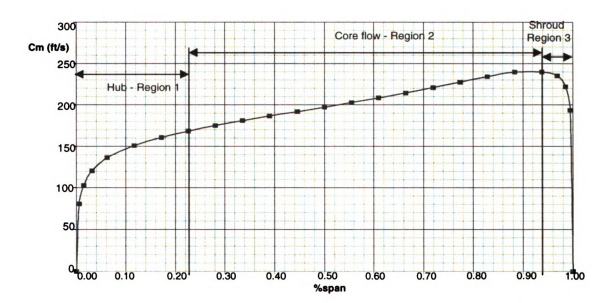


Figure D.1 Meridional velocity profile at impeller inlet (radial inlet)

The velocity profile in Region 1 and 3 can be represented by the following curve fit:

In region 1, Cm=227.6  $x^{0.914}$  (correlation:  $R^2$ =0.994)

In region 3, Cm= $313.03x^{0.0877}$  (correlation:  $R^2=0.932$ )

The displacement thickness  $\delta^*$  in region 1 is calculated as follows.

$$\delta^* = \int_0^{\delta} (1 - \frac{u}{U}) dy = \int_0^{0.226} (1 - \frac{227.6}{168}) y^{0.1914} dy$$

where y,  $\delta$ , and  $\delta^*$  are normalized by the height of the passage, and correspond to the distance from the surface, the boundary layer thickness, and the displacement thickness. The velocity at the edge of the boundary layer in Region 1 is 168 ft/s. The definition of the displacement thickness used is similar to the one on a flat plate. As mentioned by Schlichting (p.239), the formula is still valid in an axisymmetric case as long as the y-axis is normal to the surface.

We get  $\delta^*$ =0.033 for region 1 and  $\delta^*$ =0.0038 for region 3.

The inlet blockage is defined by  $B = \frac{Aeff}{Ageom}$ 

In first approximation, neglecting the blade cut-back, we have

$$B = \frac{R_s^2 - R_h^2}{r_s^2 - r_h^2} \tag{D.1}$$

where  $R_s = r_s - \delta^*_{shroud}b$ ,  $R_h = r_h - \delta^*_{hub}b$  and b=r<sub>s</sub>-r<sub>h</sub>

Introducing the expression of  $R_s$  and  $R_h$  in equation (D.1), and neglecting

$$\left(\delta_{hub}^* - \delta_{shroud}^*\right)$$
 with respect to  $(r_h + r_s)$ , we get

$$B \approx 1 - \delta_{hub}^* - \delta_{shroud}^*$$

Numerically, we get B=95.3%

Considering the approximations made (y-axis normal to the surface, no cut-back), the assumption of 5% blockage for the design is perfectly valid.

The AK value can be estimated by

$$AK = \frac{Cm_{shroud}}{Cm_{mean}} \approx \frac{251}{200} = 1.25$$

The calculations have been repeated upstream of the leading edge to ensure that the blade blockage did not affect significantly the evaluation of AK and B.